

**Extratropical Transition in the Ensemble Prediction System of
the ECMWF:
case studies and experiments**

Zur Erlangung des akademischen Grades eines
DOKTORS DER NATURWISSENSCHAFTEN
von der Fakultät für Physik der Universität (TH)
Karlsruhe

genehmigte

DISSERTATION

von

Dipl.-Met. Doris Anwender
aus München

Tag der mündlichen Prüfung:	09.11.2007
Referent:	Prof. Dr. S. Jones
Korreferent:	Prof. Dr. C. Kottmeier

Abstract

The extratropical transition (ET) of tropical cyclones often has a negative impact on the predictability of the atmospheric situation both around the ET event and further downstream. Guidance with respect to this uncertainty can be obtained from ensemble prediction systems. The representation of several tropical cyclones that underwent ET are investigated in the ensemble prediction system (EPS) of the European Centre for Medium Range Weather Forecasts (ECMWF).

The variability in association with an ET in the ensemble members is investigated performing case studies of five ET events. Two North Atlantic and three western North Pacific cases are chosen such that they cover a wide range of ET intensities. In synoptic analysis a trough-ridge-trough pattern associated with all the ET cases is identified. Plumes of high uncertainty in terms of the standard deviation of the 500 hPa geopotential are found stretching downstream from each ET event. With the aid of EOF analysis combined with clustering of the principal components, two characteristic variability patterns associated with uncertainty in the shift and the amplitude of the trough-ridge-trough pattern are found. Relations between the ET development in the individual clusters and their contribution to these patterns of variability are seen.

The structures of singular vectors (SVs) targeted on a specific tropical cyclone are examined. The SVs exhibit different structures in the tropics and in the midlatitudes. The midlatitude structures of the SVs are connected to baroclinic instability. The tropical SVs denote inertial and barotropic instability. The SVs are used to accomplish sensitivity experiments with the ECMWF EPS.

Sensitivity experiments are presented using the ECMWF EPS to investigate the impact of the perturbations targeted around tropical cyclones on the predictability of the extratropical transition and the downstream flow. Similarly, the impact of the stochastic physics is examined. Finally, the impact of higher horizontal resolution in the EPS is investigated. It is found that the targeted perturbations account for the correct representation of the spread closer around ET time while the stochastic physics is rather responsible for the later forecast times. The targeted perturbations have more influence on the track spread while the stochastic physics yields more spread in the intensity in terms of mean sea level pressure. Without the targeted perturbations the analysis would lie outside of the ensemble spread. The high resolution runs show a better representation of the landfall but still at the time of the filling the analysis central pressure is outside of the ensemble spread. It is shown that the errors introduced into the forecast during ET affect the predictability far downstream.

Contents

1	Introduction	7
2	Extratropical transition	11
2.1	Current understanding of extratropical transition	11
2.2	Challenges in numeric forecast	13
2.3	Influence of extratropical transition on the numerical forecast	17
2.3.1	Track forecast	18
2.3.2	Subgrid scale processes	19
2.3.3	Downstream propagation of uncertainty	20
3	Ensemble prediction	23
3.1	Theory of ensemble forecast	23
3.2	Generating the ensemble	28
3.2.1	Initial perturbations	29
3.2.2	Stochastic physics	40
3.3	The ensemble prediction system	42
4	Case studies	45
4.1	Overview of cases	46
4.1.1	Strong events	48
4.1.2	Weak events	51
4.2	Representation of uncertainties	54
4.2.1	Strong events	55

4.2.2	Weak events	61
4.3	The analysis method	64
4.3.1	Patterns of variability	65
4.3.2	Fuzzy clustering	67
4.4	Clustering the ensemble members	70
4.4.1	The empirical orthogonal functions	71
4.4.2	The Clusters	76
5	Experiments	93
5.1	Overview over experiments	93
5.2	Structure of the singular vectors	96
5.2.1	Spatial structure	101
5.2.2	Distribution of energy	106
5.2.3	Temporal evolution	110
5.2.4	Comparison with Eady-Index	111
5.3	Influence of targeted perturbations	114
5.3.1	Effect on tracks	114
5.3.2	Effect on the amount of spread	120
5.3.3	Response on Clustering	129
5.4	Influence of stochastic physics	133
5.4.1	Effect on tracks	133
5.4.2	Effect on the amount of spread	137
5.4.3	Response on Clustering	146
5.5	High resolution experiments	147
5.5.1	Effect on tracks	148
5.5.2	Effect on the amount of spread	152
5.5.3	Response on Clustering	154
6	Conclusions	161
	Bibliography	169

1 Introduction

The threat to life and property due to tropical cyclones (TCs) is well known. Tropical cyclones attract enormous public and media attention through their immense wind speeds, their high damage potential and their exceptional appearance when they are still over the ocean. Often considerable media coverage is given to tropical cyclones even in countries that are not directly affected by them. As soon as the strong winds decrease, the heavy rainfalls weaken and the tropical cyclone loses its typical appearance the danger is reduced. In general, the interest in such a system decreases considerably. However, if a weakening tropical cyclone meets an extratropical system with which it can interact, an explosive deepening of the resulting system can occur. Quickly intensifying wind speeds, high amounts of precipitation and giant wave heights can occur. The remnants of a tropical cyclone can move with the midlatitude westerly flow over a notable distance towards the eastern side of the ocean basin, in which the tropical cyclone developed, before interacting with an approaching midlatitude system. Hence, severe weather at the west coast of the next continent and further inland could be the consequences many days after the TC had weakened or decayed. Moreover, a tropical cyclone moving into the midlatitudes can modify the preexisting flow pattern in the westerlies. Through its circulation impinging on the jet stream a decaying TC can initiate a Rossby-wave-train which in turn can lead to cyclogenesis far downstream of the transforming TC.

The transformation of a tropical cyclone to an extratropical system, known as Extratropical Transition (ET), occurs in every ocean basin in which tropical cyclones exist. The highest number of ET events can be found in the western North Pacific. The highest percentage of tropical cyclones undergoing ET occurs in the North Atlantic with 45 %.

Extratropical Transition events pose severe problems for weather forecasters, related to the fast increase in forward speed when the transforming TC moves into the midlatitudes. Difficulties arise due to the sudden intensification of a midlatitude system which may be caused by the TC remnants and the resulting severe weather events. While tropical cyclones have been addressed in multiple investigations more effort has been denoted to the research of ET recently.

The numerical forecast for ET is often not reliable (Jones et al., 2003). In such cases of possibly uncertain weather prediction it is desirable to have a measure of probability of the weather forecast. Equally important is the knowledge of which alternative atmospheric situations are probable and which developments are unlikely but possible.

The problem of probability forecast is addressed through the method of ensemble forecast. In general, an ensemble forecast is a collection of different forecasts. These can be forecasts performed simultaneously by different models or model versions, or a number of forecasts with just one model initialized with varying initial conditions and computed simultaneously.

Even before the idea of ensemble prediction found its way into the operational weather centers, forecasters considered different models and compared the information with observations or previous forecasts to issue a new forecast and to estimate its probability. This can be seen as a subjective ensemble forecast.

The aim of this study is to obtain information about the uncertainty associated with an ET event through investigating ET cases of different intensities in an ensemble prediction system. The performance of the uncertainty in the ensemble is represented through the development of different ET scenarios by the members. Closer examination of such scenarios yields insight into physical properties associated with ET. Furthermore, the ensemble allows probabilities to be assigned to the various representations of ET by the individual members. For the investigation the ensemble prediction system (EPS) of the ECMWF will be used.

Furthermore, the instability of the atmospheric situation in association with an ET

is investigated by carrying out new experiments with the ECMWF EPS. The growth, dispersion and downstream development of uncertainties are examined. Uncertainties in the initialization of the TC undergoing ET and in the model due to the small scales of the TC in the coarse resolved global model will be investigated separately for the chosen tropical cyclone. Furthermore, the influence of higher resolution on the representation of uncertainties by the ensemble will be tested. This should give insight in the general propagation of uncertainties due to ET.

The study is arranged as follows. A general overview over the process of ET is given in chapter 2. Difficulties in numerical forecasts in general and in association with ET in particular are discussed. Ensemble forecast and the simulation of initial and model uncertainties are explained followed by a short history of the EPS evolution in chapter 3. Case studies of the ETs of five tropical cyclones of different intensities in the North Atlantic and in the western North Pacific are described in chapter 4 . The description of the experiments concerning the growth of initial and model errors follows in chapter 5. Conclusions of the results in chapter 4 and chapter 5 are given in chapter 6.

2 Extratropical transition

2.1 Current understanding of extratropical transition

Tropical cyclones (TC) moving into extratropical regions are influenced by the change of environmental conditions, such as a more baroclinic flow and the associated higher gradients of horizontal and vertical windspeed, a higher Coriolis parameter, lower sea surface temperatures (SST) and strong SST gradients, extratropical synoptic systems, change of moisture gradients and higher friction, if the TC makes landfall. These modifications differ between individual cases.

Extratropical transition is a process during which the tropical cyclone changes its characteristics gradually and becomes more extratropical. If it moves into the vicinity of an extratropical trough or a mature extratropical system the remnants of the ex-TC can strengthen or get re-inforced by the midlatitude system. The re-intensification as an ET system of the ex-TC depends strongly on the relative position of the TC remnants and the extratropical system, which is called their phasing (Ritchie and Elsberry, 2007). Fig. 2.1 shows a simulation of 16 different TC position relative to an upstream trough in the geopotential field and their final intensities. In general the closer the TC is located at the upstream trough the stronger it can re-intensify. However, differences can also be seen in the longitudinal positions. The dissipating TCs have a stronger eastward component due to their far southward location. Hence, they pass the trough to the south, are advected by the westerlies and dissipate in the environmental wind-shear thereafter. The strong re-intensifiers close to the upstream trough are advected northwards into the baroclinic zone by the southerly winds ahead of the trough.

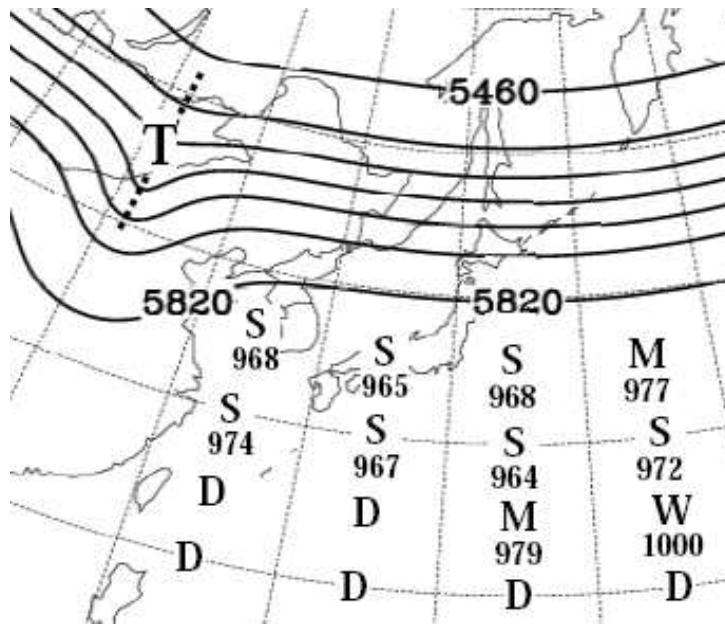


Figure 2.1: Initial positions of TCs relative to an upstream trough marked by T in the 500 hPa geopotential field in 16 model simulations performed by Ritchie and Elsberry (2007). Their final intensities are classified by S = strong intensifier, M = moderate intensifier, W = weak re-intensifier and D = dissipator. Their central pressures are given in hPa.

Klein et al. (2000) proposed a conceptual model of ET that consists of two stages, the so-called transformation and extratropical stages. During the transformation stage the TC starts to react to the different environmental conditions. The TC responds to the higher environmental windspeeds with increased forward motion and undergoes structural changes. The symmetric appearance of its outflow seen in satellite pictures becomes more asymmetric when it impinges on the preexisting midlatitude baroclinic zone. The comparatively large scale cirrus shield associated with the outflow of the TC is transported downstream by the higher vertical wind shear and expands widely in area. Inflow of cooler drier poleward air to the west leads to a partial erosion of the eye-wall and the formation of a so-called dry slot on the south west side of the TC. The cloud pattern is more “comma-shaped”. The appearance of the dry slot is defined as the beginning of the transformation stage by Klein et al. (2000). When the TC moves over cooler SSTs, over stronger gradients of SST or over land it can lose contact to its energy source in terms of high thermal and moisture fluxes or asymmetries in the convection can develop. The warm core of the TC is tilted downstream with height because of the higher vertical shear of the horizontal

wind. This leads to an asymmetric distribution of temperature and precipitation. If the TC moves over land enhanced friction is responsible for a spin-down of the system. If the ET system can complete its transformation stage it has an extratropical structure. That may include a cold core, enhanced frontogenesis, conversion of available potential energy into eddy kinetic energy. Not every TC beginning ET can complete the process. If the transforming system makes landfall, moves over cooler water or if the environmental vertical shear gets too strong it will dissipate. The longer a transforming system has to travel through regions of high vertical wind shear and low SSTs without drawing energy from the extratropical flow, the higher is the probability that it will decay. This is the reason why the most Atlantic TCs undergo ET in September and October as in these months the distance between the areas where the development of TCs is supported to the regions where extratropical development is supported is shortest (Evans and Hart, 2003).

A system that has completed its transformation stage can re-intensify when it moves into the vicinity of an extratropical disturbance. If a positive upper-level PV anomaly, i. e. an upper level trough, approaches the PV anomaly in the mid troposphere of the decaying tropical cyclone a westward tilt with height of the PV anomaly can develop. This is a constellation that is favorable for baroclinic development and a strong re-intensification as extratropical system can result.

2.2 Challenges in numeric forecast

Forecasters in each regional center responsible for issuing warnings and taking preventions are facing the same problems when dealing with ET events. They have to handle difficulties in track forecast, with the strength and distribution of surface winds, with precipitation and possible flooding and with wave height when an ET occurs over the ocean.

Numerical forecast models provide the primary guidance for the operational weather forecaster. It is the responsibility of meteorologists to provide accurate model predictions of the atmospheric state.

An example of the extent of error growth due to small inaccuracies in the initial con-

ditions and due to an imperfect model is the deterministic forecast from 23 September 2005 12 UTC verifying on 29 September 00 UTC (Fig. 2.2). In the forecast (Fig. 2.2 a) a strong deep pressure system is seen at the west coast of Ireland. Horizontal wind speeds of over 33 ms^{-1} in 850 hPa are forecast over Ireland. The central pressure of the system has values of 975 hPa and is followed by another slightly weaker deep pressure system. The analysis of 0000 UTC 29 September (Fig. 2.2 b), however, shows the midlatitude deep pressure system east of the coast of Newfoundland. A frontal system with high wind speeds can be seen at its southern part. Over Ireland a strong ridge and mean sea level pressures of 1015 - 1020 hPa can be seen. The strong deep pressure system over Ireland in the deterministic forecast is ex-Hurricane Philippe which underwent ET in the Atlantic at 23 September 2005 12 UTC in the forecast. In the analysis Philippe decayed at 23 September 12 UTC and its remnants can be seen in form of the frontal system at about $40 - 45^\circ \text{ N}$ and 45° W .

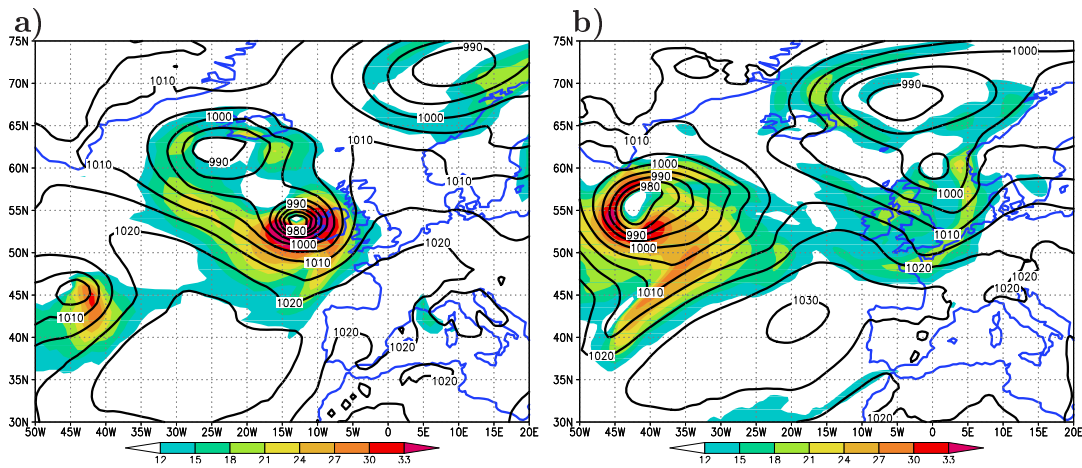


Figure 2.2: (a) Deterministic forecast from 1200 UTC 23 September for 0000 UTC 29 September 2005, i. e. 6 days after the decay of TC Philippe (2005). (b) analysis for 0000 UTC 29 September 2005. Horizontal wind at 850 hPa (ms^{-1} , shaded) and mean sea level pressure (hPa, contours).

This case of false alarm is fatal as the public may lose confidence in the weather forecast and the economy, for example the gastronomy, would experience extensive loss.

The accuracy of a weather forecast depends not only on the presence of errors but also on the stability of the environmental flow in that they are introduced. In a stable environmental flow a forecast may be almost indifferent to small errors while in a more

unstable flow they can lead to a completely wrong forecast already for verification times shortly after initialization.

Lorenz (1963a) stated that the atmosphere is a chaotic system. He defined a dynamical system as chaotic if most trajectories or orbits (solutions of the system of differential equations, see section 3.1) in phase space diverge far from each other after a certain time although they were close together in the beginning. Lorenz (1963a) compared two runs of the same model that differed only by round off errors in the initial conditions. After a few weeks forecast time the solutions were no more similar than two random trajectories of the model. Hence, small inaccuracies in the initialization of a weather forecast can lead to large deviations from the true atmospheric development after a small period of linear error growth, i. e. after some days. This effect is called the “butterfly effect” after Lorenz who raised the question if a minuscule disturbance like the flap of a butterfly’s wing can set off a tornado (Kalnay, 2003). The degree of accuracy with which an atmospheric situation can be forecast is called the predictability of this situation. The predictability varies from day to day and from region to region depending on the stability of the environmental flow. Lorenz (1963a) showed that as the atmosphere is a nonlinear dynamical system with instabilities it has a finite limit of predictability even if the model is perfect and even if the initial conditions are almost perfect. He estimated the limit of weather predictability as about two weeks.

A weather forecast consists of predicting the development of an atmospheric state with time. If a numerical model is assumed to be perfect, i. e. no errors are introduced during the model run, an inaccurate forecast is exclusively due to errors in the initial conditions (Buizza et al., 1999). These emerge due to measurement uncertainties and during the preparation of incoming observational data for a forecast, a procedure called data assimilation cycle. The necessity for this procedure arises because of the non-uniformly distributed observations over the globe. Each grid point on a latitude-longitude model needs to be given an initial value for at least the main prognostic variables temperature, moisture, horizontal wind and surface pressure. For a horizontal resolution of 1° and 20 levels this would be 1.3×10^6 grid points over the whole globe. Hence, over 5×10^6 vari-

ables would be needed. For a time window of ± 3 hours $1 \times 10^4 - 1 \times 10^5$ observations of the atmosphere are available. This is about 2 orders of magnitude less than needed and, consequently, raises the demand for a first guess or background state (Kalnay, 2003). The background state is in general a short range forecast (about 6 hours) from the initial state of an earlier time (Palmer, 2004).

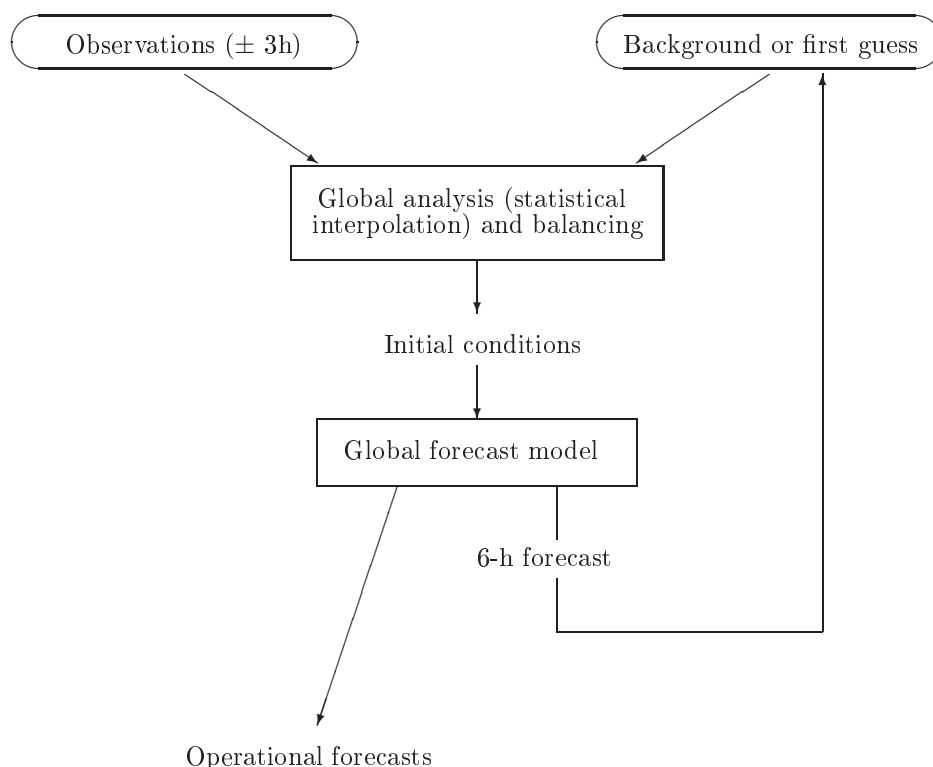


Figure 2.3: Flow diagram of a typical data assimilation cycle (Kalnay, 2003).

During the data assimilation cycle (Fig. 2.3) measurements and such a short range forecast are adjusted to each other. Observations are gathered and inserted in the model and with the aid of a so called cost function the difference between the background and the observations is minimized. Through data assimilation the analysis is obtained which represents the initial conditions for the next forecast.

Errors can be introduced through uncertainties in the measurement systems and through the heterogeneous data coverage over some areas. Over the oceans, for example, sufficient single level data like satellite data may be available (Velden et al., 1997) but there is a

lack of multilevel data. Furthermore, errors are introduced through the interpolation of observational data on the grid points.

As the assumption of a perfect model does not hold, errors can be additionally introduced during the model run (Buizza et al., 1999). These are truncation errors and uncertainties in the parameterization of subgrid scale processes. Some of these errors exhibit a fast growth (Palmer, 2004).

In the numerical forecast such growth of small initial deviations from the atmospheric state and of model errors can have disastrous consequences. If severe storms or possible flooding events are not forecast in time necessary precautions are made too late and a lot of damage can be caused that might have been avoided. This arises the demand for a probability forecast of the deterministic forecast. It is important to get information of how well a forecast can be trusted and to get early warnings through the hint on other possible atmospheric developments.

2.3 Influence of extratropical transition on the numerical forecast

The prediction of extratropical transition poses essential problems to the numerical forecast. Several limited area models exist that have high enough resolution to simulate the internal structure of a tropical cyclone to provide intensity forecasts. However, when TCs move into the midlatitudes boundary conditions from global models are required to simulate their interaction with the large-scale extratropical systems. These models have a much coarser resolution that is adequate to predict the large-scale synoptic systems of the midlatitude circulation. They in turn cannot resolve the small scale features, like deep convection, which provides the energy source of a tropical cyclone (Jones et al., 2003). As neither of these model types is appropriate to simulate both the complex physical interactions during an ET and the transition from the small scales of a tropical cyclone to the large scales of an extratropical systems, a lot of uncertainty is associated with the prediction of ET. Small errors in the initial conditions can lead to large errors in the

numerical forecast depending on the stability of the atmospheric state as described in the previous section.

2.3.1 Track forecast

The track forecast associated with an ET is an important problem. The resolution of global models is clearly not high enough to resolve the inner structures of TCs. Hence, they are not adequate for intensity forecasts. However, information is obtained from global models about the broad structures and the environment surrounding a TC. Therefore, global models have some skill in predicting tracks (Puri et al., 2001). However, the track forecasts in the models are variable and can vary substantially from one day to the next. Thus, the forecaster would need a measure of probability or reliability of the track forecasts.

Difficulties are associated with the forecast of recurvature. A TC might be steered polewards on the western flank of a subtropical high pressure system or ahead of a trough that extends equatorwards into the subtropics. The question as to whether the TC will re-intensify as an extratropical system or not depends strongly on the phasing between the decaying TC and the extratropical circulation. If a numerical forecast model is not able to predict the phasing between the ex-TC and a midlatitude system correctly this would result in a poor forecast (Klein et al., 2002; Ritchie and Elsberry, 2007). However, the forecast is even more sensitive to small position errors when the TC has moved into higher latitudes and increases its forward speed markedly under the influence of the midlatitude westerlies. A correct determination of the timing when the decaying TC starts to accelerate is important. Small uncertainties in the time when the translation speed is enhanced can result in track errors of hundreds of kilometers (Jones et al., 2003). For example, a small delay in the onset of the high translation speed in the model could cause the TC to miss a trough or a front approaching from upstream and a decay of the system may be forecast while in reality the system re-intensifies strongly through interaction with the extratropical system. This is an example of a chaotic development, i. e. a small position error can result in a totally different development of the atmosphere.

2.3.2 Subgrid scale processes

A difficult challenge for numerical models is the description of processes that are of subgrid scale, i. e. that are too small to be resolved by the model grid. These processes called model „physics“ include condensation, evaporation, moist convection, turbulent transfer of moisture, gravity waves, friction and so on. Processes that are resolved by the grid and are computed explicitly by the model equations are called „dynamics“. Small errors originate in the interaction of dry advective dynamics with subgrid scale moist processes and their growth may be enhanced through the dynamical instabilities of the atmospheric flow.

Subgrid scale processes are parametrized, i. e. expressed in terms of variables that are explicitly represented in the atmospheric dynamics. As by the parameterization the real state of the physical processes can only be estimated some inevitable deviations develop between the observed variables and the model tendencies.

Through friction or moving over cooler water a TC may reduce its intensity by increasing its mean sea level pressure and it grows in scale. However, during the transformation stage (Klein et al., 2000) the weakening TC still contains a notable amount of moisture and latent heat release in the midtroposphere from the remaining deep convection. Davis et al. (2007) found that the remnants of TCs have a substantial diabatic contribution to the development of a baroclinic cyclone. Errors induced by the parameterization of moist processes not only have effects on the forecast of the intensity of the ex-TC in the midtroposphere but also have a dynamical impact on the outflow. Uncertainties in heat and moisture content result in uncertainties associated with the prediction of the convection that in turn leads to inaccuracies in the forecast of the height and horizontal scale of the outflow. Furthermore, if a decaying TC recurves but stays equatorwards of the strong vertical wind shear of the midlatitudes it can remain its circulation and transport a large amount of moisture along. A midlatitude system approaching several days after the decay of the TC may possibly interact with the remnant moisture field. Uncertainties in the intensification of the extratropical system many days later may be the consequence.

Other processes that may cause problems due to their parameterization includes the turbulence occurring through the impinging of the outflow of the TC on the midlatitude jet stream. Rappin et al. (2006) found in their model studies that stronger jets produced more rapid intensifications of TCs because of the stronger inertial instabilities at the anticyclonic shear side of the jet. Furthermore, the jet is a region where barotropic instability can occur if the horizontal wind profile has a certain curvature, i. e. if the acceleration is high enough. Moreover, the baroclinic instability is high in the jet through the strong vertical shear of horizontal wind speeds (Pichler, 1984; Holton, 1992). Uncertainties in the parameterization of turbulence in these unstable regions leading to uncertainties in the jet strength can have a strong effect on the predictability of the intensity of an ET.

2.3.3 Downstream propagation of uncertainty

An ET does not only influence the predictability in its environment but it can also have an impact on the midlatitude circulation far downstream.

According to Hoskins et al. (1985) the dynamic tropopause can be seen as a representation of upper level PV distributions. In adiabatic frictionless flow anomalies in the potential temperature on a surface of constant potential vorticity, for example the tropopause, can be seen as anomalies of potential vorticity (Morgan and Nielsen-Gammon, 1998). This will be explained in detail below.

The effect of an ET on downstream development of disturbances can be described on the dynamic tropopause. The TC can be imagined schematically divided into two rotational components. The cyclonic component describing the comparatively small scale cyclonic circulation in the TC core throughout the tropopause and the anticyclonic component describing the larger scale anticyclonic circulation in the outflow of the TC. When a TC approaches the midlatitude jet, a ridge forms in the jet through the northwards advection of high potential temperature to the west and southwards advection of low potential temperature to the east of the TC caused by the anticyclonic circulation. At the tropopause the anticyclonic circulation exceeds the cyclonic circulation and when both are

centered on the axis of the TC almost only the anticyclonic part can be noted especially farther away from the center. The divergent wind in the outflow additionally advects high potential temperatures into the ridge what sustains the formation of a distinct negative PV anomaly. The northward advection at the westside of the system causing negative relative vorticity due to the conservation of absolute vorticity is exactly the mechanism that excites a Rossby-wave-train which propagates to the west relative to the basic state flow. As soon as the tropical cyclone gets under the influence of the strong vertical shear in the midlatitudes the PV tower gets tilted and the anticyclonic part is shifted downstream relative to the cyclonic part. This is a constellation that allows the cyclonic part to transport air of high potential temperature into the ridge at its eastern side and low potential temperature into the trough upstream of the ridge at its western side. Thus, the cyclonic parts act to sustain the amplitude of the ridge and the steepness of the upstream trough-ridge pattern. The anticyclonic circulation is responsible for the westward propagation relative to the basic flow and for the downstream development. On its eastern side it continues advecting air of lower potential temperature into the downstream trough which deepens consequently (Riemer et al., 2007).

Small errors in the phasing of the weakening TC and the midlatitude wave pattern could lead to weakening or amplification of this mechanism by positive or negative interference with the preexisting midlatitude wave pattern. Consequently, errors can travel downstream with the Rossby-wave-train.

3 Ensemble prediction

3.1 Theory of ensemble forecast

In the previous section it has been described that the accuracy of numerical weather forecast will always be limited. One single forecast does not yield information about its own accuracy and whether the atmospheric situation has a low or a high predictability. Because of the inevitable error growth, a forecast that consists of several solutions instead of only one, a so-called ensemble of forecasts or simply ensemble forecast, is of more value than the deterministic forecast alone (Tracton and Kalnay, 1993). A deterministic forecast is a fully determined forecast initialized with complete, certain, sufficiently accurate initial conditions. It produces a single particular result and does not give information about its uncertainty. Ensemble forecast can be treated as “stochastic”. A stochastic process is non-deterministic, i. e. one solution is only one of many possible solutions (Schönwiese, 1985). An ensemble forecast can be seen as probability forecast and consists of marginally different initial states of the atmosphere developing into different final states after a certain forecast time. The small deviations of the initial states are forecast error estimations and are represented by small perturbations of the forecast model, referred to as initial perturbations. Depending on the number of members of the ensemble showing similar final states probabilities can be assigned to the different forecasts.

In the case of a probability forecast the individual prognostic variables with their estimated uncertainties are described by probability density functions (pdf) $\rho(\mathbf{X}, t)$ where \mathbf{X} describes an atmospheric state and t the time. The evolution of a pdf is usually considered in phase space. If the state of a system is described by m variables x_1, \dots, x_m the

phase space is an m -dimensional Euclidean space with coordinates x_1, \dots, x_m . Each point in the phase space represents an instantaneous state of the system. Hence, the state of the system at one time in phase space is fully described by just one point. A temporal development of the system, known as trajectory in phase space (Lorenz, 1963a), is described by a succession of such points. As the real state of the system \mathbf{X} is uncertain it is described by the pdf instead of just one point. The probability that the state \mathbf{X} lies in a volume S of phase space at time t is $\int_S \rho(\mathbf{X}, t) dS$ (Palmer, 2004). Ensemble prediction is the prediction of the evolution of the pdf of the individual model variables from an initial state to a future pdf. The future pdf describes the state of the atmosphere at the end of a limited time interval.

Epstein (1969) first introduced stochastic-dynamic forecasting under which falls ensemble prediction. He derived a forecast equation that described the evolution of the pdf with time under the dynamics of the forecast model.

$$\frac{\partial \rho}{\partial t} + \nabla_D \cdot (\dot{\mathbf{X}}\rho) = 0 \quad (3.1)$$

This continuity equation is called the Liouville equation (Epstein, 1969; Ehrendorfer, 1994). Analogous to the continuity equation in fluid dynamics which describes the mass conservation, it states that no probability density, i. e. ensemble member, can be created or destroyed. The model has D dimensions.

A forecast of the true probability would have to be started from an infinite number of initial perturbations covering the uncertainty completely. Although Epstein (1969) showed that the future pdf can be approximated by predicting only the first two moments, the mean and standard deviation of the initial pdf, stochastic-dynamic forecasting was still not feasible for modern forecast models as they have too many degrees of freedom as described in section 2.2. Each of the grid points would have to be provided with a pdf for each model variable.

Leith (1974) proposed the Monte Carlo ensemble forecast with a finite number of members. The method of assuming random initial perturbations that are added to the initial conditions and performing an ensemble forecast is known as the Monte Carlo technique.

In the Monte Carlo method the pdf is precisely defined by all of the random initial perturbations. The higher the number of dimensions of the problem the more useful the result obtained by the Monte Carlo method.

However, in weather prediction the pdf is uncertain because the number of dimension in current numerical forecast models is too high. It is technically not possible to solve the partial differential equations of the model with a sufficiently high number of perturbations that cover the uncertainties in all the degrees of freedom (model variables, grid points, ...). Therefore, the pdf can only be calculated approximately. The purpose of reasonable ensemble prediction is to cover the largest possible uncertainties in the atmosphere, i. e. to describe the largest possible error growth. The ensemble has to be reliable in the sense that if there are instabilities in the atmosphere the ensemble has to detect them by showing sufficient deviation between the different solutions of the individual forecasts. If the highest uncertainties are perfectly described the real atmospheric development should be included in the ensemble in any case. Furthermore, the ensemble members should stay close together if there are not much uncertainties in the atmosphere, i. e. the members should not indicate uncertainties if there are none. Therefore, instead of describing the evolution of the complete pdf it is only necessary to find out these small initial perturbations that will grow most and yield the most different solutions of the individual forecasts.

A schematic of an ensemble forecast is shown in Fig. 3.1. At the beginning the individual forecasts, started from slightly perturbed initial conditions, lie close together. In this phase they can be seen as one deterministic forecast in the sense that one single initial state is determined and the forecast yields one unique forecast state (Palmer, 2004). After a certain time, however, the forecasts in Fig. 3.1 show a much larger spectrum of possible solutions. Examining how far and after which time the solutions diverge from each other allows a quantification of the uncertainty and an estimate of how long the atmospheric situation can be predicted with a good degree of accuracy. Fig. 3.1 indicates that in the deterministic phase the ensemble mean would be a good representation of the development in all the ensemble members. In the stochastic phase, however, the mean in the case shown in Fig. 3.1 would be of no use as it would deviate far from all the members and overlap

with none of them. However, investigating the groupings of ensemble members during the stochastic phase can give information about alternative atmospheric evolutions and their probability, depending on the number of members in the individual groups.

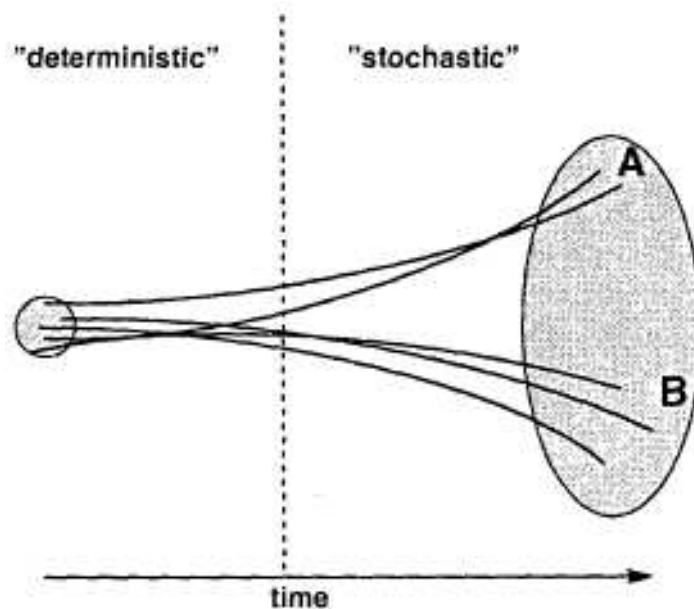


Figure 3.1: Schematic of ensemble prediction, with individual trajectories drawn for forecasts starting from a representative set of perturbed initial conditions within a circle representing the uncertainty in the initial conditions and ending within the range of possible solutions, represented by the ellipse. For the shorter range, the forecasts are close to each other and they may be considered deterministic, but beyond a certain time, the forecast is stochastic. Forecasts may cluster into groups of similar trajectories (denoted A and B in the figure), whose probability of verification may be related to the number of forecasts in each group (Tracton and Kalnay, 1993).

The initial error growth and the length of time over which the ensemble members still lie close together depend strongly on the initial state of the atmosphere. Some atmospheric flow patterns, for example blocking anticyclones or cut-off lows, are known from the experience of operational weather forecasters to be very stable and thus very predictable. Other flow types are very unstable and therefore unpredictable. The Lorenz attractor (Lorenz, 1963a) gives a nice example of the dependence of the flow development on the initial state. It describes the development in time of a 3-dimensional, dynamic, non-linear, autonomous system with three variables in phase space. Two dimensions of the Lorenz attractor are shown in Fig. 3.2. The time development of the three model variables x_1 , x_2

and x_3 is determined by

$$\begin{aligned}\frac{dx_1}{dt} &= \kappa(y - x_1) \\ \frac{dx_2}{dt} &= \gamma x_1 - x_2 - x_1 x_3 \\ \frac{dx_3}{dt} &= x_1 x_2 - \phi x_3\end{aligned}\tag{3.2}$$

where x_1 , x_2 and x_3 are the three model variables and κ , γ and ϕ are parameters that are kept constant within one integration. The parameters can be changed, however, to obtain a family of solutions. The system is non-linear since it contains products of the dependent variables, dynamic since it describes the development with time of the variables and autonomous since the coefficients are not time dependent. The dimensions of the phase space are the independent variables $x_1(t)$, $x_2(t)$ and $x_3(t)$ and the points in the phase space show the simultaneous values of the three variables at any time.

In Fig. 3.2 only $x_1(t)$ and $x_2(t)$ are presented. The solutions of Eq. (3.2) are the orbits or trajectories in phase space. An attractor is an attracting state of the system that is approached by trajectories in phase space again and again. An atmospheric attractor would be, for example, the climate. The black circle in Fig. 3.2, which would actually be a

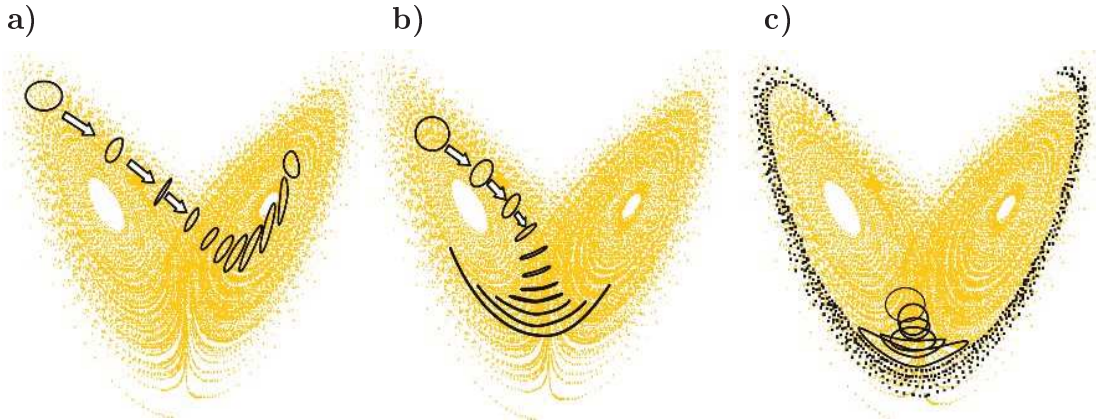


Figure 3.2: Phase space evolution of an ensemble of initial points on the Lorenz (1963a) attractor for three different sets of initial conditions.

sphere in the 3-dimensional system, contains different estimated states of the atmosphere at the initialization time of a forecast. The circle is created by adding small errors to points on the attractor. The circle of points is the pdf of the atmospheric state in phase

space. The two wings of the attractor can be considered as two different weather regimes (Buizza, 2004). If the points are added in regions that are stable (Fig. 3.2 a) they stay close together. Small perturbations stay small and the situation is highly predictable. All of the points in the circle in Fig. 3.2 a describe a regime change. If the small perturbations are added in a less stable region (Fig. 3.2 b) the points in the sphere stay close together for a short time, indicating good predictability for a finite period but thereafter they show a bifurcation. About 50 % of the initial atmospheric states show a regime change and a much wider range of possible developments. Hence, the situation is quite predictable for a short time but a regime change could be forecast with a probability of only 50 %. Adding the small initial errors on points of the attractor that are located in very unstable regions (Fig. 3.2 c) the atmospheric states that have been very similar in the beginning evolve into completely different states after a very short time and a total loss of predictability would result even for a short range prediction.

3.2 Generating the ensemble

Adequate computer resources for the computationally expensive method of ensemble forecasting only became available at the beginning of the 1990s. Ensemble forecasting was implemented in December 1992 both at the ECMWF and at the US National Centers of Environmental Prediction (NCEP). The ensemble at the ECMWF is generated by performing 50 runs with a version of their numerical weather prediction model that is about half as high resolved as the version used for the operational forecast. The ensemble is initialized with 50 slightly different initial perturbations added to the initial best estimate, i. e. the analysis.

The aim of the ensemble forecast is to predict a probability of an event that matches the percentage of occurrence of this event. Taking an example out of climate prediction, one can say that the forecast probability that it will rain a certain amount one particular day in the year should be equal to the percentage of such rain events on this day over past years. The ensemble should be reliable, that is its hit rate has to be high and its false

alarm rate has to be low. In other words, if an event occurs it should be forecast and if it does not occur, it should not be forecast. Reliability of the ensemble involves the detection of the fastest growing errors, as explained in the previous section. A quantity to determine how far the ensemble members differ from each other at a given time is the spread, often represented by the standard deviation with respect to the ensemble mean or the root-mean-squared difference with respect to the control forecast. If the initial uncertainties are fully described by the initial perturbations of the EPS and model errors play no role, a small spread would indicate a very predictable situation. In contrast, a large spread of the possible atmospheric developments should coincide with a low predictability. However, the spread is not only used as a measure of uncertainty. It also yields information about possible alternative atmospheric developments and indicates which events are not likely to happen.

To get information about the highest possible uncertainty it is important that the largest possible error growth is contained in the ensemble forecast. Therefore, estimating the pdf that describes the initial uncertainties includes identifying the structures, that are the most important ones for the dynamical development and the dispersion in the ensemble (Leutbecher and Palmer, 2007).

3.2.1 Initial perturbations

The perturbations that are used to initialize an ensemble have to be constructed such that the ensemble describes the largest possible deviations of initially very similar atmospheric states from each other. It would be useless to construct initial perturbations from random or arbitrary chosen errors because they might not comprise the fastest growing error structures and a consequential low spread could erroneously indicate a high predictability. Hence, the structures that exhibit high instabilities in the atmospheric flow have to be identified. To give an example, such structures that grow strongly may be associated with troughs in the geopotential that are tilted to the west with height, i. e. the structures indicate regions of baroclinic instability.

Different methods are used at different weather forecast centers to find the most unstable structures with which they initialize their ensembles. The US National Centers for Environmental Prediction (NCEP), for example, uses bred vectors (Toth and Kalnay, 1997). These are generated by perturbing their model with a random number. The perturbed and unperturbed states are evolved with their non-linear forecast model for some time. At the end of that time the difference between the two runs is rescaled to the amplitude of typical analysis errors and inserted as new difference of the new state from the unperturbed. The growing cycle is repeated and the bred vector is the perturbation that is obtained after several growing and rescaling cycles. The Canadian Meteorological Service uses initial conditions based on an ensemble transform Kalman filter (ETKF) that is very similar to the breeding method of the NCEP. The ETKF technique is like a refined breeding method in the sense that the rescaling is replaced by a linear transformation.

At the ECMWF initial perturbations are calculated using singular vectors (SV). Singular vectors are obtained through performing a stability analysis which is the general proceeding in the search for unstable structures. A stability analysis comprises the substitution of the model variables with their basic state plus a small perturbation. The behavior of the perturbation under the influence of the stability of the basic flow, i. e. the growth or decay of the perturbation, has to be investigated. Long time perturbation growth is dominated by the exponentially growing eigenmodes, also called the exponentially growing normal modes, of the flow following the instability criteria of Rayleigh (1880). However, structures exist that have greater amplification rates than the most unstable normal mode over some finite time interval (Farrell, 1982). These structures, called singular vectors, describe the largest possible transient error growth. After a sufficiently long time the most unstable structure will correspond to the most unstable normal mode. Singular vectors are a generalization of eigenvectors.

To illustrate the general stability analysis that yields the SVs as fastest growing solutions, it is convenient to recall first the well known traditional form of stability analysis performed for example in the Eady (1949) model. The important difference between the general and the traditional form is the time dependence of the basic state. While in the

traditional stability analysis the basic state is assumed to be time independent the flow in the general stability analysis varies slowly in time.

In both the general and traditional stability analysis a nonlinear model is considered in that the spatially discretized partial differential equations that govern the dynamics can be written as a set of nonlinear coupled ordinary differential equations \mathbf{F} (Kalnay, 2003; Leutbecher and Palmer, 2007).

$$\frac{d\mathbf{X}}{dt} = \mathbf{F}(\mathbf{X}) \quad (3.3)$$

To test the stability of the system of equations the behavior of small deviations from the basic state has to be examined. Although in the mature and decaying phase of the life cycle of a perturbation nonlinear effects are important, linear theory can be applied during most of the intensification stage (Farrell, 1982). The model variables (e. g. temperature, wind, specific humidity, ...) are decomposed into a basic state and perturbation quantities, so that a trajectory $\mathbf{X}(t)$ is split into $\mathbf{X} = \bar{\mathbf{X}} + \mathbf{x}'$. Hence, a Taylor expansion of Eq. (3.3) yields

$$\frac{d\mathbf{X}}{dt} = \frac{d\bar{\mathbf{X}}}{dt} + \frac{d\mathbf{x}'}{dt} = \mathbf{F}(\bar{\mathbf{X}}) + \left. \frac{\partial \mathbf{F}}{\partial \mathbf{X}} \right|_{\bar{\mathbf{X}}} \mathbf{x}' + O(\mathbf{x}'^2) = \mathbf{F}(\bar{\mathbf{X}}) + \mathbf{A}_1 \mathbf{x}' + O(\mathbf{x}'^2) \quad (3.4)$$

Linearization implies that $\mathbf{x}'\mathbf{x}' = \mathbf{0}$ such that the terms of order $O(\mathbf{x}'^2)$ and higher can be neglected. The Jacobian of \mathbf{F} , $\left. \frac{\partial \mathbf{F}}{\partial \mathbf{X}} \right|_{\bar{\mathbf{X}}} = \mathbf{A}_1$, is called the tangent linear model in differential form consisting of the linearized model equations. It has been introduced first by Lorenz (1965). Consequently the evolution of the perturbation \mathbf{x}' is described by

$$\frac{d\mathbf{x}'}{dt} = \mathbf{A}_1 \mathbf{x}' \quad (3.5)$$

In the Eady (1949) model the traditional stability analysis is performed. It is regarded as the simplest model that represents baroclinic instability. Since it implies the assumption of a time independent basic state, the tangent linear model \mathbf{A}_1 in Eq. (3.4) is time independent. The growth of the small perturbations is calculated with an exponential approach:

$$\mathbf{x}' = \mathbf{f}(\mathbf{X}) e^{\lambda t} \quad (3.6)$$

Substituting (3.6) into (3.5) gives

$$\mathbf{A}_1 \mathbf{f}(\mathbf{X}) = \lambda \mathbf{f}(\mathbf{X}) \quad (3.7)$$

The long term growth of the initial perturbations is revealed by their projection onto the normal modes or eigensolutions, i. e. the eigenvectors with eigenvalues λ of the time-independent tangent linear model \mathbf{A}_1 . However, it is important to note, that over finite time intervals structures exist that grow faster and stronger than the most unstable normal modes. This is caused by the non-normality of the tangent linear model (Farrell, 1982).

In the real atmosphere a general stability analysis has to be performed including the time dependence of the basic state trajectory $\bar{\mathbf{X}}(t)$. In this case the tangent linear model in Eq. (3.4) is time dependent. Integrating Eq. (3.5) a perturbation at time t_1 can be found through

$$\mathbf{x}'(t_1) = \mathbf{x}'_0 + \int_{\tau=t_0}^{t_1} \mathbf{A}_1 \mathbf{x}' d\tau \quad (3.8)$$

where \mathbf{x}'_0 denotes the perturbation at initial time. Following Kalnay (2003) the stability problem can be solved numerically applying a time difference scheme to Eq. (3.3), for example the Crank-Nicholson scheme

$$\mathbf{X}^{n+1} = \mathbf{X}^n + \Delta t \mathbf{F} \left(\frac{\mathbf{X}^n + \mathbf{X}^{n+1}}{2} \right) \quad (3.9)$$

This yields a non-linear model solution

$$\mathbf{X}(t_1) = \mathbf{M}[\mathbf{X}(t_0)] \quad (3.10)$$

where \mathbf{M} is the time integration of the numerical scheme from t_0 to t_1 . Adding a small perturbation $\mathbf{x}'(t)$ and linearization similar to Eq. (3.4) the tangent linear model is obtained

$$\mathbf{x}'(t_1) = \frac{\partial \mathbf{M}}{\partial \mathbf{X}} \mathbf{x}'(t_0) = \mathbf{L}(t_0, t_1) \mathbf{x}'(t_0) \quad (3.11)$$

where \mathbf{L} is the tangent linear propagator that describes the evolution of a perturbation from time t_0 to time t_1 . The adjoint of the tangent linear model on its part describes

the evolution of a perturbation from time t_1 to time t_0 . In the interest of simplicity it is assumed that the model has only real variables, i. e. that the adjoint of the tangent linear model \mathbf{L}^* is simply the transpose of the tangent linear model \mathbf{L}^T (Kalnay, 2003). The key property that allows transient growth larger than that of the eigenmodes is the non-normality of \mathbf{L} , that is, $\mathbf{L}\mathbf{L}^T \neq \mathbf{L}^T\mathbf{L}$.

Calculation of singular vectors

In order to find the fastest growing solutions or perturbations of the tangent linear model and its transpose, a singular value decomposition has to be performed (Björnsson and Venegas, 1997). This can be seen as generalized eigenanalysis. For any matrix there exists an orthogonal $m \times m$ matrix \mathbf{U} and an orthogonal $n \times n$ matrix \mathbf{V} such that

$$\mathbf{L} = \mathbf{U}\mathbf{\Sigma}\mathbf{V}^T \quad (3.12)$$

or

$$\mathbf{L}\mathbf{V} = \mathbf{U}\mathbf{\Sigma} \quad (3.13)$$

with $\mathbf{U}^T\mathbf{U} = \mathbf{1}$ and $\mathbf{V}^T\mathbf{V} = \mathbf{1}$ (Golub and van Loan, 1996). $\mathbf{\Sigma}$ is a diagonal $m \times n$ matrix with the decreasing singular values σ_i ($\sigma_1 \geq \sigma_2 \geq \dots \geq \sigma_n$) as elements. The columns \mathbf{u}_i of \mathbf{U} are the left or evolved singular vectors of \mathbf{L} since they correspond to the end of the optimization interval. The columns \mathbf{v}_i of \mathbf{V} are the right or initial singular vectors of \mathbf{L} since they are valid in the beginning of the optimization interval (Kalnay, 2003).

To calculate the SVs some transformations are necessary. Left multiplying (3.12) with \mathbf{U}^T yields

$$\mathbf{U}^T\mathbf{L} = \mathbf{\Sigma}\mathbf{V}^T \quad (3.14)$$

Transposing (3.14) we obtain

$$\mathbf{L}^T\mathbf{U} = \mathbf{\Sigma}\mathbf{V} \quad (3.15)$$

Considering that Σ is diagonal, left multiplying (3.13) with \mathbf{L}^T and using (3.15) we obtain

$$\mathbf{L}^T \mathbf{L} \mathbf{V} = \Sigma^2 \mathbf{V} = \Lambda \mathbf{V} \quad \text{or} \quad \mathbf{L}^T \mathbf{L} \mathbf{v}_i = \sigma_i^2 \mathbf{v}_i = \lambda_i \mathbf{v}_i \quad (3.16)$$

where $\lambda_i = \sigma_i^2$ and Λ is a diagonal matrix with the elements λ_i . Solving this eigenvalue problem the initial SVs are obtained as eigenvectors of $\mathbf{L}^T \mathbf{L}$. The leading initial SVs are the structures that will grow most quickly and strongest in amplitude from time t_0 to time t_1 .

To calculate the left SVs we left multiply (3.15) with \mathbf{L} and with (3.12) we obtain

$$\mathbf{L} \mathbf{L}^T \mathbf{U} = \Sigma^2 \mathbf{U} = \Lambda \mathbf{U} \quad \text{or} \quad \mathbf{L} \mathbf{L}^T \mathbf{u}_i = \sigma_i^2 \mathbf{u}_i = \lambda_i \mathbf{u}_i \quad (3.17)$$

Solving this eigenvalue problem yields the evolved SVs as eigenvectors of $\mathbf{L} \mathbf{L}^T$. The leading evolved SVs determine the structure of the perturbations after the period of maximal growth. The time interval (t_0, t_1) during that the leading SVs should have grown maximally is called the optimization time. Singular vectors are ordered according to their growth rate, i. e. their singular values, such that the fastest growing structure is the first singular vector (SV1), the second fastest growing is the second singular vector (SV2) and so on.

The growth of the perturbations of the model variables \mathbf{x}' during their optimization time has to be quantified by an appropriate measure. In other words, the perturbation growth has to be defined relative to a particular chosen quantity. The growth will depend on how the amplitude is defined. A nice example to explain the use of these measures is given in Kalnay (2003), where the following question is posed: “What is the optimal initial perturbation (measured by the square of the change in surface pressure over the states of Oklahoma and Texas) that produces the maximum final change after a 1-day forecast (measured by the change in the vorticity between surface and 500 hPa over the eastern USA)?”. This measure is contained in the definition of a norm by which the SVs are defined. It measures the perturbation amplitude at initial and final time. Furthermore, the measure weights the perturbations \mathbf{x}'_0 and \mathbf{x}'_1 of the model variables in Eq. (3.11) in the sense that the perturbation growth is determined by considering only selected model variables, i. e. those contained in the measure. In ensemble forecast a norm is wanted that

adjusts the perturbation scales and structures to realistic error structures. The growth rate of SVs and their scales are dependent on the choice of the norms (Palmer et al., 1998). At ECMWF the equal initial norm is used for all the perturbations such that they are equally likely to occur (Leutbecher and Palmer, 2007). The initial SVs are of equal size. The growth rate has to be determined with respect to the maximization of the initial time norm. The Euclidean norm which contains the identity matrix as weight matrix that defines the inner product is

$$\|\mathbf{x}'_0\|^2 = \mathbf{x}'_0{}^T \mathbf{x}'_0 = \langle \mathbf{x}'_0, \mathbf{x}'_0 \rangle \quad (3.18)$$

If the norm would be defined with any weight matrix \mathbf{W} applied to the perturbation at initial time \mathbf{x}'_0 this would look like

$$\|\mathbf{x}'_0\|^2 = (\mathbf{W}\mathbf{x}'_0)^T \mathbf{W}\mathbf{x}'_0 = \mathbf{x}'_0{}^T \mathbf{W}^T \mathbf{W}\mathbf{x}'_0 \quad (3.19)$$

The initial norm is chosen to be representative of the error distribution at initial time. The final norm is a convenient measure of forecast error because it provides a normalization so that errors of different variables like temperature and wind can be compared. For a measure \mathbf{B} of the perturbations at the end of the time interval t_0, t_1 , applying Eq. (3.11), the final norm would look like

$$\|\mathbf{x}'(t_1)\|^2 = (\mathbf{B}\mathbf{L}\mathbf{x}'_0)^T \mathbf{B}\mathbf{L}\mathbf{x}'_0 = \mathbf{x}'_0{}^T \mathbf{L}^T \mathbf{B}^T \mathbf{B}\mathbf{L}\mathbf{x}'_0 \quad (3.20)$$

At the ECMWF both for the initial and the final time SVs the total energy norm \mathbf{E} is used where \mathbf{E}_0 denotes the total energy norm at initial time. Initial total energy SVs are subcyclone scale and are located mainly around the steering level (Palmer et al., 1998). The steering level for a disturbance is the level in the atmosphere for which the velocity of the flow equals the phase velocity of the disturbance. In the atmosphere the 500 hPa is known as the level that steers the low and high pressure systems which are the atmospheric normal modes. Because of their structure total energy initial SVs can grow strongly (Hartmann et al., 1995) and are appropriate to describe analysis errors (Palmer et al., 1998). Different norms like “enstrophy”, “streamfunction” and “kinetic energy” have

been tested as well that were less suitable to describe the error structure (Palmer et al., 1998).

The squared total energy norm used at the ECMWF is given by the discretized form of

$$\frac{1}{2} \int_{p_0}^{p_1} \int_S (u^2 + v^2 + \frac{c_p}{T_r} T^2) dp ds + \frac{1}{2} R_d T_r p_r \int_S (\ln p_{sfc})^2 ds \quad (3.21)$$

where u , v , T and $\ln p_{sfc}$ are the perturbations of the zonal and meridional wind component, the temperature and the logarithm of the surface pressure. R_d , c_p are the gas constant and the specific heat at constant pressure of dry air, T_r and p_r are a reference temperature and a reference pressure. The volume S denotes the whole model atmosphere (Leutbecher and Palmer, 2007). In this equation the integral of u^2 and v^2 is the kinetic energy and the last term under the pressure integral containing T^2 together with the right hand term containing the logarithm of the surface pressure is the available potential energy (APE). The APE is the difference between the total potential energy (consisting of the internal energy and the gravitational potential energy) of a closed system and the minimum of the total potential energy that could result from an adiabatic redistribution of mass (Lorenz, 1955). The APE is equivalent to the maximum kinetic energy that can be realized by an adiabatic process.

The search for the maximum growth of the norm during the time interval t_0, t_1 , involves the maximization of the ratio of the final time norm to the initial time norm

$$\frac{\|\mathbf{x}'(t_1)\|^2}{\|\mathbf{x}'_0\|^2} = \frac{\langle \mathbf{L}\mathbf{x}'_0, \mathbf{E}\mathbf{L}\mathbf{x}'_0 \rangle}{\langle \mathbf{x}'_0, \mathbf{E}_0\mathbf{x}'_0 \rangle} = \frac{\langle \mathbf{x}'_0, \mathbf{L}^T \mathbf{E} \mathbf{L} \mathbf{x}'_0 \rangle}{\langle \mathbf{x}'_0, \mathbf{E}_0 \mathbf{x}'_0 \rangle} \quad (3.22)$$

The positive definite, symmetric operators \mathbf{E}_0 and \mathbf{E} denote the total energy norm at initial and final time respectively (Puri et al., 2001). Here the property $\langle \mathbf{L}^* \mathbf{x}, \mathbf{y} \rangle = \langle \mathbf{x}, \mathbf{L} \mathbf{y} \rangle$ is used by which the adjoint \mathbf{L}^* is defined with respect to the Euclidean norm (Eq. 3.18). In the case of only real variables the adjoint \mathbf{L}^* is equal to the transpose \mathbf{L}^T of the linear operator \mathbf{L} . With the aid of the variable transformation

$$\mathbf{x}' = \mathbf{E}_0^{-\frac{1}{2}} \tilde{\mathbf{x}}' \quad (3.23)$$

whereas the symmetry of \mathbf{E}_0 implies that $\mathbf{E}_0^{-\frac{1}{2}T} = \mathbf{E}_0^{-\frac{1}{2}}$, Eq. (3.22) can be rewritten as

$$\frac{\|\mathbf{x}'(t_1)\|^2}{\|\mathbf{x}'_0\|^2} = \frac{\langle \tilde{\mathbf{x}}'_0, \mathbf{E}_0^{-\frac{1}{2}} \mathbf{L}^T \mathbf{E} \mathbf{L} \mathbf{E}_0^{-\frac{1}{2}} \tilde{\mathbf{x}}'_0 \rangle}{\langle \tilde{\mathbf{x}}'_0, \tilde{\mathbf{x}}'_0 \rangle} \quad (3.24)$$

Since

$$\mathbf{E}_0^{-\frac{1}{2}} \mathbf{L}^T \mathbf{E} \mathbf{L} \mathbf{E}_0^{-\frac{1}{2}} = (\mathbf{E}^{\frac{1}{2}} \mathbf{L} \mathbf{E}_0^{-\frac{1}{2}})^T (\mathbf{E}^{\frac{1}{2}} \mathbf{L} \mathbf{E}_0^{-\frac{1}{2}}) \quad (3.25)$$

the eigenvalue problem

$$(\mathbf{E}^{\frac{1}{2}} \mathbf{L} \mathbf{E}_0^{-\frac{1}{2}})^T (\mathbf{E}^{\frac{1}{2}} \mathbf{L} \mathbf{E}_0^{-\frac{1}{2}}) \mathbf{V} = \Lambda \mathbf{V} \quad (3.26)$$

has to be solved, which is analogous to the dimensionless form (Eq. 3.16). Consequently, the initial SVs of the operator $\mathbf{E}^{\frac{1}{2}} \mathbf{L} \mathbf{E}_0^{-\frac{1}{2}}$ are the phase space directions that maximize the ratio in (3.24) (Buizza, 2004).

The extratropical perturbations \mathbf{x}'_ϵ , $\epsilon = 1 \dots N_{pf}$ with $N_{pf} = 50$ in the EPS of the ECMWF (without considering model errors, i. e. without stochastic physics) are constructed as follows:

$$\mathbf{x}'_\epsilon = \mu_{ini} \sum_{k=1}^{N_{SV}} \alpha_{\epsilon k} \mathbf{v}_k + \mu_{evo} \sum_{k=1}^{N_{SV}} \beta_{\epsilon k} \mathbf{u}_k \quad (3.27)$$

where \mathbf{v}_k and \mathbf{u}_k are again the leading initial and evolved SVs and $\alpha_{\epsilon k}$ and $\beta_{\epsilon k}$ are drawn from a Gaussian distribution with zero mean and unit variance. The purpose of these coefficients is to weight the singular vectors. For details it is referred to Leutbecher and Paulsen (2004). The coefficients μ_{ini} and μ_{evo} determine the overall magnitude of the perturbations. They are scaled to have an amplitude comparable to analysis-error estimates.

Tropical singular vectors

At ECMWF SV growth is optimized for the extratropical domain, i. e. polewards of 30° , and for tropical domain separately. For the calculation of the so called extratropical SVs the tangent linear model with dry dynamics is used. However, the dry dynamics are not

useful for the description of the perturbation growth in the tropics were moist processes are important. In January 2002 the additional calculation of the tropical SVs (only initial SVs) based on a tangent linear model \mathbf{L}_m that includes large-scale condensation and deep cumulus convection has been introduced in the ECMWF model IFS (Integrated Forecasting System). This new physics package for calculating tropical SVs is called “full physics” package. The extratropical SVs calculated from the tangent linear model without these moisture processes are called “dry SVs” and the tropical SVs are called “moist SVs” (Ehrendorfer et al., 1999).

To optimize SV growth in selected domains, for example in the extratropics, in the tropics or only around tropical cyclones a projection operator is needed. At ECMWF a projection operator \mathbf{P} setting a vector to zero outside a given domain, for example for tropical SVs outside of $30^\circ \text{ S} - 30^\circ \text{ N}$, in the final time norm is used (Puri et al., 2001). Optimizing moist SV growth including the projection operator, Eq. (3.24) obtains the form

$$\frac{\|\mathbf{x}'(t_1)\|^2}{\|\mathbf{x}'_0\|^2} = \frac{\langle \tilde{\mathbf{x}}'_0, \mathbf{E}_0^{-\frac{1}{2}} \mathbf{L}_m^T \mathbf{P}^T \mathbf{E} \mathbf{P} \mathbf{L}_m \mathbf{E}_0^{-\frac{1}{2}} \tilde{\mathbf{x}}'_0 \rangle}{\langle \tilde{\mathbf{x}}'_0, \tilde{\mathbf{x}}'_0 \rangle} \quad (3.28)$$

where the eigenvalue problem

$$(\mathbf{E}^{\frac{1}{2}} \mathbf{P} \mathbf{L}_m \mathbf{E}_0^{-\frac{1}{2}})^T (\mathbf{E}^{\frac{1}{2}} \mathbf{P} \mathbf{L}_m \mathbf{E}_0^{-\frac{1}{2}}) \mathbf{V} = \Lambda \mathbf{V} \quad (3.29)$$

has to be solved analogous to Eq. (3.26). The optimization of SVs for a selected domain is called targeting of SVs on that domain.

The choice of the target area has a substantial impact on the SV structure (Barkmeijer et al., 2001; Puri et al., 2001). Targeting SVs on the whole tropical strip does not guarantee that the fastest-growing SVs will be in the region of a tropical cyclone. However, a tropical cyclone, especially one that undergoes ET, causes a lot of forecast errors as explained in section 2.3. A spread that is insufficient to account for the uncertainty associated with a TC would be the consequence. Therefore, at the ECMWF SVs are calculated targeted on TCs. This is realized by determining optimization regions in the vicinity of the TC such that the fastest growing initial SVs will have grown optimally after their optimization

time in that regions. The optimization region around a TC is determined such that a rectangular box is placed around the TC positions forecast for the optimization time by the latest ensemble run. A minimum extension of this box of 5° in latitudinal and 7° in longitudinal direction is imposed (Leutbecher and Paulsen, 2004).

At the top of Fig. 3.3 all optimization regions over the whole globe are shown for 1200 UTC 14 October 2004. They are determined for TY Tokage (2004) (red box), TY Nock-Ten (2004) (green box) and additionally an optimization region is always calculated for the Caribbean (blue box). The Caribbean region is designed to account for the impacts that uncertainties in that region can have on the forecast for Europe. The optimization regions for 15, 16, 17 and 18 October for Tokage (green) and Nock-Ten (red) are shown in a smaller area at the bottom of Fig. 3.3.

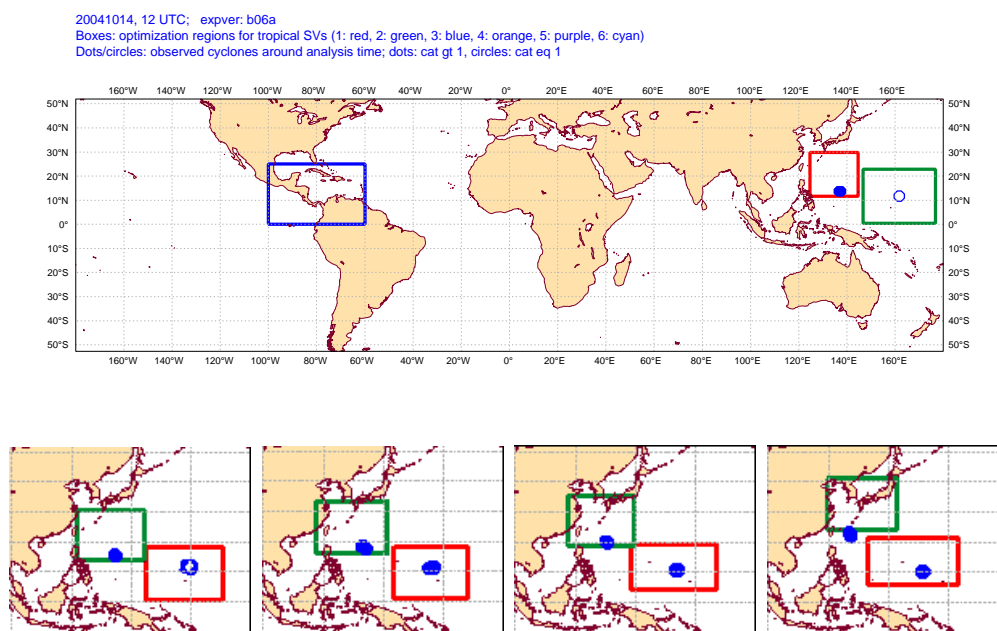


Figure 3.3: Optimization regions calculated on 14 September 2004 12 UTC (top) for TY Tokage (red), Nock-Ten (green) and the Caribbean (blue) and on 15, 16, 17 and 18 September 2004 12 UTC (bottom) for TY Tokage (green) and Nock-Ten (red). Blue dots denote the position of Tokage and Nock-Ten around analysis time.

Before 2004 targeted perturbations have been calculated in a latitude band of 25° N – 25° S to avoid an overlap with extratropical perturbations. Therefore, when a TC moved

polewards of this latitude belt, for example in the case of an ET, the spread became small abruptly and the uncertainty was underrepresented. In September 2004 a new configuration was implemented at the ECMWF. An important innovation was the expanding of the latitude belt for that the optimization regions were determined to $50^\circ \text{ N} - 50^\circ \text{ S}$. The targeted SVs are calculated in an orthogonal subspace to the extratropical SVs such that an overlap is avoided (Leutbecher and Paulsen, 2004). Other innovations include the increase of the number of optimization regions and the introduction of a procedure named Gaussian sampling from that the coefficient α and β (Eq. 3.27) are drawn for the initial perturbations. Furthermore, the targeting is applied also to tropical depressions (WMO-class ≥ 1). Previously, targeting was applied only to WMO-class 2 and higher class TCs.

All these innovations in the new configuration led to changes in the track spreads during an ET and to improvements in the strike probability forecasts. Note that the optimization regions are rectangular boxes that enclose the forecast TC positions from the latest ensemble forecast. Thus, they are not centered on the TCs. In fact, they are expected to cover the region where the TC position will be after the optimization interval of the SVs (in case of the total energy metric: 48h).

3.2.2 Stochastic physics

Until October 1998 the EPS of the ECMWF was based on the “perfect model assumption”, i. e. that all the uncertainties in the forecast are described by the initial perturbations and that during the model run no errors are introduced. However, the uncertainties associated with parametrized processes and their impact on the larger scales cannot be neglected for a longer model integration time. Buizza et al. (1999) stated that the ensemble spread is too small especially later in the medium range beyond a forecast time of about 2 days. It is assumed that there is a significant source of random error associated with the parametrized physical processes. It is not appropriate to enhance the spread by creating larger initial perturbations because in this case the initial spread would be too large. Houtekamer et al. (1996) were the first who introduced a procedure whereby each ensemble member differs

both in the initial conditions and in the parameters describing subgrid scale processes.

At the ECMWF a scheme has been designed that perturbs the parametrized tendencies randomly such that the stochastic perturbation is based on the total tendency from all parametrized processes. The scheme assumes that larger parametrized tendencies correspond to a larger random error component (Buizza, 2004). In the ECMWF EPS an ensemble member \mathbf{e}_ϵ at time t can be seen as

$$\mathbf{e}_\epsilon(t) = \int_{t=0}^t \{\mathbf{H}(\mathbf{e}_\epsilon, t) + \mathbf{\Pi}(\mathbf{e}_\epsilon, t)\} dt \quad (3.30)$$

where $\epsilon = 1, \dots, 50$ designates the perturbed ensemble members and $\epsilon = 0$ the control forecast. \mathbf{H} identifies the resolved and $\mathbf{\Pi}$ the parametrized processes. The integration starts from initial conditions

$$\mathbf{e}_\epsilon(t=0) \equiv \mathbf{e}_0(t=0) + \delta\mathbf{e}_\epsilon(t=0) \quad (3.31)$$

The initial perturbation $\delta\mathbf{e}_\epsilon(t=0)$ is generated as described by Eq. 3.27.

Including a representation of the uncertainty due to the parametrized physical processes Eq. 3.30 becomes

$$\mathbf{e}_\epsilon(t) = \int_{t=0}^t \{\mathbf{H}(\mathbf{e}_\epsilon, t) + \mathbf{\Pi}'(\mathbf{e}_\epsilon, t)\} dt \quad (3.32)$$

where the perturbed parametrized tendency is defined as

$$\mathbf{\Pi}'(\mathbf{e}_\epsilon, t) \equiv \langle r_\epsilon(\Psi, \Theta, t) \rangle_{G, T_s} \mathbf{\Pi}_\epsilon(\mathbf{e}_\epsilon, t) \quad (3.33)$$

where $\langle \dots \rangle_{G, T_s}$ denotes that the same random number r_ϵ has been used for a grid point box of $G \times G$ degrees and over T_s time steps. Each grid point is identified by its latitude Ψ , longitude Θ and vertical hybrid coordinate (Buizza et al., 1999). In other words in Eq. (3.33) the random numbers re-scale the parametrized tendencies. Random numbers from three different intervals for high- ($r_\epsilon \in [0, 2]$), medium- ($r_\epsilon \in [0.5, 1.5]$) and low- ($r_\epsilon \in [0.75, 1.25]$) amplitude stochastic forcing have been tested. Buizza et al. (1999) found that results with the most positive impact in representing the spread were calculated with

the medium amplitude configuration. The values $G = 10^\circ$ and $T_s = 6$ h have been adopted as the operational scheme. Hence, because the EPS has a 1° horizontal grid, the same random number is used for 10 grid points for 6 hours. The stochastic physics with this configuration was implemented operationally on 21 October 1998.

3.3 The ensemble prediction system

The first ensemble forecast with the EPS of the ECMWF was started in December 1992 with 33 members. It was based on 33 nonlinear integrations of a model version with resolution T63L19, i. e. truncation after wave number 63 and 19 level. One of the members, the control forecast, was calculated taking the 12 GMT analysis as initial conditions, and 32 were calculated from perturbations added to the 12 GMT analysis along the directions of maximum growth in phase space (Buizza et al., 1998; Barkmeijer et al., 1999). The initial SVs were calculated with T42L19 resolution. Two sets of SVs were computed with one set confined to grow polewards of 30° N and the other one polewards of 30° S. This is referred to as targeting the SVs in the Northern and Southern Hemisphere respectively. As mentioned in the previous section only variations in the initial conditions were simulated (Buizza and Palmer, 1995) in the first version without taking into account errors due to model uncertainties.

In 1996 the EPS was upgraded to a 51 member T159L31 configuration as a consequence of investigations of Buizza et al. (1998) who found that both increased ensemble size and resolution have positive impact on the ensemble skill. From that time on the SVs were calculated with T42L31 resolution. Buizza et al. (1998) report, however, that the ensemble spread was still underestimated. This may be caused by the neglect of uncertainties associated with model error. Furthermore, they recommended the use of evolved SVs calculated from two days previously. These account for perturbations that have grown during the data assimilation cycle. In March 1998 the evolved SVs were included in the calculation of initial perturbations. In addition, the “stochastic physics” scheme, described in the previous section, was introduced. These innovations led to a range of benefits including

a better level of spread and a higher chance for the verification analysis to be comprised within the ensemble in the forecast range (Buizza et al., 2001).

The resolution of the ECMWF EPS was increased further to T255L40 (~ 80 km grid point spacing) in November 2000. The SVs were calculated with higher vertical resolution (T42L40). These innovations improved the estimation of the probability density function of forecast states and a better predictability for longer forecast times was achieved (Buizza et al., 2001). In September 2004 Gaussian sampling was introduced for the calculation of the extratropical SVs making it possible to calculate the 50 initial perturbations with only a few of the largest SVs. Furthermore, the targeting of perturbations on tropical cyclones was revised. Details were given in section 3.2.1. This was the configuration that our study is based on.

In February 2006 the resolution was upgraded to T399L62 with an enhancement of the vertical resolution for the SVs to T42L62.

The ensemble and deterministic forecasts are initialized twice daily. The ensemble forecasts are available on a 1 degree lat./long. grid and the deterministic forecasts and analyses on a 0.5 degree lat./lon. grid. In the extratropics a simplified and in the tropics a moist physics scheme is used as explained in section 3.2.1.

4 Case studies

An ensemble forecast of a poleward moving TC is often characterized by a high variability among the individual members as result of the difficulties in the numerical forecast explained in section 2.3, indicating low predictability (Harr et al., 2007). Through investigation of the representation of ET events in an ensemble prediction system insight can be gained into both the predictability associated with an ET event and the dominant dynamical mechanisms for ET.

Harr et al. (2007) presented a statistical methodology to examine the behavior of the individual ensemble members in the regions of high variability associated with ET. The analysis method consists of a combination of empirical orthogonal function (EOF) analysis and clustering of the first two principal components. Thereby ensemble members can be grouped together that contribute in a similar way to the main variability. In Harr et al. (2007) for the case of Nabi (2005) an EOF pattern associated with the east-west location and the amplitude of a so called trough-ridge-trough pattern was found.

In this investigation the analysis is expanded to examine five TCs that underwent ET. They were chosen such that they encompass a wide range of TC intensity on the Saffir-Simpson-Scale and also occur over both the North Atlantic and the western North Pacific ocean basins.

4.1 Overview of cases

The representation in the EPS of the North Atlantic hurricanes Fabian (2003) and Philippe (2005) and the western North Pacific typhoons (TYs) Maemi (2003), Tokage (2004) and Saola (2005) has been investigated. The cases are divided into strong events and weak events. Fabian (category 4, NHC 2006), Maemi (category 5, JMA 2006) and Tokage (category 4, JMA 2006) belong to the strong and Saola (category 2, JMA 2006) and Philippe (category 1, NHC 2006) to the weak events. An overview of the cases with their time of recurvature and of ET can be found in Table 4.1. The terms “investigation time”, “FCST1” and “FCST2” will be explained later.

The strong events are characterized by a re-intensification after ET and a marked influence on the midlatitude flow. The weak events do not re-intensify after or decay before ET and do not appear to influence the midlatitude flow. The weak events are chosen because of large forecast errors associated with their representation of ET.

The key variable for our investigation is the potential temperature on the “dynamic tropopause”. The potential vorticity (PV) is conserved in adiabatic, frictionless conditions (Hoskins et al., 1985) and therefore the choice of this variable has the advantage that the dynamics of one conserved variable, the potential temperature, can be viewed along the surface of another conserved variable, the potential vorticity. In isentropic coordinate version of the equation for the PV is

$$PV = -g(f + \mathbf{k} \cdot \nabla_{\theta} \times \mathbf{v}_h) / \frac{\partial p}{\partial \theta} \quad (4.1)$$

where f is the Coriolis parameter, g the acceleration due to gravity, \mathbf{k} the unit vertical vector, ∇_{θ} a three dimensional gradient operator, \mathbf{v}_h the horizontal wind velocity, p the pressure and θ the potential temperature. From equation (4.1) it follows that for a standard atmosphere at rest the PV increases with increasing stability and with increasing Coriolis parameter. In general, the PV increases with increasing total vorticity $f + \mathbf{k} \cdot \nabla_{\theta} \times \mathbf{v}_h$. Consequently, at the tropopause, where the stability increases abruptly, there is a marked increase in potential vorticity.

The tropopause can be defined by PV values between 1.5 - 3 PVU, where $1 \text{ PVU} = 10^{-6} \text{ Km}^2 \text{ kg}^{-1} \text{ s}^{-1}$. The potential temperature can be investigated on a constant plane of the PV and vice versa. For this investigation a value of 2 PVU as definition of the so-called “dynamic tropopause” (Morgan and Nielsen-Gammon, 1998) is used. A $\text{PVU} = 2$ surface can be seen as the shape of the tropopause. If the potential temperature on this dynamic tropopause is investigated the shape of troughs and ridges can be identified clearly. This is because the opposing slopes of PV and potential temperature surfaces result in potential temperature gradients along the 2 PVU surface being much sharper than, for example, gradients along isentropic surfaces (Morgan and Nielsen-Gammon, 1998). In troughs the tropopause is lower and the low potential temperatures bow up to higher levels. In ridges the high potential temperatures reach further down and the tropopause is located higher up. This is illustrated in Fig. 4.1 in that the Icelandic low can be seen as a positive PV anomaly with values of $\text{PVU} = 2$ dipping down to about 500 hPa whereas the potential temperature bows up in the troposphere and down in the stratosphere. In case of a negative PV anomaly the behavior would be opposed.

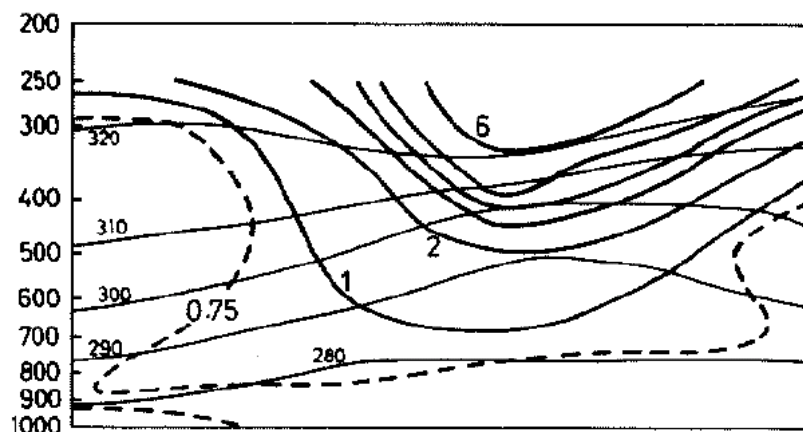


Figure 4.1: Vertical cross-section along a SW-NE line through the Icelandic low on 12 April 1983. The thin lines indicate isentropes at 10 K intervals and the thick lines PV at 1 unit intervals. The 0.75 PV unit is shown by a heavy dashed line (Hoskins et al., 1985).

Table 4.1: Key data of the investigation times of the three typhoons (JMA, 2006) and two hurricanes (NHC, 2006).

	Fabian	Maemi	Tokage	Saola	Philippe
time of recurvature	06 Sept. 2003 00 UTC	11 Sept. 2003 12 UTC	18 Oct. 2004 18 UTC	24 Oct. 2005 03 UTC	/
ET time	08 Sept. 2003 18 UTC	13 Sept. 2003 06 UTC	21 Oct. 2004 00 UTC	25 Sept. 2005 12 UTC	23 Sept. 2005 12 UTC (decay)
investigation time	10 Sept. 2003 00 UTC	14 Sept. 2003 00 UTC	21 Oct. 2004 00 UTC	26 Sept. 2005 12 UTC	23 Sept. 2005 12 UTC
FCST1	04 Sept. 2003 12 UTC	10 Sept. 2003 12 UTC	16 Oct. 2004 12 UTC	21 Sept. 2005 12 UTC	18 Sept. 2005 12 UTC
FCST2	05 Sept. 2003 12 UTC	11 Sept. 2003 12 UTC	18 Oct. 2004 12 UTC	24 Sept. 2005 12 UTC	19 Sept. 2005 1200 UTC

4.1.1 Strong events

Each of the TCs Fabian (2003), Maemi (2003) and Tokage (2004) interacted with a mid-latitude trough. In the case of Fabian the trough was already deep before the interaction and approached from upstream as the decaying TC moved towards the midlatitudes. The decaying Fabian merged with the midlatitude deep pressure system associated with the trough but ex-Fabian was clearly the dominant system. A trough could be seen upstream of Maemi, also. However, the trough was weaker than in the case of Fabian and appeared to intensify as the outflow from Maemi impinged on the midlatitude jet. It is difficult to identify an upstream trough as Tokage approached the midlatitude jet. In this case the ridge downstream of TY Tokage amplified dramatically as the outflow of Tokage interacted with the midlatitude jet. This amplification lead to the formation of an upstream

trough as described by Bosart and Lackmann (1995) for Hurricane David (1979). In all three cases a distinct pattern formed that consisted of the trough that interacted with the TC, a ridge directly downstream and a second trough downstream of the ridge. Recent studies of ET suggest that the TC outflow can contribute to the ridge building (Henderson et al., 1999) and to the subsequent amplification of the downstream trough (Riemer et al., 2007).

The synoptic development after the ET is quite different in each of the cases. Fabian interacted with the upstream trough that rolled up cyclonically during ET. A strong blocking ridge associated with weak zonal flow emerged downstream of the ET system and inhibited the system from moving eastward. The ex-TC turned back to the northwest and the whole system re-intensified strongly (Fig. 4.2 a).

In the case of Maemi, the extratropical cyclone that resulted from the ET and a low pressure center associated with the downstream trough of the trough-ridge-trough pattern developed equally strongly. As in the case of Fabian, Maemi was prevented from traveling eastwards directly after its ET by a strong blocking ridge. The trough associated with the ET rolled up cyclonically and both ex-Maemi and the downstream low intensified moderately (Fig. 4.2 b). The ridge did not weaken until 60 h after ET so that ex-Maemi could then travel eastwards (not shown). The downstream low then intensified to a strong low pressure system over the west coast of America.

The ridge that developed as Tokage's outflow interacted with the midlatitude jet, had a northeast-southwest orientation with quite strong southwesterly flow. Therefore, in contrast to the cases of Fabian and Maemi, it moved to the east quite quickly. A strong potential temperature gradient can be seen directly to the northwest of Tokage near to the crest of the ridge (Fig. 4.2 c) 12 h after the TC had interacted with the midlatitudes. The associated high vertical wind shear and the positive stretching deformation acted to flatten the ridge and to reduce the perturbation kinetic energy at upper levels (Webster and Chang, 1997). After the significant weakening of Tokage due to its landfall in Japan, the ET system re-intensified moderately as the western part of the ridge rolled up cyclonically. Through its continuing tilt to the northeast the ridge acts to thin the downstream

trough that consequently formed a cut off low at about 175° E (Fig. 4.2 c) .

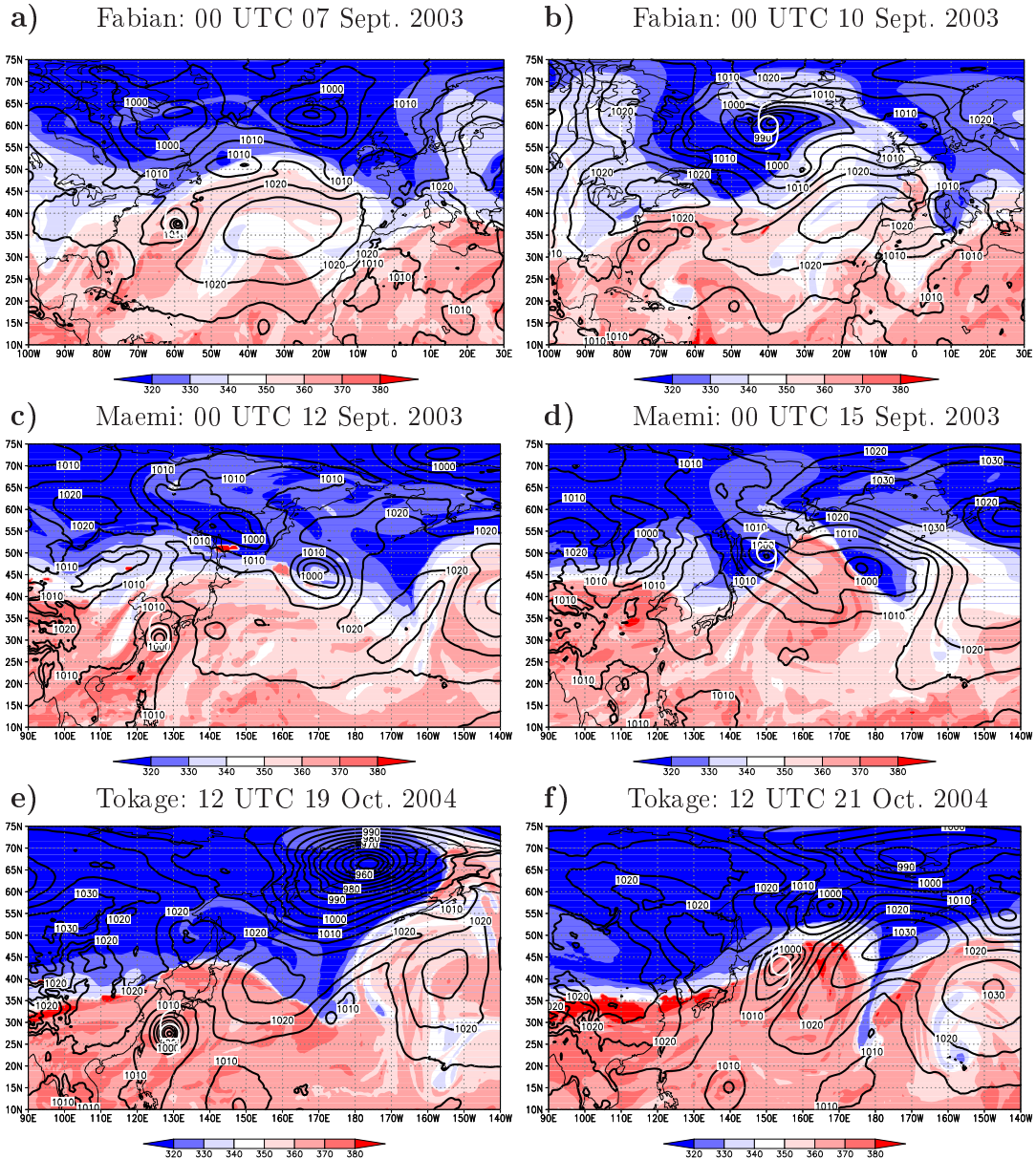


Figure 4.2: Analyses of Fabian on a) 0000 UTC 07 and b) 0000 UTC 10 September 2003, Maemi on c) 0000 UTC 12 and d) 0000 UTC 15 September 2003, Tokage on e) 1200 UTC 19 and f) 1200 UTC 21 October 2004. Fabian, Maemi and Tokage are marked by a gray TC symbol before and by a white TC symbol after ET. Potential temperature on the dynamic tropopause (shaded, K), surface pressure (contours, hPa).

4.1.2 Weak events

The weak events Philippe and Saola were chosen for this investigation because their deterministic forecasts were highly inaccurate. Saola underwent ET and its remnants were absorbed by a large-scale midlatitude low pressure system that subsequently intensified. However, the deterministic forecast failed to predict the ET. Philippe decayed to a remnant low on 1800 UTC 23 September but a strong ET was predicted incorrectly by the deterministic forecasts initialized up to 4 days before its decay.

Saola recurved ahead of a very weak midlatitude trough. A second upstream trough steered the ex-TC eastwards (Fig. 4.3 a). At that time a large-scale quasi-stationary extratropical low pressure system was situated northeast of ex-Saola and affected the track of the TC. The pattern has a strong resemblance to the northeast pattern described in Harr and Elsberry (2000). The influence of the upstream trough decreased and 48 h later Saola's remnants were absorbed by the downstream low.

The position of Saola in the 84 h deterministic forecast that verifies on 0000 UTC 27 September 2005 (Fig. 4.3 b) indicates that Saola did not recurve, even though the initialization time of this forecast (Fig. 4.3 b) was only 24 h before the recurvature time. In the deterministic forecast Saola decayed south of Japan. The recurvature appeared to be sensitive to very small differences in the potential temperature gradient ahead of the midlatitude trough that steers the TC north-eastwards in the analysis (not shown). Only the forecast from 24 September 00 UTC, which was initialized following the turn of Saola towards the northwest, predicted the recurvature.

Philippe was a very small-scale system that could not be resolved in the ECMWF analysis after 21 September 12 UTC. However, the surface reflection of an upper level cold low could be seen at about 65° W and 30° N (Fig. 4.4 a), as described in Franklin (2006). When Philippe was reported as decayed on 1800 UTC 23 September its remnant vorticity center could still be seen (Franklin, 2006). Thus, it is suggested that the remnants of Philippe reinforced the cold low. On 26 September (not shown) a strong ridge upstream of Philippe that seemed to be sustained by the outflow of Hurricane Rita (2005) had

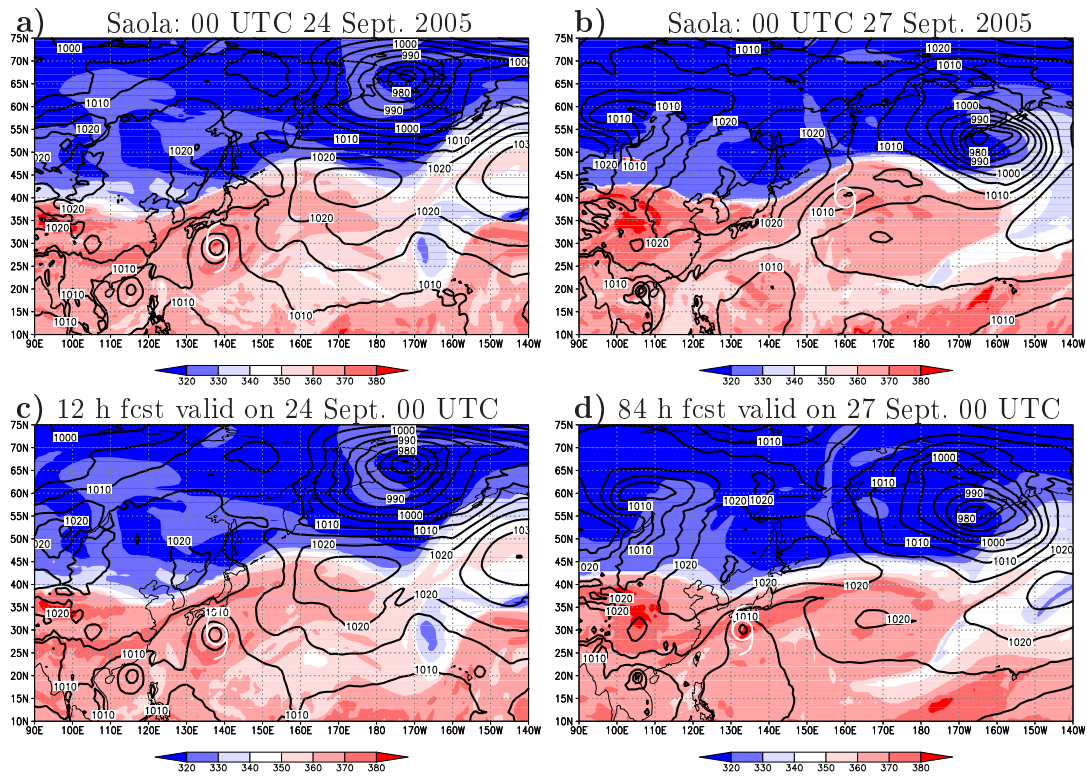


Figure 4.3: Analysis on a) 24 September 00 UTC and b) 27 September 00 UTC. c) 12 h and d) 84 h deterministic forecast from 1200 UTC 23 September. Saola’s remnants are marked by a gray TC symbol. Potential temperature on the dynamic tropopause (shaded, K), surface pressure (contours, hPa).

developed north of the remnants of Philippe. The ridge inhibited an upstream midlatitude trough from approaching and interacting with the cold low at this time. The surface low pressure system ahead of that upstream trough, situated at about 60° W and 45° N (Fig. 4.4 b), had already absorbed the remnant low of ex-TC Rita (Knabb et al., 2006) and subsequently absorbed the cold low containing the remnants of Philippe. The resulting system intensified strongly ahead of a strong upper level potential temperature gradient on 0000 UTC 29 September (not shown). Thus Philippe contributed indirectly to the re-intensification of the midlatitude system.

The deterministic forecast for 1200 UTC 23 September initialized on 1200 UTC 19 September (i. e. 4-day forecast) (Fig. 4.4 c) predicted a larger-scale TC Philippe than was observed. Philippe’s position and the upper-level development were forecast quite well for that time. However, 12 h later in the same forecast (not shown) Philippe interacted with

an upstream trough that extended far south and the ex-TC re-intensified strongly. On 1200 UTC 27 September (i. e. 8-day forecast) (Fig. 4.4 d) the strong ET system merged with a midlatitude low that was connected to a second upstream trough.

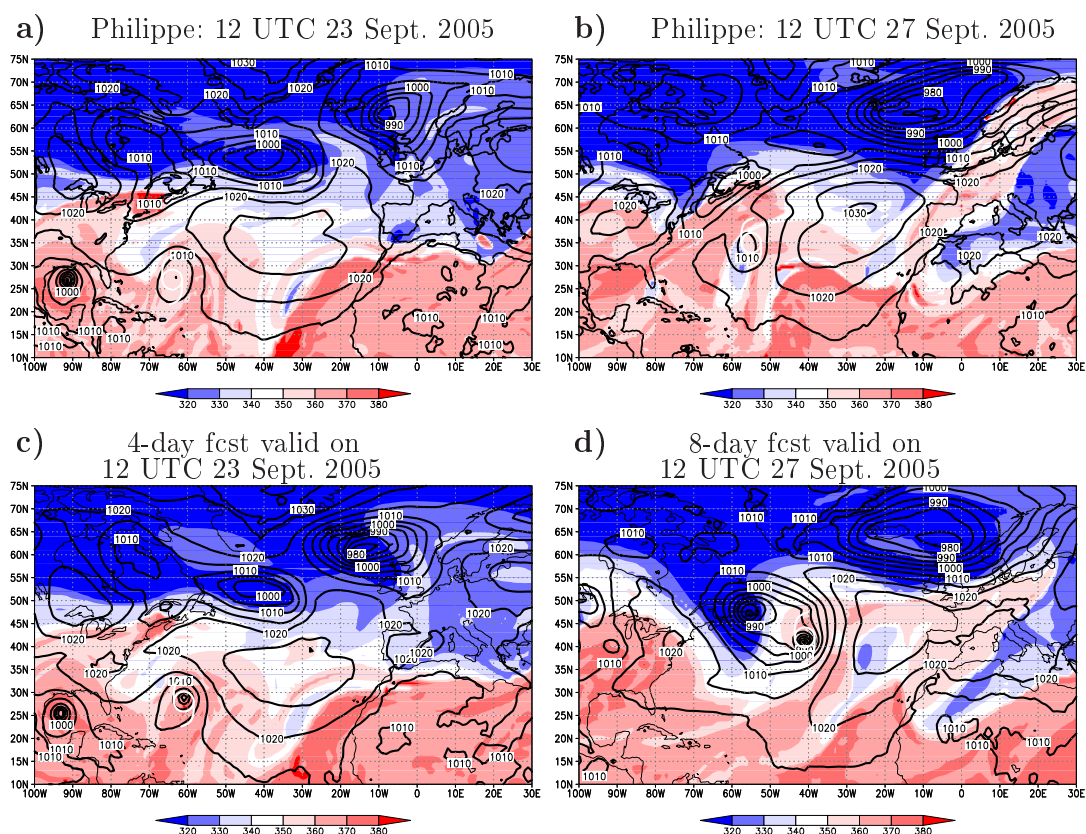


Figure 4.4: Analyses a) 6 h prior to and b) 96 h after Philippe’s decay. c) 4-day and d) 8-day deterministic forecasts from 1200 UTC 19 September. Philippe or the position of its remnants respectively are marked by a gray TC symbol. Potential temperature on the dynamic tropopause (shaded, K), surface pressure (contours, hPa).

The midlatitude flow patterns during the existence of Saola and Philippe were quite different. The flow over the western North Pacific was zonal with only weak small-scale troughs during Saola’s lifecycle whereas the flow over the North Atlantic was more wavy in the presence of Philippe. Nevertheless, the interaction of the TCs with the midlatitude flow was quite similar in both cases.

4.2 Representation of uncertainties

In this section the variability in the EPS associated with the ET events is described using the TC tracks from the analysis, the deterministic forecast and the ensemble forecasts for each case. The tracks are calculated by locating the minimum mean sea level pressure in a region defined by two boxes. One of them extends 3° S, 7° N, 5° E and 5° W from the previous TC position. The other extends 5° in east-west and 7° in north-south direction with its southwest corner 5° E of the TC position. This accounts for the high translation speed of the system after ET. A maximum pressure change of 30 hPa in 12 hours is allowed to exclude the detection of other TCs close by. In addition, Hovmoeller plots (Hovmöller, 1949) of the standard deviation of the 500 hPa geopotential from the 51 ensemble members are averaged over the latitude band of 40° - 50° N. These plots show a development with longitude and time of a variable averaged over a latitude band. The diagram is useful for investigating the propagation of waves. A downstream propagating wave can be visualized for example by positive and negative values of the meridional wind speed. Alternatively, the propagation of wave packets, i. e. spatially limited wave disturbances (Pedlosky, 1987), can be observed. Rossby wave packets usually run from the top left to the bottom right corner of this diagram. Stationary waves would appear as perpendicular oriented maxima and minima of for example meridional wind velocity in the plot.

The standard deviation is one particular measure of the ensemble spread. In this latitude band it illustrates both the variability in the midlatitude pattern of troughs and ridges, and the variability in the representation of the tropical cyclone in question as it moves into the midlatitudes.

For all of the cases two forecast times were chosen, one well before the recurvature started, referred to as FCST1, and the second close to or at the time of recurvature, referred to as FCST2. Through this choice the decrease in the uncertainty associated with the recurvature from the first to the second forecast time can be observed and the uncertainty associated with the ET itself can be isolated from that associated with the

recurvature. Definitions of FCST1 and FCST2 can be found in Table 4.1 for each case.

4.2.1 Strong events

A comparison of the enhanced variability in the vicinity of the ET events shows certain similarities between the three major TC cases. Local maxima in standard deviation can be seen upstream, around or downstream of the ET event.

Fabian

The track of Fabian in the deterministic forecast for FCST1 was quite similar to its analysis up to recurvature but the deterministic forecast did not capture the acceleration afterwards. Six hours after ET time there is a difference of almost 1000 km (Fig. 4.5 a) between the TC position in the analysis and the deterministic forecast. Both analysis and deterministic forecast are situated within the tracks of the ensemble members. The ensemble tracks indicate uncertainty in the forecast of the recurvature, i. e. after 48 to 60 h. In some ensemble members the TC accelerates after recurvature whereas in others, especially those situated at the eastern edge of the plume (at about 35° N and 60° W), it remains slow moving or even decays. Thus, a separation of over 1000 km between the individual positions is seen after 72 h. The ensemble members for the forecast from FCST2 (Fig. 4.5 b), when the TC motion had already changed from northwestwards to northwards, do not show the substantial increase in spread after the recurvature anymore. However, close to the ET time (after about 60 h in Fig. 4.5 b) the TC positions in the members vary noticeably, indicating uncertainty in the ET event. The track in the deterministic forecast lies in the middle of the ensemble tracks while the analysis track differs markedly from the deterministic forecast and lies on the flank and sometimes even outside of the ensemble tracks.

The uncertainty in the recurvature for FCST1 can be seen as increased standard deviation from 0000 UTC 7 September (60 h forecast) at about 50° W (Fig. 4.5 c). High

values extend from the ET time and position (black dot) and even higher values can be found upstream at about 60° W from 12 h after the ET in Fig. 4.5 c. This can be explained through high variability in the ensemble associated with the mature midlatitude system that had developed from the ET of Fabian. The system cannot move to the east because of the blocking ridge mentioned in section 4.1.1. Thus it loops backward to interact with another upstream trough. This second interaction can be seen in Fig. 4.5 c, as the local maxima associated with the ET event and that associated with the upstream trough in the mature midlatitude system merge on 0000 UTC 12 September. Another plume of high values can be found well downstream of the ET event. Those are linked to a downstream trough that deepened in association with the steepening of the blocking ridge directly downstream of the ET of Fabian. In the ensemble forecast from FCST2 the plumes of high standard deviation associated with the ET of Fabian and with the downstream trough have decreased strongly in amplitude. However, they can still be distinguished clearly from 30 h after the ET (Fig. 4.5 d). The highest variability in the forecast from 5 September is connected to the interaction of the ET system with the second trough mentioned above that approached from upstream of the ET event in the major midlatitude system.

Maemi

In the case of Maemi, there is again significant variability associated with the recurvature after about 48 h in the tracks for FCST1 (Fig. 4.6 a). The track spread increases during ET, so that the locations of the TC in the ensemble members differ by over 2000 km after 4 days. During recurvature, the analysis and deterministic forecast are on the eastern edge of the set of ensemble tracks. The spread in the ensemble members for FCST2 (Fig. 4.6 b), initialized when the motion of Maemi had an eastward component in the analysis, is much smaller and increases more slowly than for the earlier forecast time. Nevertheless, shortly after ET (from 48 h) the spread increases. The analysis and deterministic forecast tracks are close together until ET time for both FCST1 and FCST2 but differ by over 700 km from 18 hours after ET.

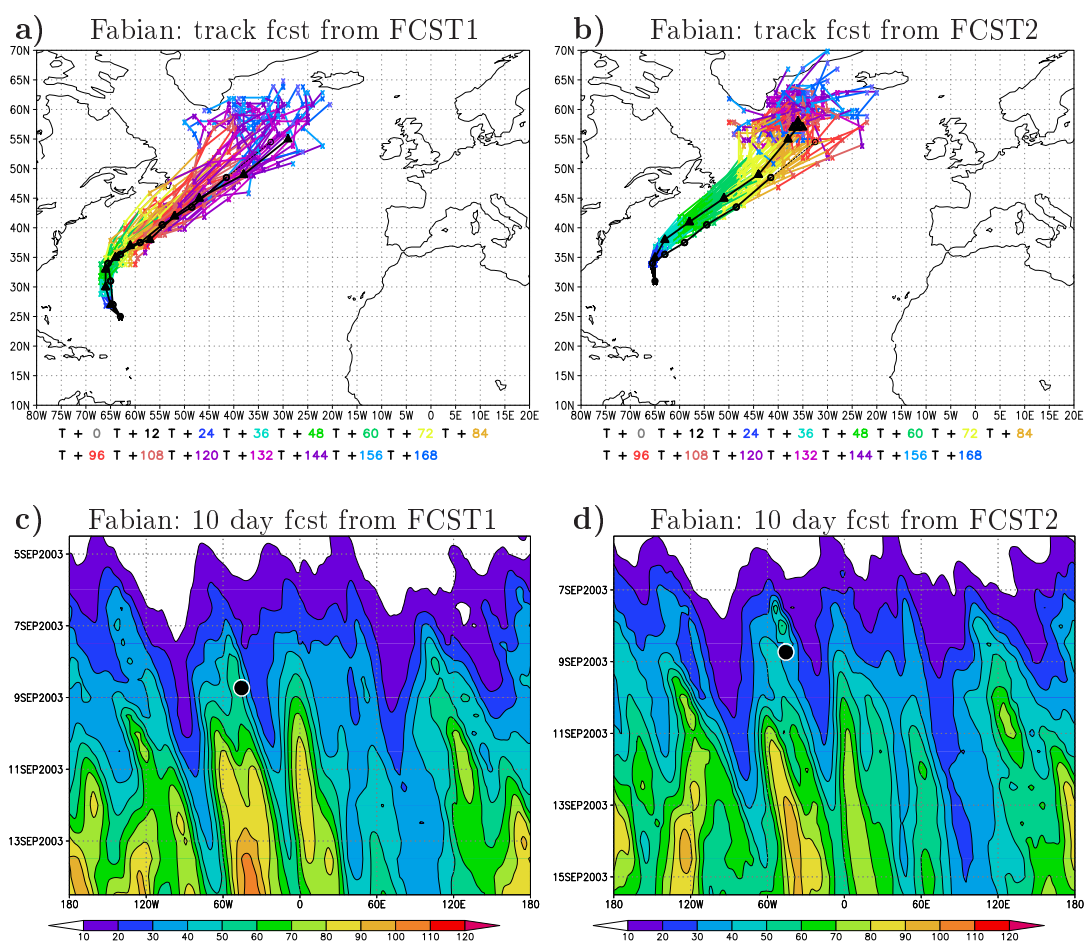


Figure 4.5: Tracks for Fabian based on location of minimum sea level pressure. ECMWF analysis (black line with circles), deterministic forecast (black line with triangles) and ensemble forecast (colors) a) from FCST1 and b) from FCST2 for 7 days. Analysis dashed after ET. Hovmoeller plot of standard deviation of 500 hPa height (m) in the ensemble for Fabian averaged between 40° - 50° N. 10-day forecast from c) FCST1 and d) FCST2. ET position is marked by a black dot.

The Hovmoeller plots from FCST1 and FCST2 (Figs. 4.6 c, d) show enhanced values of standard deviation in the vicinity of the ET but much higher values existed downstream of the ET event. This illustrates that the variability in the downstream trough (Sect. 4.1.1) is higher than that of the ET itself. The standard deviation is largest from 14 to 17 September at about 180°. The region of higher values from 1200 UTC 17 September at about 135° W is still connected to the variability in the downstream trough but the wave has flattened at that time and the predictability has increased. In FCST2 the enhanced values at about 180° from 14 to 16 September (Fig. 4.6 d) have decreased strongly, as in the case of Fabian for the later forecast time. Nevertheless, the variability in the downstream

trough is still significant, as there are no other regions with equally high values of standard deviation at this time.

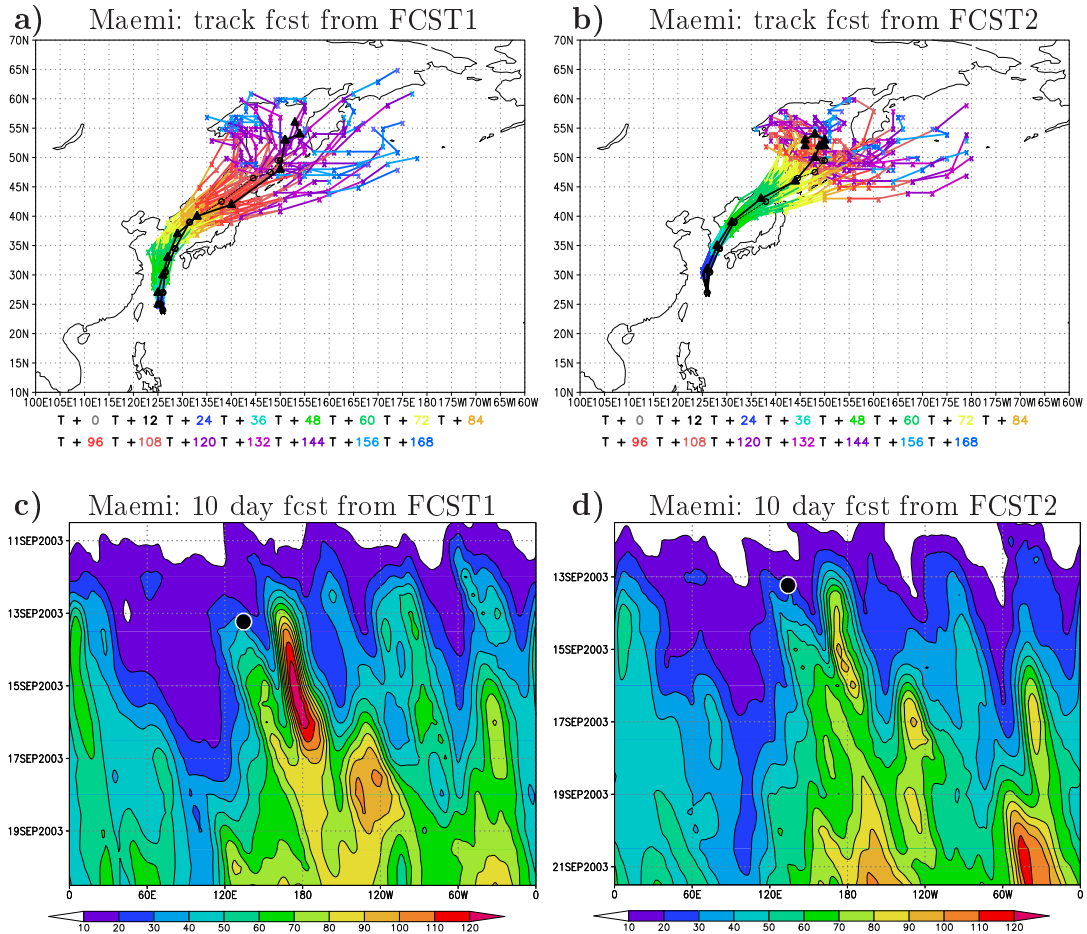


Figure 4.6: As Fig. 4.5 for Maemi.

Tokage

Before ET time the deterministic track forecasts for FCST1 and FCST2 of Tokage are quite close to the analyzed track (Figs. 4.7 a and b) and both fall within the ensemble track forecasts. There is uncertainty associated with the time of recurvature for FCST1 (Fig. 4.7 a). Furthermore, a noticeable increase in spread can be seen at the time of ET and here the analysis track lies at the edge of the ensemble tracks while the deterministic forecast is situated in the center. All but two ensemble members show the tracks to be farther north than in the analysis. In Fig. 4.7 b it can be seen that there are several tracks

south of the analysis and around it in the ensemble members from FCST2. Tokage can no longer be identified in the group of southern forecasts after a forecast time of 84 h. The northern group of ensemble members continue to track Tokage.

The weakening of Tokage during ET associated with its landfall in Japan is not captured in the ensemble and deterministic forecasts for the mean sea level pressure from FCST1 and FCST2 (Figs. 4.7 c and d). In FCST1 (Fig. 4.7 c), at 108 hours the central mean sea level pressure varies between 945 and 985 hPa in the ensemble forecasts compared with the analyzed value of 993 hPa. Only 3 members show a weakening of the central mean sea level pressure to the same value as the analysis, and this only after 132 hours. In FCST2 (Fig. 4.7 d) a subset of ensemble members shows no or only a weak reintensification after ET and similar central pressure values to the analysis after 72 hours. Some members do not track the ex-TC after 84 h forecast time. The remaining members and the deterministic forecast weaken during the transformation stage, but re-intensify after ET.

The plume of high standard deviation originating at ET time in the FCST1 Hovmoeller plot (Fig. 4.7 e) is clearly associated with the ET system itself. Compared to the other two cases of major hurricanes the high values decrease quite quickly. However, a large maximum downstream at about 150° W on 23 October indicates a downstream propagation of the uncertainty associated with the ET. A similar downstream propagation can be seen in the Hovmoeller plot for FCST2 (Fig. 4.7 f). One day after ET there are two localized maxima that decrease in amplitude quite quickly. One is directly associated with the ET of Tokage and one with the ridge downstream of the ET at about 180° . Two days after ET the uncertainty is associated with the downstream trough at about 135° W.

The three major TC cases illustrate nicely that the variability associated with an ET event can be found either upstream, around the ET system, or in the downstream development. It has been shown that the recurvature and the ET event are the main sources of uncertainty. In general, the closer the forecast time is to the ET the more predictable the flow.

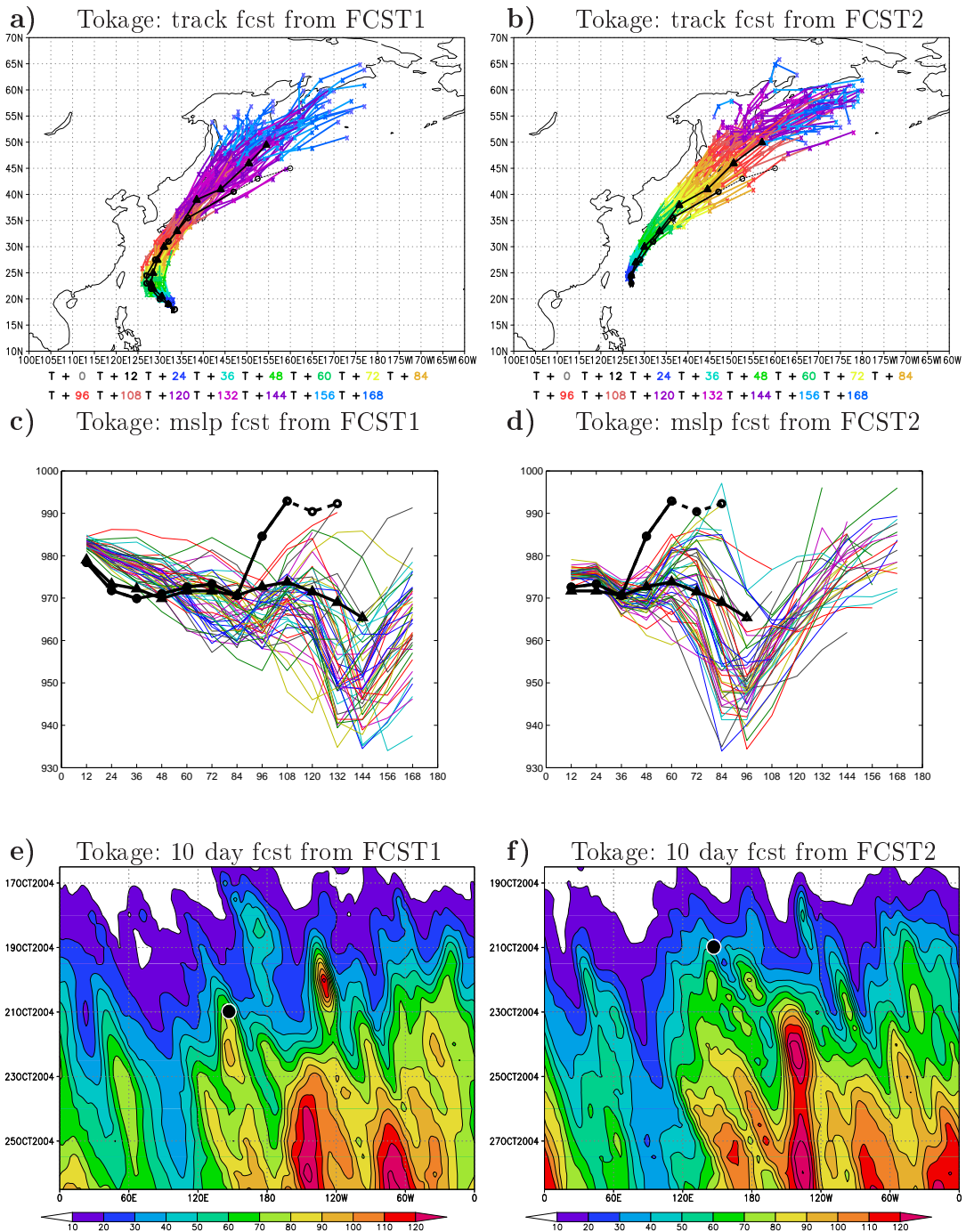


Figure 4.7: Top: as Fig. 4.5 a, b for Tokage. Middle: analysis (black line with circles), deterministic forecast (black line with triangles) and ensemble forecast (colors) of the central surface pressure of Tokage from c) FCST1 and d) FCST2 for 5 days. Bottom: as Fig. 4.5 c, d for Tokage.

4.2.2 Weak events

The variability within ensemble forecasts for TCs Saola and Philippe exhibit similar behavior as for the major TCs in that there are plumes of high uncertainty associated with the ET events and downstream of them. In the minor TC cases the main source of variability is the interaction of the ex-TC with a large-scale midlatitude low pressure system. Different realizations of this interaction could be characterized by either the ex-TC or the midlatitude low intensifying after merger, or two systems of similar strength merging. Furthermore, a distinct amount of ensemble members forecast a decay of the TC and a reintensification of the midlatitude low without an interaction between the two.

Saola

In the ensemble track forecast of Saola from FCST1 (Fig. 4.8 a) only a few ensemble members recurve and only six of them interact with the midlatitude flow. The deterministic forecast agrees with the majority of the ensemble members and does not predict the recurvature while the six members that contain the recurvature are grouped around the analysis. Thus, a low probability is assigned to the recurvature by the ensemble. In FCST2, however, there is better agreement among the ensemble members, with all having about the same direction of motion. Nevertheless, a closer inspection shows that Saola cannot be identified after 36 to 48 h in many members that lie on the southern edge of the plume of tracks. In the deterministic forecast Saola moves in the same direction as in the analysis, but whereas the final analyzed position of Saola is 140° E and 40° N on 0000 UTC 27 September, Saola reaches that position 24 h later in the deterministic forecast.

The Hovmoeller plot from FCST1 for Saola (Fig. 4.8 c) shows a distinct maximum in values of standard deviation downstream of the ET event around 48 h after ET at about 160° W. This maximum is caused by uncertainty in the ensemble associated with the prediction of a midlatitude trough with which Saola will interact (black triangle). In the ensemble forecast, however, the uncertainty at 160° W cannot be attributed to Saola because the TC enters the latitude band between 40° N and 50° N in only six of the 51

ensemble members. Thus, the Hovmoeller plot does not show much uncertainty associated with the ET of Saola itself (black dot). In FCST2 (Fig. 4.8 d), however, a weak plume of higher standard deviation can be seen on 1200 UTC 26 September at about 175° W emanating from the ET of Saola. The highest variability develops following the interaction of Ex-Saola (black triangle) with the midlatitude trough.

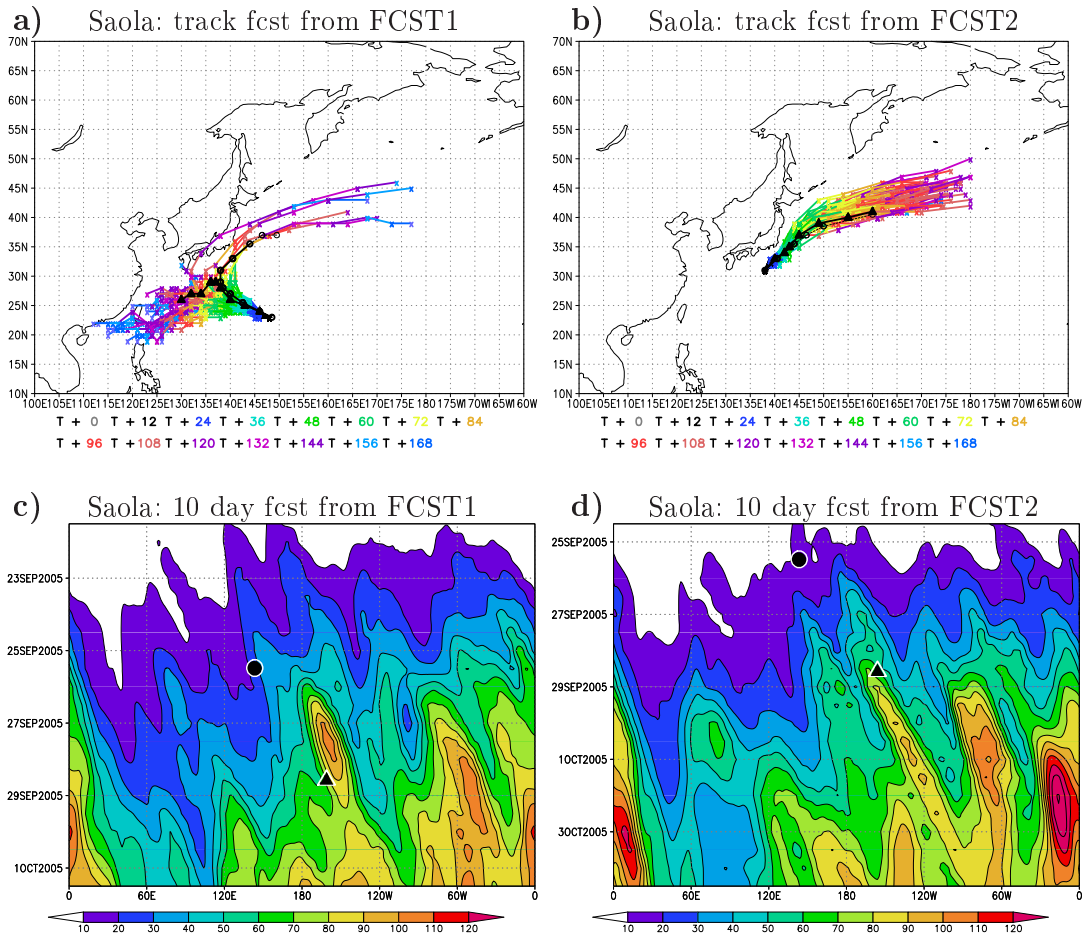


Figure 4.8: As Fig. 4.5 for Saola. ET-position is marked by a black dot, analyzed position of absorption of remnants of Saola is marked by a black triangle.

Philippe

A large spread can be seen in the ensemble track forecasts for Philippe (Fig. 4.9 a, b). In FCST1 (Fig. 4.9 a) Philippe decays south of 30° N without recurving in the western ensemble members, but recurves north of 30° N in the eastern ones. The deterministic

forecast track lies on the eastern edge of the ensemble tracks and shows a recurvature. Only one ensemble member lies to the east of the deterministic forecast from 0000 UTC 23 September. Two of the recurving ensemble members follow the deterministic forecast quite well. In the analyzed track Philippe is located at the edge of the ensemble envelope but close to the deterministic forecast. However, Philippe decays on 1200 UTC 23 September, whereas it can be identified for an additional two days in the deterministic forecast. In FCST2 (Fig. 4.9 b) more members recurve and do so farther south. A lot of the members decay after 144 h forecast time. One member is very similar to the deterministic forecast that shows Philippe far to the east after 168 h. For both of these forecast times Philippe can be identified in the deterministic forecast for a much longer time than in the analysis.

The variability in the environment of Philippe at the time of its decay cannot be shown in the Hovmoeller plots (Fig. 4.9 c and d) because the TC is situated south of the latitude band of 40° - 50° N. A white circle denotes Philippe's longitudinal location on 1200 UTC 23 September. The plume of higher standard deviation that can be seen for FCST1 (Fig. 4.9 c) from 22 September at about 65° W and for FCST2 (Fig. 4.9 d) from 23 September at about 55° W is due to variability associated with a midlatitude trough. This midlatitude trough formed a weak cut-off low (at about 70° W and 30° N in Fig. 4.4 a) that steered the remnants of Philippe to the north. On 1200 UTC 27 September, (i. e. the time when the cold low that had been reinforced by Philippe merged with the large-scale midlatitude low pressure system), a prominent maximum of standard deviation can be seen in both Hovmoeller plots. Thus, large uncertainty in the ensemble is associated with the different realizations of the merger and the development thereafter. The values in the maximum for FCST2 are lower than in FCST1 and the area of highest variability is narrower.

In general, an operational forecaster might give more weight to the high resolution deterministic forecast because it is more likely to capture small scale systems like TCs that undergo ET. For example, in the case of Philippe a forecaster might suggest that the ensemble cannot resolve Philippe. These two minor TC cases suggest that ensemble forecasts both assign probabilities to the deterministic forecast and indicate atmospheric developments that are possible even if they are not very probable. This study shows

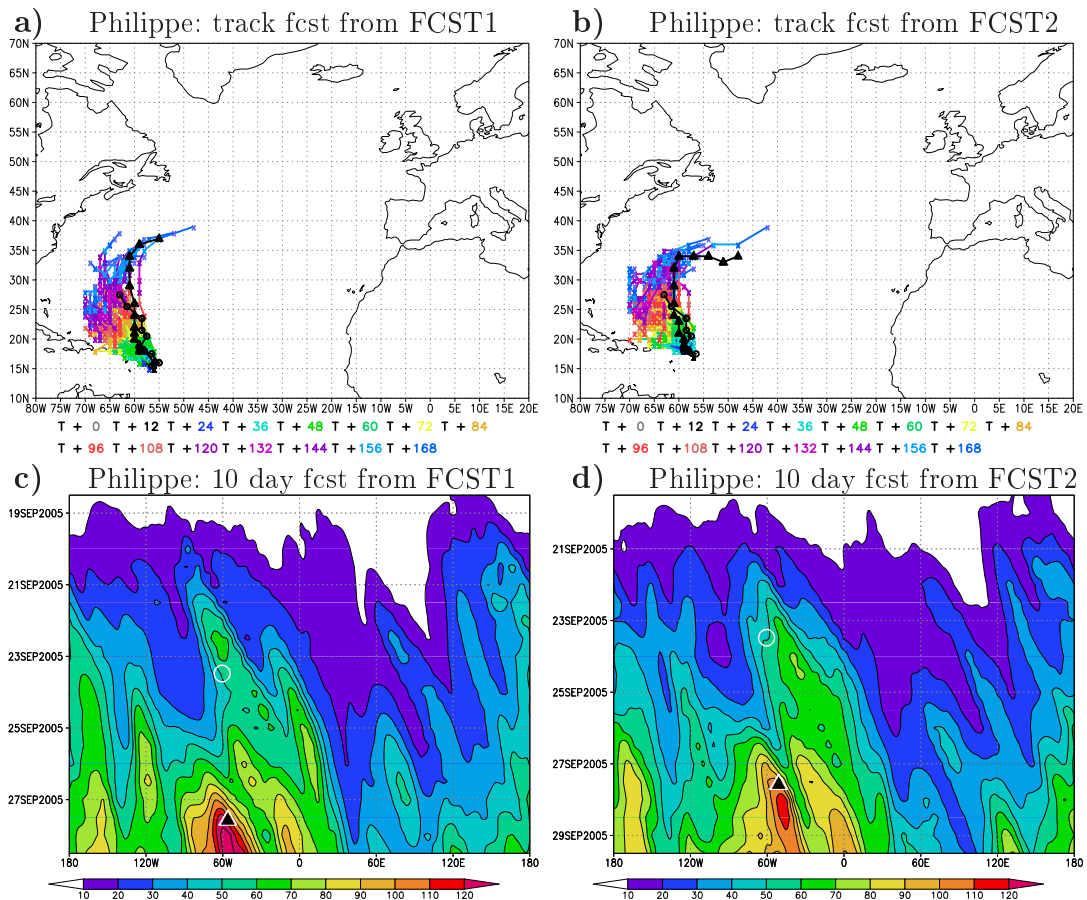


Figure 4.9: As Fig. 4.5 for Philippe. Position of decay of Philippe is marked by a white circle, position of absorption of remnants is marked by a black triangle.

that for the case of Philippe the forecaster should regard the deterministic forecast with caution. In Saola's case the recurvature was already indicated in the ensemble forecast 3 days prior to its occurrence while the deterministic forecast did not predict it until its onset.

4.3 The analysis method

In section 4.2 an increase of standard deviation among the ensemble members (i. e. a decrease in predictability) associated with the 5 investigated ET events was found. The ensemble forecast becomes less uncertain when the forecast time is close to or at the time of recurvature. To gain insight into the source of these uncertainties the regions of

high standard deviation are examined with regard to recurring patterns. For this purpose ensemble members that show similar developments and intensities of ET and of the up- and downstream flow should be combined to groups within an ensemble. A large number of groups defines a variety of different atmospheric flow patterns. It is hypothesized that the number of groups decreases as the predictability increases.

4.3.1 Patterns of variability

Several authors have used techniques to quantify the probability distribution of the state of the atmosphere in multidimensional phase space. The aim of these methods is to find patterns where the variability in a particular variable over space is highest, also called the „centers of action“ (Björnsson and Venegas, 1997), and the contribution of the individual atmospheric flow patterns to these patterns of high variability. In the current work the method of empirical orthogonal function (EOF) analysis (Lorenz, 1956) also called principal component analysis (PCA) is used to find the centers of variability. The principal components (PCs) are often used to investigate the time variation of the EOFs. In our case, however, the variation from ensemble forecast to ensemble forecast of a selected variable is of more interest. Therefore, the PCs are considered as change of the EOFs with the ensemble members. To calculate the EOFs the potential temperature on the dynamical tropopause as mentioned in section 4.1 was used.

The first step in calculating the EOFs for one ensemble forecast of a variable \mathbf{x} in a particular area around an ET event and the ocean basin downstream of it is to calculate anomalies from the ensemble mean of this variable. The matrix is arranged such that one row consists of the anomalies in one ensemble member at all the $1, \dots, G$ grid points and one column consists of the anomalies at one specific grid point in all the $1, \dots, \epsilon$ ensemble

members.

$$\mathbf{X}' = \begin{pmatrix} x'_{11} & x'_{12} & \cdots & x'_{1G} \\ x'_{21} & x'_{22} & \cdots & x'_{2G} \\ \vdots & \vdots & \ddots & \vdots \\ x'_{\epsilon 1} & x'_{\epsilon 2} & \cdots & x'_{\epsilon G} \end{pmatrix}$$

The individual rows can be regarded as maps shown by the individual ensemble members (Björnsson and Venegas, 1997). The anomalies x'_{ij} from the ensemble mean of the model variable \mathbf{x} at each grid point are

$$\mathbf{X}' = \mathbf{X} - \frac{1}{\epsilon}[\mathbf{1}]\mathbf{X} \quad (4.2)$$

\mathbf{X} is the matrix of values at each grid point for each ensemble member, $[\mathbf{1}]$ is a defined $\epsilon \times \epsilon$ matrix with all elements equal to 1.

The next step is to find the spatial covariances of the anomalies of the entire ensemble. Therefore, the variance-covariance matrix Φ is calculated by transposing \mathbf{X}'

$$\Phi = \frac{1}{\epsilon - 1} \mathbf{X}'^T \mathbf{X}' \quad (4.3)$$

The variance-covariance matrix is also called the dispersion matrix because it describes how the anomalies are dispersed around the ensemble mean (Wilks, 1995). To get the regions of the maximum covariance or dispersion of the anomalies an eigenvalue analysis has to be performed on Φ .

$$\Phi \mathbf{C} = \Lambda \mathbf{C} \quad (4.4)$$

where the \mathbf{c}_i column vectors of \mathbf{C} are the eigenvectors of Φ corresponding to the eigenvalues λ_i which are the trace of Λ . The eigenvalue λ_i determines the factor by which the eigenvector \mathbf{c}_i is stretched. Both Λ and \mathbf{C} are $G \times G$ matrices. These eigenvectors are the EOFs. The EOFs are uncorrelated in space, i. e. they are orthogonal $\mathbf{C}^T \mathbf{C} = \mathbf{1} = \mathbf{C} \mathbf{C}^T$. They are arranged according to the percentage of the total variability they express so that the first one points in the direction of the highest percentage of total variability, the

second one in the direction of the second highest and so on. The eigenvectors can be seen as a new coordinate system with its axes along the joint variability of the data.

The principal components, which yield the quantitative amount of the total variability, are obtained through the projection of the anomalies \mathbf{x}' onto the EOFs \mathbf{c}_i

$$\nu_m = \mathbf{c}_m^T \mathbf{x}' = \sum_{i=1}^G c_{im} x'_i \quad m = 1, \dots, Z \quad (4.5)$$

ν_m is the m th principal component. Z is the number of principal components needed to describe the total variability. The principal components account successively for the maximum amount of the joint variability. In general, the total variability is explained by much fewer PCs than there are dimensions in the original coordinate system, i. e. $Z \ll G$. Thus, the calculation of the PCs of a system with many dimensions reduce it to a system of much fewer dimensions containing, nevertheless, all the physical information of the original system. Relating this to the variability in the ensemble, it can be said that the spatial patterns of variability, i. e. the regions in the investigated domain, in that the main variability can be found, are determined by the EOFs. The verification of these patterns shown by the individual ensemble members are given by the PCs, i. e. the contribution of each ensemble member to the EOFs is given through the PCs.

4.3.2 Fuzzy clustering

It is straightforward to assume that individual ensemble members that have PCs, i. e. contributions to the patterns of main variability, with the same sign and about the same strength have similar synoptic developments. Therefore, grouping members with similar PCs together should give information about the possible evolutions in the atmospheric flow and assign probabilities to them according to the number of ensemble members contributing to them.

A variety of methods to perform this grouping is proposed by several authors. Cheng and Wallace (1991) used a hierarchical clustering on the two leading EOFs to find spatial patterns in 500 hPa height fields. Hierarchical clustering is a method that starts with as

many clusters as members exist and groups iteratively two clusters together that subsequently form a new cluster (Fig. 4.10). This is continued until all members are grouped into one cluster. A measure has to be determined after which to stop the merging. This could be for example a distinct increase of distance between the point of merger of one cluster with another compared with its previous point of merger as in Fig. 4.10. In other words the clustering is stopped if the remaining clusters exhibit too much differences from each other.

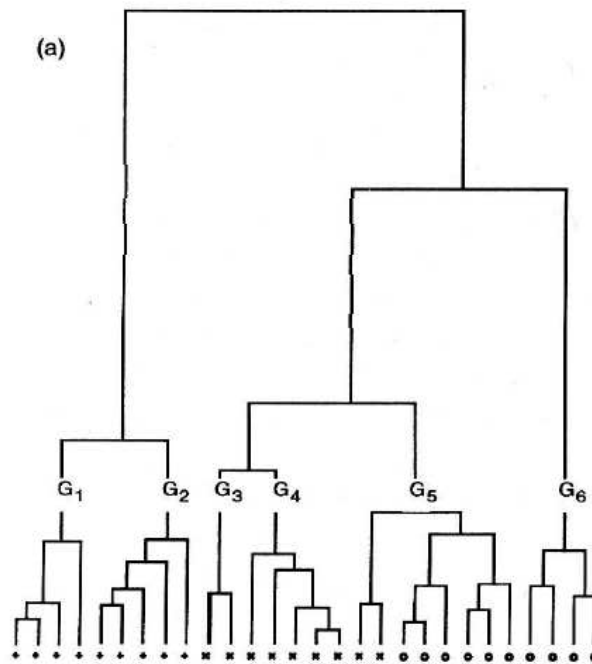


Figure 4.10: Hierarchical clustering of n points (Wilks, 1995). $G_1 - G_6$ denote the resulting clusters. The distance between the clusters before they are merged is indicated by the distance of the points of merger from the previous point of merger or the initial n clusters. $+$, x , and o may be different stations (northern, southern, western) in case of a clustering of maximum temperature.

Mo and Ghil (1988) performed a non-hierarchical clustering in a seven dimensional phase space defined by the principal components of the leading EOFs of a temporal correlation matrix on planetary 500 hPa height fields. The method used in this study falls among the non-hierarchical clustering. To start the iterative cluster procedure a pre-defined number of cluster centers called centroids are set arbitrarily in a phase space diagram (Fig. 4.11). In this study the clustering is performed on the first two PCs of the

leading two EOFs of each ensemble member to arrange the ensemble members in groups. These groups exhibit similar structures of the potential temperature on the dynamical tropopause at a specific time. Hence, each of the 51 ECMWF ensemble members corresponds to one point in the phase space described by its values of the first two PCs. In other words, each ensemble member is represented by the pair of PC values. The members are assigned to their closest centroid with regard to a certain measure of the distance.

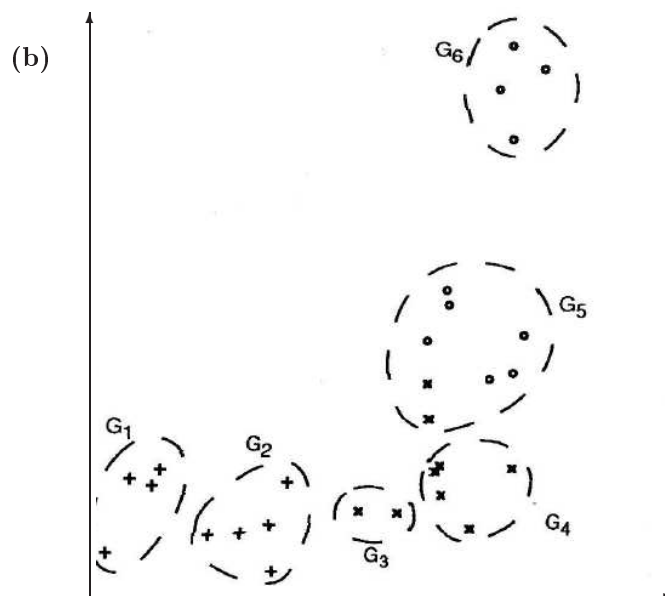


Figure 4.11: Non-hierarchical clustering (Wilks, 1995). Scatterplot of n points. The number of clusters $G_1 - G_6$ has been predefined. As in Fig. 4.10 $+$, x , and \circ may be different stations (northern, southern, western) in case of a clustering of maximum temperature.

In contrast to a hard clustering, in which every member is assigned to one cluster, the method used here is a fuzzy clustering method. In fuzzy clustering some members that cannot be assigned clearly to one cluster are not assigned to any cluster. Each of the members is provided with a weight by which the strength of their membership in their clusters is determined (Harr et al., 2007). For a point k the weight associated with cluster i is defined as

$$w_{i,k} = \frac{1}{\sum_{j=1}^N \left(\frac{d_{i,k}}{d_{j,k}} \right)^{\frac{2}{q-1}}} \quad (4.6)$$

$d_{i,k}$ is the distance between point k and the centroid of cluster i , $d_{j,k}$ is the distance of the

point k to all the other clusters j , N is the total number of clusters and q is a fuzziness coefficient that has been set to 1.5.

Each ensemble member has as many of these weights or „membership factors“ as there are centroids. The mean and standard deviation of the highest membership factor of all 51 ECMWF members is calculated. Ensemble members whose highest membership factor is more than one standard deviation below this mean are not assigned to any cluster. These members lie in boundary regions between clusters. The other members are assigned to the cluster for which their membership factor is highest.

In the resulting groups each center is recalculated and becomes the new centroid. After this step the members are rearranged according to their smallest distance to the new centroids. This procedure is repeated until no ensemble member is reassigned anymore. An important advantage of the non-hierarchical clustering is that, in contrast to the hierarchical method, the members can be rearranged, i. e. the members can change the cluster during the clustering procedure.

To determine the optimal number of centroids the procedure was started with 2 clusters. Their charts of the potential temperature on the dynamical tropopause and the surface pressure were examined to see if the atmospheric patterns are different. If that is the case one centroid is added such that the clusters split into three and so on. If the newly added cluster does not exhibit distinct differences to the former ones the clustering is stopped.

4.4 Clustering the ensemble members

The analysis method described in the previous chapter is applied to all 5 cases. The EOFs are calculated for each case for one time at which a noticeable increase in the ensemble standard deviation could be seen in the plume originating from the ET location on the Hovmoeller plot. As in Harr et al. (2007) this time is referred to as the investigation time. The time of maximum standard deviation in the plumes was not used because this occurred typically several days after ET. For this later time it would probably not be possible to depict the different ET-scenarios that are responsible for the variability in the

ensemble members. The investigation times for the 5 cases can be found in Table 4.1.

4.4.1 The empirical orthogonal functions

In all five cases the main variability as depicted by the first two EOFs is caused by different representations of the trough-ridge-trough pattern described in section 4.1. The EOFs describe the east-west shift of the pattern, the horizontal tilt of the troughs and the ridge and their amplitude.

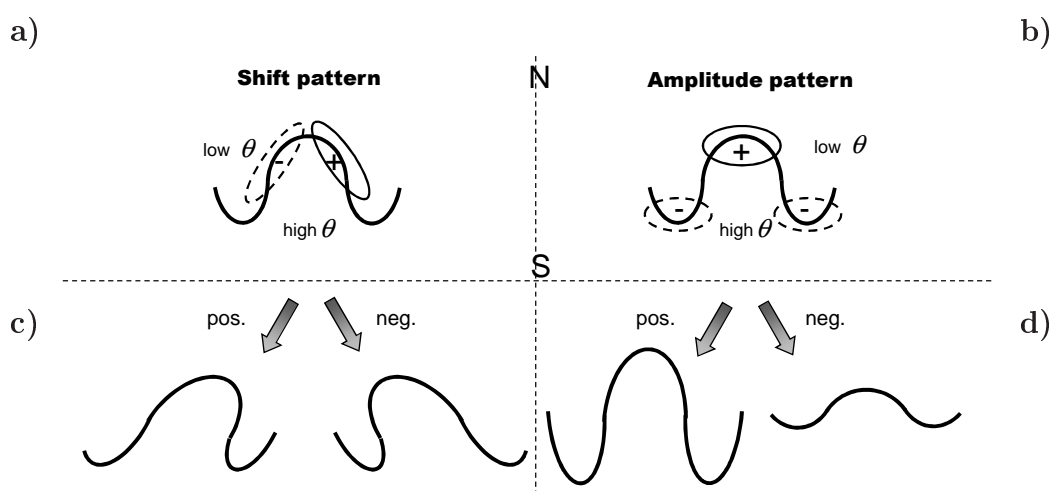


Figure 4.12: Schematic of the first two EOFs (top) denoting a) the shift and b) the amplitude pattern. The dynamic tropopause is represented schematically. The thick black line represents the strong potential temperature gradient in the midlatitudes. South of it the potential temperature values should be high, north of it they should be low. Synoptic patterns that result from the contribution to c) the shift and d) the amplitude pattern.

In Fig. 4.12 a, b the variability patterns are illustrated by a schematic of the dynamic tropopause. The thick black line signifies the strong potential temperature gradient on the tropopause. High values of potential temperature are to the south and low values to the north of this line. One of the first two EOFs has maxima with opposite signs in

the front and the rear of the ridge. The other one shows variability at the crest of the ridge and in the up- and downstream trough. In Fig. 4.12 c it is indicated that a positive contribution to the shift pattern represents an eastward shift and a negative contribution to the shift pattern a westward shift. Fig. 4.12 d denotes that a positive contribution to the amplitude pattern represents an amplification of the ridge and a negative contribution a flattening of the ridge. This can be understood considering that a positive contribution always amplifies the maxima according to their respective signs. A negative contribution counteracts the signs of the maxima. Since EOF1 and EOF2 can be related to either a shift in the pattern or a change in amplitude, they will be referred to in the following as shift and amplitude patterns.

In Fig. 4.13 and 4.14 EOFs 1 and 2 are superimposed on the ensemble mean of the potential temperature on the dynamic tropopause at the investigation time of FCST2 for Saola and at FCST1 for the other TCs. Note that the signs at the centers of action are arbitrary and defined for each case by the respective principal component.

For Maemi the centers of action of EOF1 (Fig. 4.13 a) are located at the front and rear of the ridge almost exactly as in Fig. 4.12. Thus, a positive contribution of an ensemble member to EOF1 would mean a shift or at least a tilting of the pattern to the east (Fig. 4.12 c, left) and a negative contribution a shift or tilting to the west (Fig. 4.12 c, right). In EOF2 (Fig. 4.13 b) a region with strong positive values is situated at the crest of the ridge and two small regions with weak negative values can be found at the bases of the troughs. Here a positive contribution would enhance the amplitude of the ridge and deepen the troughs (Fig. 4.12 d, left) while a negative contribution would flatten the ridge and weaken the troughs (Fig. 4.12 d, right). In the case of Maemi, the shift and amplitude patterns are separated optimally in the EOFs.

For Fabian the EOFs (Figs. 4.13 c and d) show similar characteristics. At the rear of the ridge a region of strong positive values can be found in EOF1 (Fig. 4.13 c). This center of action describes the variability in the cyclonic wrap-up of the upstream trough and resembles the upstream part of the shift pattern (Fig. 4.12 a). Negative values are seen at the crest of the ridge similar to parts of the amplitude pattern (Fig. 4.12 b) and

extend along the gradient at the rear of the downstream trough as the downstream part of the shift pattern (Fig. 4.12 a). Therefore EOF1 describes a mixture of the variability in amplitude and shift. As in the case of Maemi, EOF2 for Fabian (Fig. 4.13 d) describes the variability in the location and tilt of the ridge. A large region of positive values at the crest of the ridge and strong negative values at the base of the upstream trough slanting slightly to the rear of the ridge can be seen. Thus, as for Maemi, EOF2 describes mainly the amplitude of the pattern (Fig. 4.12 b).

EOF1 of Tokage (Fig. 4.13 e) is very similar to EOF1 of Maemi at first view. However, the region of positive values at the front of the ridge is stronger and larger in scale than the negative values at the rear of the ridge. A part of the positive values extend to the crest of the ridge. From this perspective EOF1 would describe mainly variability in the shift of the ridge (Fig. 4.12 a) and to a small part variability in the amplitude (Fig. 4.12 b). EOF2 of Tokage (Fig. 4.13 f) shows two regions of variability with opposed sign at the crest of the ridge. At closer inspection it is seen that the negative values lie polewards of the strong gradient of potential temperature and the positive values equatorwards. The negative values situated north of the positive extend down into the downstream trough. To one part this pattern describes variability in the amplitude pattern (Fig. 4.12 b) especially in the depth of the downstream trough. To the other part variability in the gradient of potential temperature describing the shape of the ridge is shown by EOF2 of Tokage.

The EOFs for the minor TCs have in common that EOF1 describes variability in the amplitude and EOF2 in the shift in contrast to the EOFs of the major TCs. Furthermore, the centers have smaller horizontal scales and their values are weaker.

For Saola (Figs. 4.14 a and b) the ensemble mean exhibits a rather zonal structure in the midlatitudes. The patterns with the highest and second highest contribution to the total variability oppose that for Maemi. The amplitude pattern described by EOF1 is very similar to EOF2 of Maemi. EOF2 describes variability in the shift of the long shallow ridge.

During Philippe's lifecycle the ensemble forecasts exhibited high variability in the mid-latitude flow that was unrelated to Philippe. Because the contribution of the ensemble

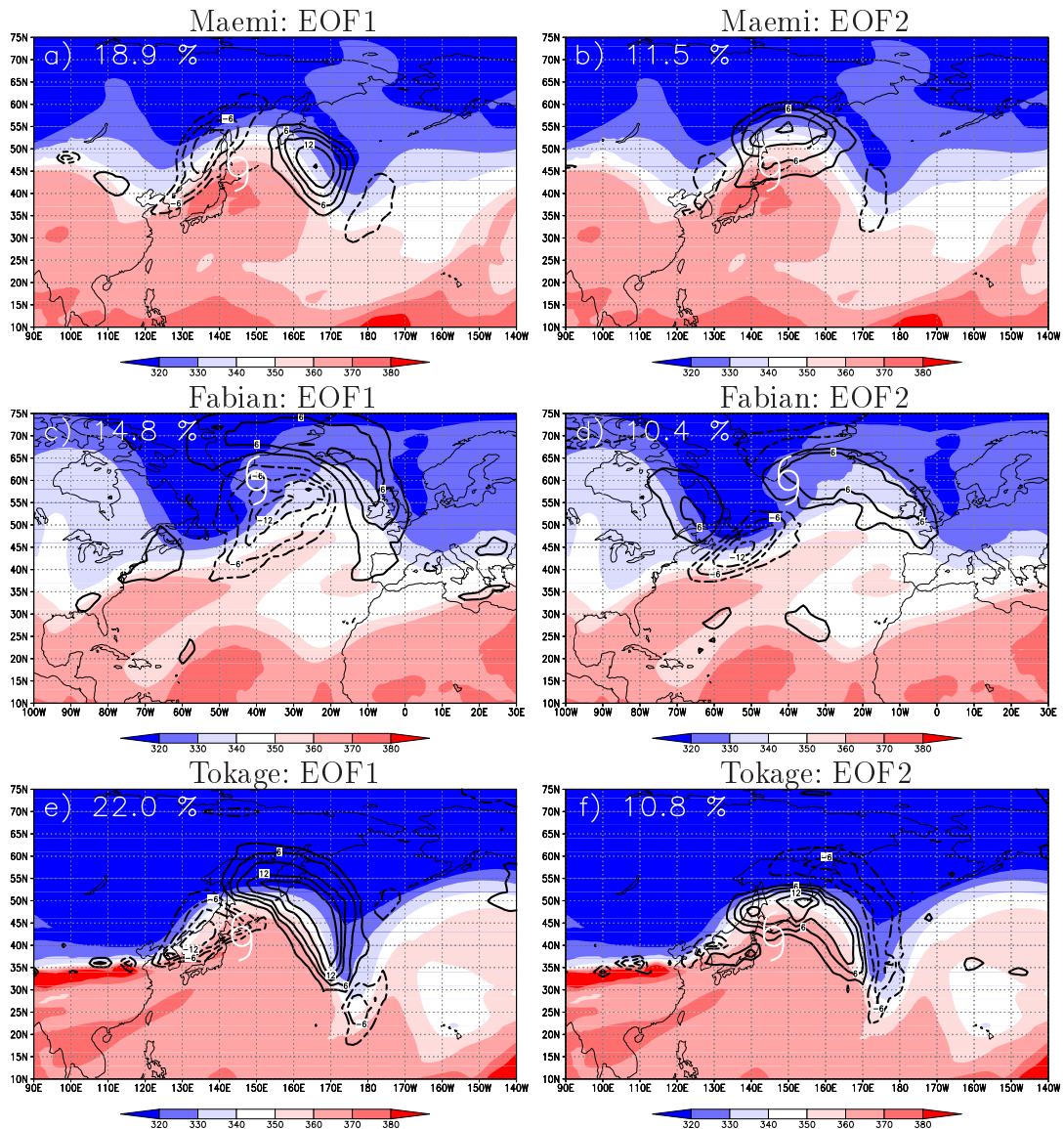


Figure 4.13: Ensemble mean of potential temperature on the dynamic tropopause (shaded, K) for Maemi (top), Fabian (middle) and Tokage (bottom) for FCST1 (Table 4.1). EOF1 (left) and EOF2 (right) are shown in contours at an interval of 3.0 K. The percentage of their contribution to the total variability is marked in white in the top left corner.

members to the variability associated with Philippe is the matter of interest, the region for which the EOFs were calculated was confined to $50^{\circ} - 80^{\circ} \text{ W}$ and $10^{\circ} - 40^{\circ} \text{ N}$. In this region EOF1 and EOF2 represent over 30 % of the total variability both in FCST1 and FCST2. For reasons of symmetry the same domain size as for the other four cases is shown. EOF1 has a region of positive values at the crest of the weak ridge directly

downstream of the TC and a small region of negative values in the upstream trough. In EOF2 a larger region of negative values is located in the weak upstream trough and the rim of a region of positive values can be seen around 50° W. EOF1 suggests variability in the amplitude of the trough-ridge pattern. The negative values in EOF2 describe to one part variability in the depth of the upstream trough and to the other variability in the shift of the ridge which has an inclined axis similar to Tokage.

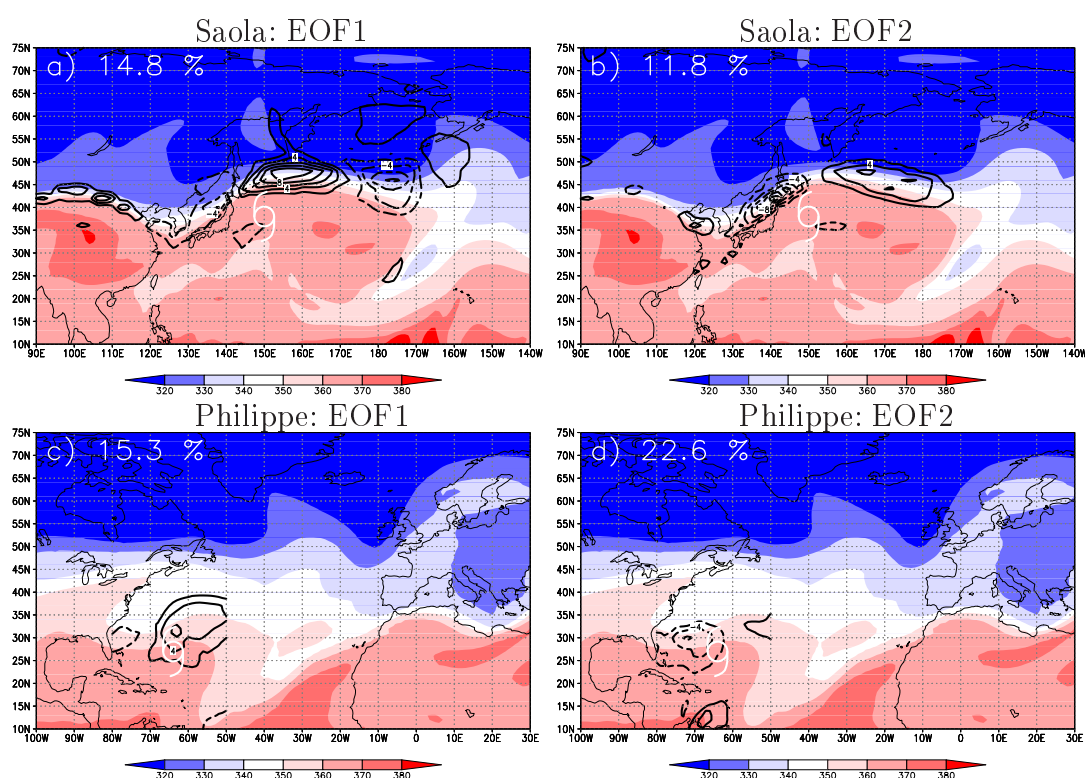


Figure 4.14: As Fig. 4.13 for Saola (top) and Philippe (bottom). FCST2 is shown for Saola and FCST1 for Philippe (Table 4.1). EOF1 (left) and EOF2 (right) are shown in contours at an interval of 2.0 K.

For the 5 cases studied here, EOF1 and EOF2 can be related to either a shift in the pattern or a change in the amplitude, and will be referred to in the following as shift and amplitude patterns.

4.4.2 The Clusters

The temporal evolution leading to the variability among EPS members and the further development of the members is examined by the fuzzy cluster analysis of the principal components associated with EOF1 and EOF2 explained in section 4.3.1 to describe the contribution of the individual ensemble members to the main variability. The combination of the principal component analysis with the clustering analysis has the advantage that the development of the grouped members before and after the time of investigation can be observed.

The numbers of clusters found for each case are presented in Table 4.2 for FCST1 and in Table 4.3 for FCST2. The number of clusters was always less for FCST2 than for FCST1. It was shown in section 4.2 that the variability was smaller for FCST2 in all the cases. This agrees with Harr et al. (2007) who hypothesize that the number of scenarios decreases as the forecast time approaches the ET time. Additionally, the percentage contribution of the shift and amplitude pattern to the total variability and the contribution of each of the clusters to these patterns is listed. In all cases the first two EOFs contribute about 25 % – 40 % to the total variability for FCST1 (Table 4.2) and 20 % – 30 % for FCST2 (Table 4.3). Hence, clustering EOF1 and EOF2 takes into account a large part of the total variability. For Philippe the percentage is highest, because the region of which the EOFs are calculated is smaller than for the other four cases.

As mentioned above, only the relative signs of the centers of action are important. To examine the links between the representation of the ET in the individual clusters and the contribution of each cluster to the EOFs the pattern of Maemi has been taken as a reference. The signs of the other cases have been changed accordingly as seen in Fig. 4.13 and 4.14. Thus a positive contribution to the shift pattern represents an eastward shift and a negative contribution to the shift pattern a westward shift. A positive contribution to the amplitude pattern represents an amplification of the ridge and a negative contribution a flattening of the ridge. The nature of the contribution to the EOF in question is given for each cluster in Table 4.2.

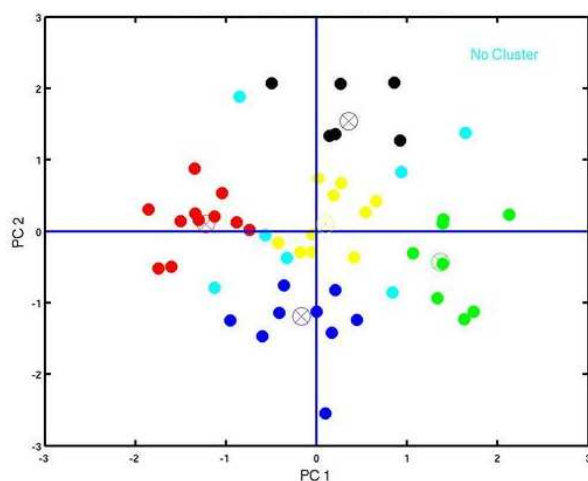


Figure 4.15: Ensemble members with the first (PC1) and second principal component (PC2) as new coordinates for the 5-cluster solution. The ensemble forecast was initialized at FCST1 and verifies at the investigation time of Maemi. Cluster centers are defined by circles with crosses. Turquoise points define ensemble members that do not belong to any cluster.

To illustrate the clustering of the principal components the phase space diagram for the PCs found for the ensemble forecast from FCST1 for Maemi is shown (Fig. 4.15). The optimal number of clusters following the criteria explained in section 4.3.2 for Maemi was 5. In the diagram the points are the 51 ensemble members with PC1 and PC2 as their new coordinates. Ensemble members assigned to a given cluster are denoted by the same colour. The turquoise dots denote ensemble members that do not belong to any cluster. Each of the Maemi clusters contributes either positively or negatively only to one of the variability patterns. The cluster denoted by yellow dots does not contribute to any of the variability patterns and, thus, is similar to the ensemble mean. Therefore, the five Maemi clusters are nice examples for the link of the contribution of the clusters to each of the variability patterns and the synoptic development (see next section). For a closer investigation of the individual clusters, the potential temperature on the dynamic tropopause and the surface pressure have been averaged in each cluster. The clusters have been investigated with regard to their representation of the ET, i. e. the strength of reintensification and the longevity of the resulting system, and to their downstream development. The conceptual model proposed by Klein et al. (2000) was used to define the strength of an ET in terms of the depth of the surface pressure after interaction with

Table 4.2: Number of Clusters for FCST1. Number of members in each of the clusters, percentage contribution of the shift and amplitude pattern to the total variability. Contribution of the individual clusters (+ positive, - negative, ++ strong positive contribution) to the respective variability pattern. Strength of ET: 0: No ET; 1: Little or no re-intensification, central mslp ≥ 1000 hPa; 2: Moderate re-intensification, central mslp 985 – 999 hPa; 3: Deep re-intensification, central mslp < 985 hPa.

	Cluster	Members	Shift pattern	Contrib.	Amplitude pattern	Contrib.	ET	Fig.
Fabian	3	15		-		+	3	4.16 a
		9	14.8 %	-	10.4 %	-	0	4.16 b
		19		+		o	3	4.16 c
Maemi	5	9		o		-	1	4.4.2 a
		6		o		+	3	4.4.2 b
		8	18.9 %	+	11.5 %	o	2	4.4.2 c
		10		o		o	3	4.4.2 e
		11		-		o	3	4.4.2 d
Tokage	3	3		++		-	3	4.18 a
		22	22.8 %	+	10.8 %	+	3	4.18 b
		16		-		-	3	4.18 c
Saola	2	27		-		-	0	/
		19	11.5 %	+	13.0 %	+	0	/
Philippe	5	10		+		+	1	4.4.2 a
		8		o		-	0	4.4.2 e
		7	15.3 %	+	22.6 %	-	0	4.4.2 b
		8		-		-	0	4.4.2 c
		3		-		++	3	4.4.2 d

the midlatitudes (see Table 4.2). However, the upper limit for a deep reintensification was raised by 5 hPa to account for the comparatively low resolution of the ensemble forecast. Thereafter, 0 is assigned to a TC that is decaying without ET, 1 to a TC undergoing ET and re-intensifying weakly or not at all (mslp ≥ 1000 hPa), 2 to a TC re-intensifying

Table 4.3: As Table 4.2 for FCST2.

	Clusters	Members	Shift pattern	Contrib.	Amplitude pattern	Contrib.	ET	Fig.
Fabian	2	22		+		-	3	/
		21	11.2 %	-	9.1 %	+	3	/
Maemi	2	24		+		-	2	/
		19	16.9 %	-	9.4 %	+	2	/
Tokage	3	11		+		+	3	/
		15	12.4 %	-	8.5 %	o	3	/
		18		o		-	3	/
Saola	2	20		+		+	1	4.21 a
		22	11.8 %	-	14.8 %	-	0	4.21 b
Philippe	2	21		-		-	0	/
		22	14.5 %	+	16.8 %	+	1	/

moderately after ET (mslp 985 – 999 hPa) and 3 to a TC re-intensifying strongly after ET (mslp < 985 hPa).

For the five cases some remarkable similarities can be found between clusters with the same sign of their contribution to the EOFs. For the strong events the different atmospheric developments are clearly associated with the position and intensity of the TC relative to the midlatitude flow and with the shape of the midlatitude trough-ridge-trough pattern which is influenced by the TC. For the weak cases, Saola and Philippe, the differences in the clusters base mainly on the variability in the midlatitude flow and not so much on the intensity and location of the TC. This is due to the weak representation of these minor TCs in the model fields. It is to be expected, since in the analyses (section 4.1.2) it could be seen that in both cases the midlatitudes play the dominant role for the ET event and for the absorption of the remnants. The pattern which describes the highest percentage of variability is the shift pattern for the strong cases and the amplitude pattern for the weak cases.

Note that the fifth Maemi cluster does not contribute to the variability patterns and thus its dynamical tropopause has a similar orientation like the ensemble means with regard to the shift and the amplitude of the trough-ridge-trough pattern.

Note further that FCST1 for Saola builds an exception insofar as there is no interaction of Saola with the midlatitude flow in most of the ensemble members, as seen in section 4.2.2. In this case applying the analysis method to the ensemble forecast for this investigation time does not yield meaningful results with respect to different representations of ET. Thus, only FCST2 for Saola is discussed in the following.

Since the ensemble members have been clustered based on the variability patterns situated in a smaller region in the case of Philippe the different representation of the trough-ridge pattern in the clusters refers to the trough at about $70^{\circ} - 80^{\circ}$ W and $30^{\circ} - 35^{\circ}$ N and the ridge at about $50^{\circ} - 70^{\circ}$ W and $30^{\circ} - 35^{\circ}$ N (Fig. 4.4.2).

Positive shift pattern

The clusters that contribute positively to the shift pattern (Figs. 4.16 c, 4.4.2 c, 4.18 a, b, 4.21 a, 4.4.2 a, b) are either in a mature state or have decayed already. In each positively shifted case the associated ridge on the dynamic tropopause is tilted southwest-northeast (Figs. 4.4.2 c, 4.18 b) or is significantly eroded (Figs. 4.16 c, 4.18 a). Considering the temporal evolution (not shown) it is seen that these positive contributors to the shift pattern develop and decay quickly. The systems reintensify deeply in the Fabian-cluster and in both Tokage-clusters and moderately in the Maemi-cluster.

Figs. 4.16 c and 4.18 a resemble the cyclonic paradigm of baroclinic wave life cycle in its decaying state (Thorncroft et al., 1993; Davis and Emanuel, 1991). Fig. 4.4.2 c contains elements of both cyclonic and anticyclonic paradigms. The southern portion of the upstream trough ($115^{\circ} - 140^{\circ}$ E) is bent back anticyclonically whilst the northern portion is beginning to wrap up cyclonically. Subsequently, the southern anomaly thins and the cyclonic wrap up becomes more pronounced (not shown). A positive contribution to the shift pattern favors the formation of a cut-off low. This can be seen in Figs. 4.18

a and b. The ridge is strongly tilted to the east and the trough that has interacted with Tokage shows only a weak cyclonic wrap-up of its northern portion. The formation of a cut-off low at about 175° E is nearly completed.

In the weak cases that contribute positively to this pattern the ridge is rather shifted than tilted downstream. The clusters show the upper-level ridge directly downstream of the TC shifted to the east compared to the ensemble mean. In combination with the positive contribution to the amplitude pattern (Figs. 4.21 a and 4.4.2 a), which will be described below, this leads to the ET being in a favorable region for re-intensification. The ex-TCs move into regions close to the potential temperature gradient and re-intensify weakly in these two clusters. In Fig. 4.4.2 b the trough-ridge pattern looks rather similar to that in Fig. 4.4.2 a but has a weaker amplitude. In this cluster Philippe has already moved south of the trough and decays 12 hours later.

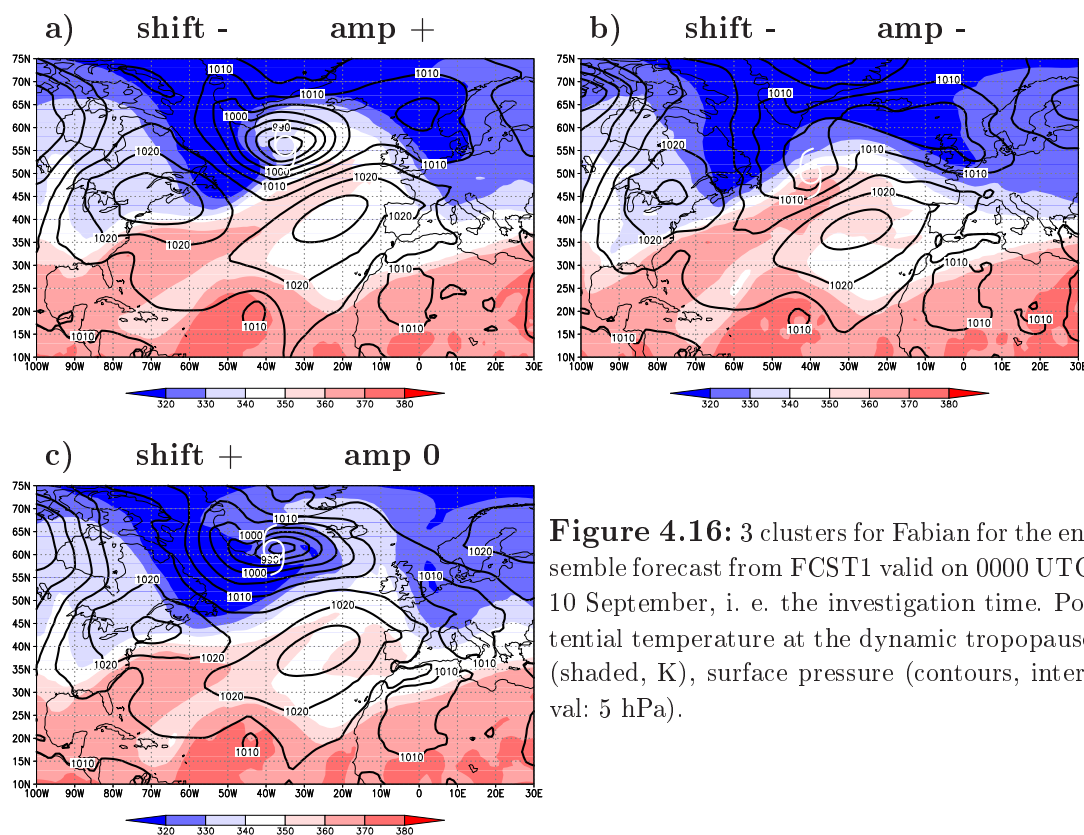


Figure 4.16: 3 clusters for Fabian for the ensemble forecast from FCST1 valid on 0000 UTC 10 September, i. e. the investigation time. Potential temperature at the dynamic tropopause (shaded, K), surface pressure (contours, interval: 5 hPa).

Negative shift pattern

In contrast, the negative contributors to the shift pattern (Figs. 4.16 a, b, 4.4.2 d, 4.18 c, 4.21 b, 4.4.2 c, d) represent a delayed development of the ET system because the westward shift results in a later interaction with the upstream trough. Fig. 4.16 b will be discussed later because, through its negative contribution to the amplitude pattern, it shows a decay without ET. In the other 3 cases the troughs have begun to wrap up cyclonically as in the cyclonic paradigm and the ridges are oriented meridionally. The surface pressure shows the systems either in their early stage of ET (up to 24 h before peak intensity) or just reaching their peak intensity. Subsequently, they reintensify strongly and develop into persistent almost stationary systems after interaction with the midlatitudes (e. g. for Tokage in Fig. 4.19). Moreover, the north-south orientation of the ridges and the nearly stationary ET-systems allow the downstream troughs to persist and the associated downstream surface pressure systems (at about $140^{\circ} - 160^{\circ}$ W in Fig. 4.19 b) to intensify.

The weak cases show the upper-level trough-ridge pattern farther to the west compared to the ensemble mean. In the case of Saola, this results in a position of the ex-TC which is not favorable for re-intensification because it is well east of the upstream trough. The TC weakens further and is absorbed subsequently by the midlatitude system downstream. For Philippe this combination of a negative contribution to the shift pattern and a strong positive contribution to the amplitude pattern (as will be described below) gives a particularly favorable configuration for a strong ET in this smallest cluster. However, comparing this cluster with Fig. 4.4.2 c, in which Philippe has already decayed, illustrates, however, that a positive contribution to the amplitude pattern is essential for recurvature and strong re-intensification.

Time development: Shift pattern

The different rate of baroclinic development of the ET systems in the clusters that contribute positively and negatively to the shift pattern can be observed by investigating the

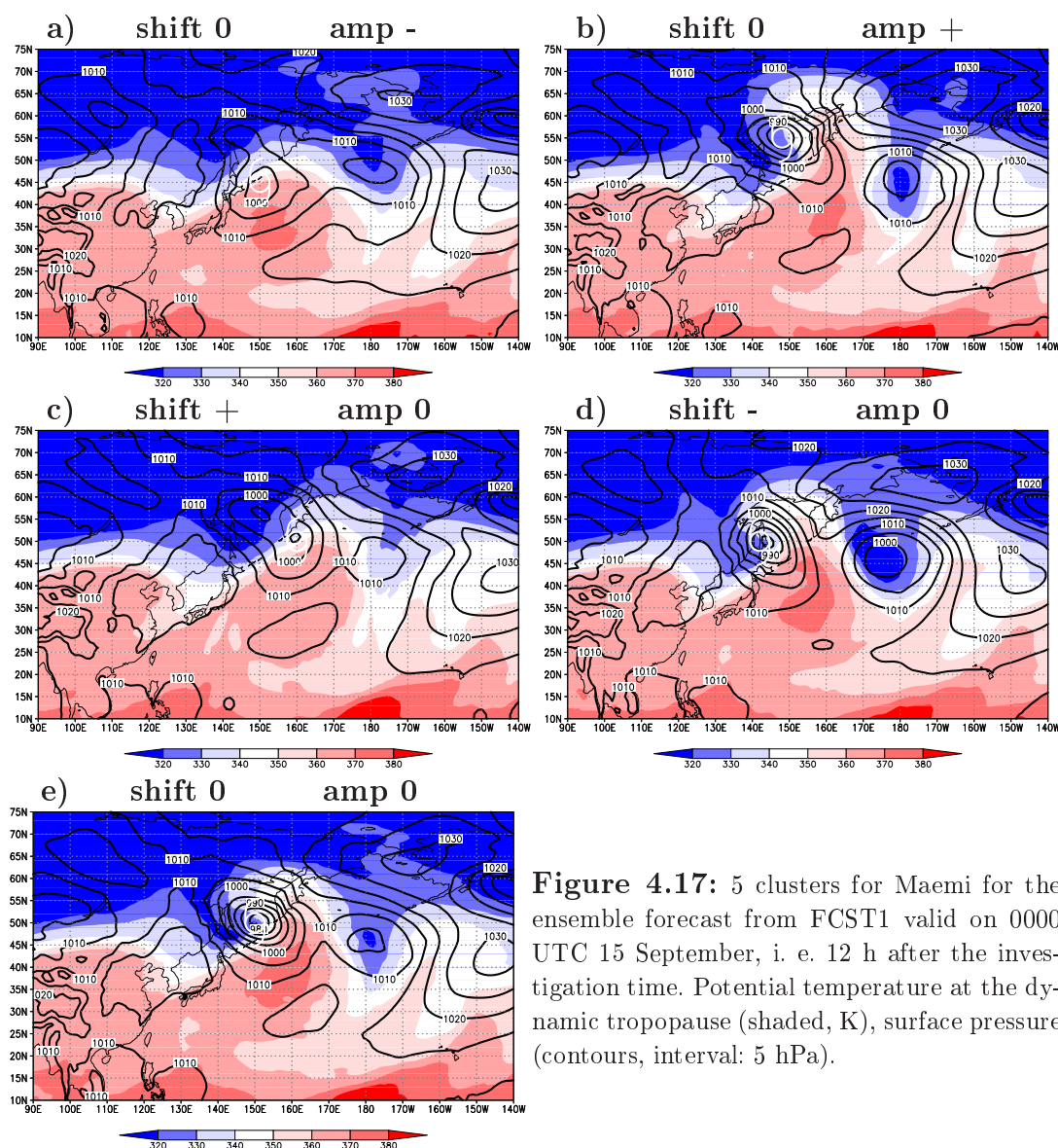


Figure 4.17: 5 clusters for Maemi for the ensemble forecast from FCST1 valid on 0000 UTC 15 September, i. e. 12 h after the investigation time. Potential temperature at the dynamic tropopause (shaded, K), surface pressure (contours, interval: 5 hPa).

low level temperature. The clusters of Maemi are taken exemplary because for Maemi the clusters contributing to the shift pattern do not contribute to the amplitude pattern. In the interest of clarity, the cluster that contributes positively to the shift pattern (Fig. 4.4.2 c) is referred to as „positive shift“ and the cluster that contributes negatively to the shift pattern (Fig. 4.4.2 d) as „negative shift“. Fig. The time development of the temperature at 850 hPa in colors together with the relative vorticity in contours of the two Maemi clusters at this level is shown from 00 UTC 13 September to 00 UTC 15 September (Fig. 4.20).

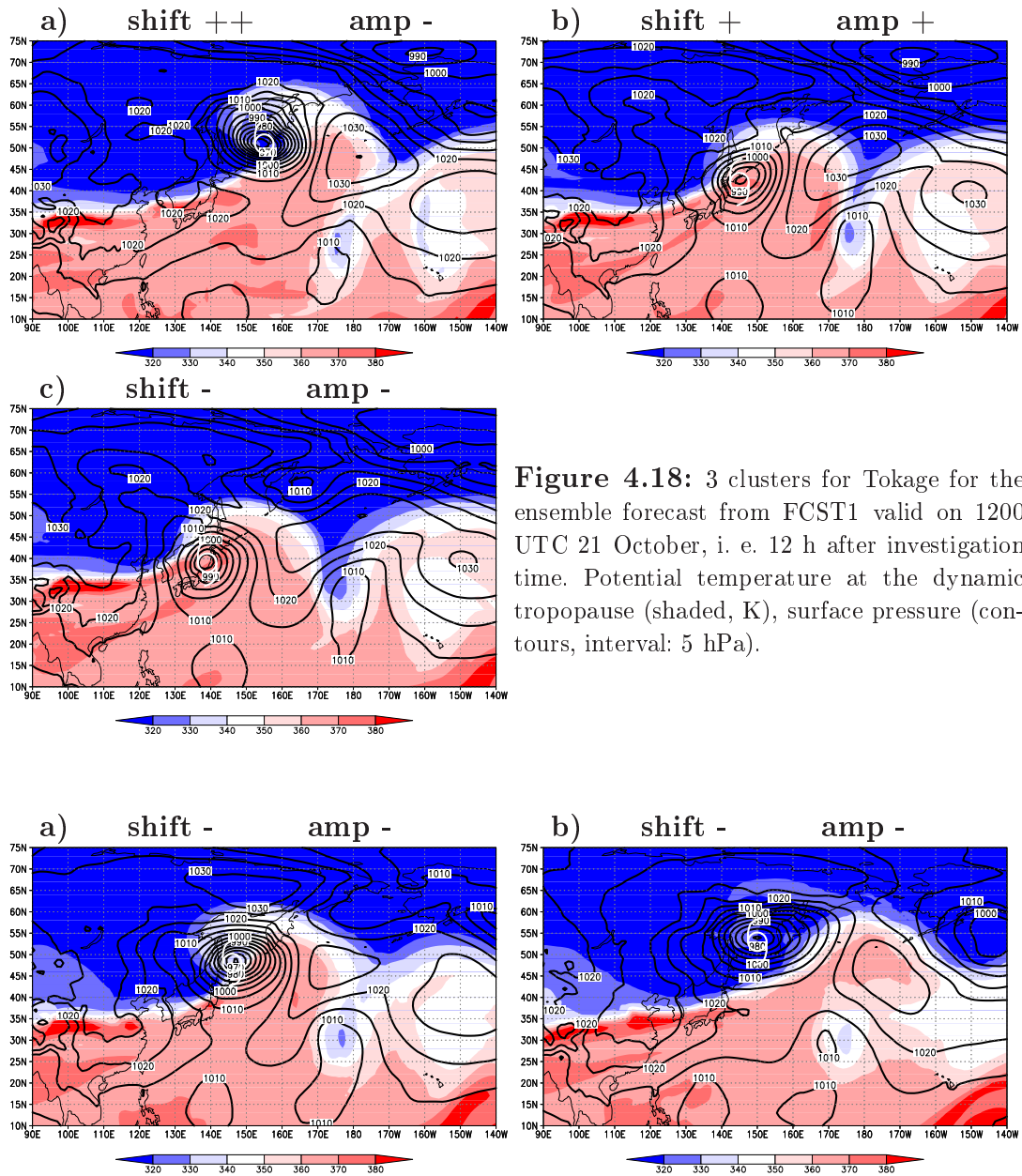


Figure 4.18: 3 clusters for Tokage for the ensemble forecast from FCST1 valid on 1200 UTC 21 October, i. e. 12 h after investigation time. Potential temperature at the dynamic tropopause (shaded, K), surface pressure (contours, interval: 5 hPa).

Figure 4.19: Same cluster as Fig. 4.18 c for a) 1200 UTC 22 October and b) 1200 UTC 23 October.

At 00 UTC 13 September the enhanced midlatitude temperature gradient in negative shift (Fig. 4.20 a) is further away from the ex-TC, seen as a relative vorticity maximum, than in positive shift (Fig. 4.20 b), but it is stronger upstream of Maemi. One day later the temperature gradient has developed to a steep cold front in negative shift (Fig. 4.20 c) which results from the enhanced transport of cold poleward air towards the southeast. The cold front upstream of the TC in positive shift (Fig. 4.20 d), stays comparatively weak.

This results in a more zonal flow pattern which allows a quicker downstream propagation of the ex-TC. While on 13 September (Figs. 4.20 a, b) the positions of Maemi were about the same, on 14 September (Figs. 4.20 c, d) Maemi is clearly further east in positive shift (Figs. 4.20 d). On 15 September the cold front at Maemi's position in negative shift (Fig. 4.20 e) has nearly caught up with the warm front. The negative thickness advection has deepened the baroclinic system (Holton, 1992) and the ET system, which is almost stationary compared with 14 September (Figs. 4.20 c), can re-intensify strongly. In contrast, the cold front in positive shift (Fig. 4.20 f) has weakened and ex-Maemi is far to the east in comparison with negative shift (Fig. 4.20 e).

Positive amplitude pattern

A positive contribution to the amplitude pattern indicates a high amplitude trough-ridge-trough pattern (Figs. 4.16 a, 4.4.2 b, 4.18 b, Figs. 4.21 a, 4.4.2 a, d). In the clusters of the strong events the TCs moved towards the baroclinic zone and appeared to steepen the potential temperature gradient through their outflow. The position of the approaching upper level troughs was favorable for a further steepening leading to cyclogenesis upstream (Hirschberg and Fritsch, 1991). All the strong events contributing positively to the amplitude pattern re-intensified strongly.

The weak events do not seem to play an active role in the ridge building. Nevertheless, the clusters that contribute positively to the amplitude pattern (Figs. 4.21 a, 4.4.2 a, d) show a rather distinct development of a trough-ridge pattern that contains a trough that interacts with the TC and a ridge directly downstream. The ex-TCs interact with the comparatively high potential temperature gradient between the trough and the ridge and undergo ET. One of the Philippe clusters (Fig. 4.4.2 a) shows a weak re-intensification 12 h after the time shown. The other one (Fig. 4.4.2 d) shows a strong re-intensification 36 h after this time. In the Saola cluster that contributes positively to the amplitude pattern, the ex-TC has re-intensified weakly (Fig. 4.21 a). Ex-Saola moves to the west and merges with the large-scale midlatitude system 24 h later.

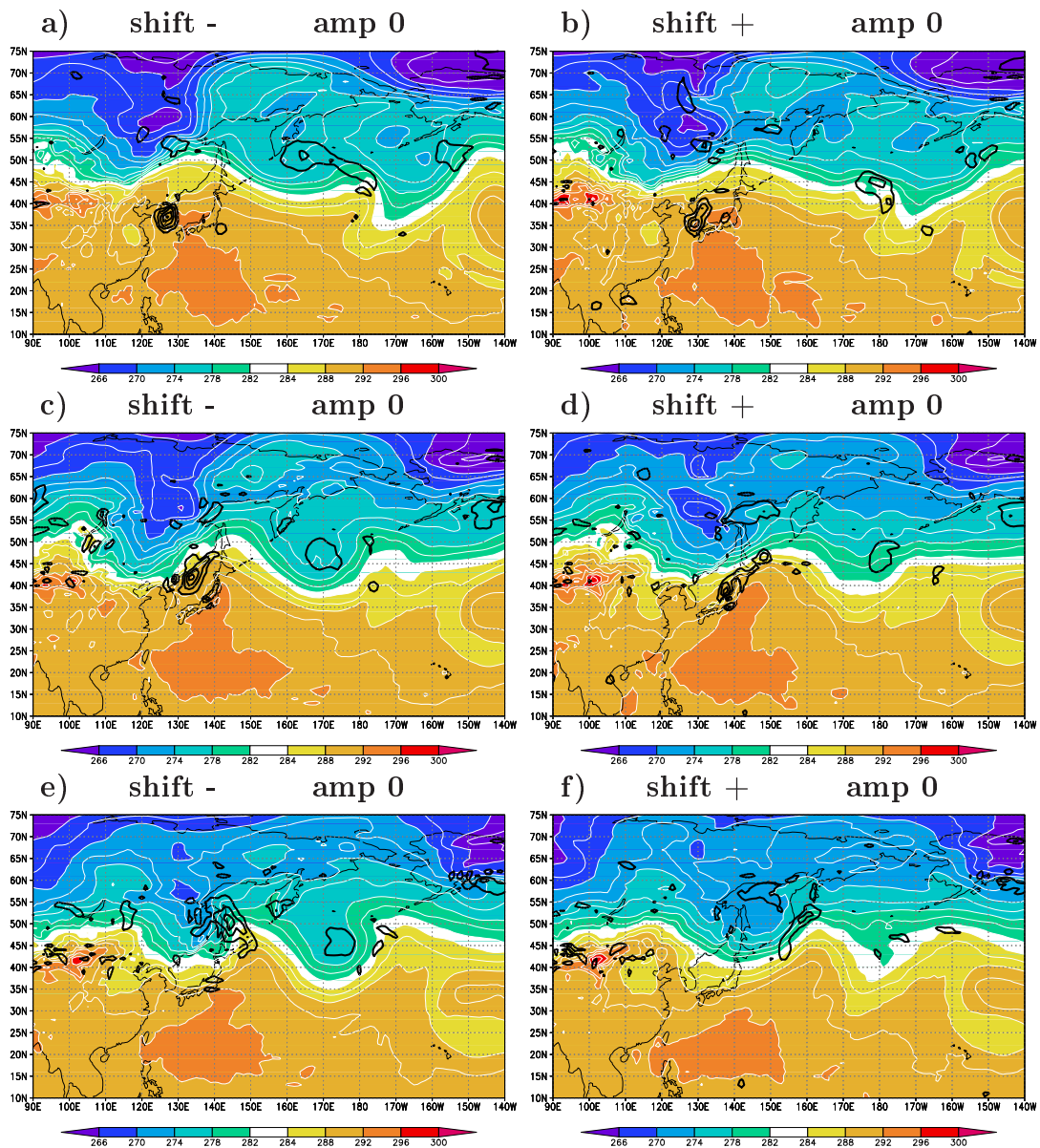


Figure 4.20: Clusters contributing in a negative (left) and positive (right) sense to the shift pattern for Maemi as in Fig. 4.4.2 d and c valid on 00 UTC 13 Sept. (a, b), 14 Sept. (c, d) and 15 Sept. (e, f). Temperature (K, shaded) and relative vorticity (contours, interval: $5 \times 10^{-5} \text{ s}^{-1}$) at 850 hPa.

Negative amplitude pattern

A negative contribution to the amplitude pattern indicates zonal flow (Figs. 4.16 b, 4.4.2 a, d, 4.18 a, c, Figs. 4.21 b, 4.4.2 c, e). This is particularly marked for Fabian, Maemi, Saola and Philippe. In Figs. 4.16 b and 4.4.2 a the ridge is large-scale and shallow and there is no wrap up in the upstream trough. Fabian decayed after completion of its recurvature (3

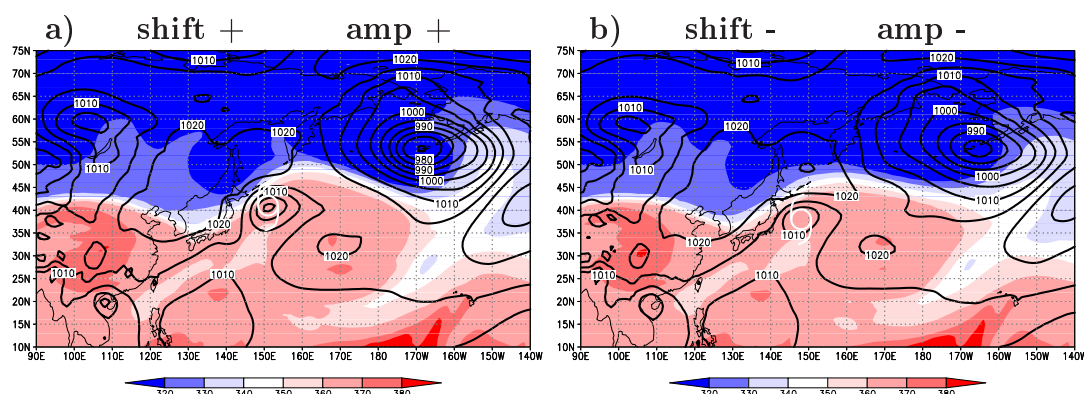


Figure 4.21: 2 clusters for Saola for the ensemble forecast from FCST2 valid on 0000 UTC 27 September, i. e. the investigation time. Potential temperature at the dynamic tropopause (shaded, K), surface pressure (contours, interval: 5 hPa).

days before the time shown in Fig. 4.16 b) without undergoing ET because the upstream trough was too far west and thus not favorable for an interaction. The remnants of Fabian can be seen at about 40° W and 50° N in Fig. 4.16 b. Ex-Maemi's track was influenced by the upstream midlatitude trough that steered it to the east but it did not re-intensify because it was to the east of the potential temperature gradient. These two clusters (Figs. 4.16 b and 4.4.2 a) show no ET or ET without re-intensification. At first glance Figs. 4.18 a and c have different flow patterns than expected for a negative contributor to the amplitude pattern. The ridges are slightly shallower than in 4.18 b but the ET systems undergo deep reintensification. This is primarily due to the high amplitude trough-ridge pattern of the ensemble mean. Also, in the case of Tokage the shift pattern explains a much larger part of the total variability (22.0 %) than the amplitude pattern (10.8 %) (Table 4.2). Therefore the influence of the amplitude pattern on the development of the individual clusters is much weaker.

No upstream trough can be seen in Fig. 4.4.2 c for Philippe and there is only a very weak trough in Fig. 4.4.2 e. The ex-TC either has decayed already (Fig. 4.4.2 c) or a small low pressure system resulting from Philippe moves towards the Bahamas (Fig. 4.4.2 e). The strength of Saola in the midlatitudes is noticeably weaker in Fig. 4.21 b than in Fig. 4.21 a due to its weaker upstream trough and weaker potential temperature gradient between the upstream trough and the ridge. Therefore, Saola merges with the large-scale

midlatitude system downstream 24 h later than in the cluster with positive contribution to the amplitude pattern.

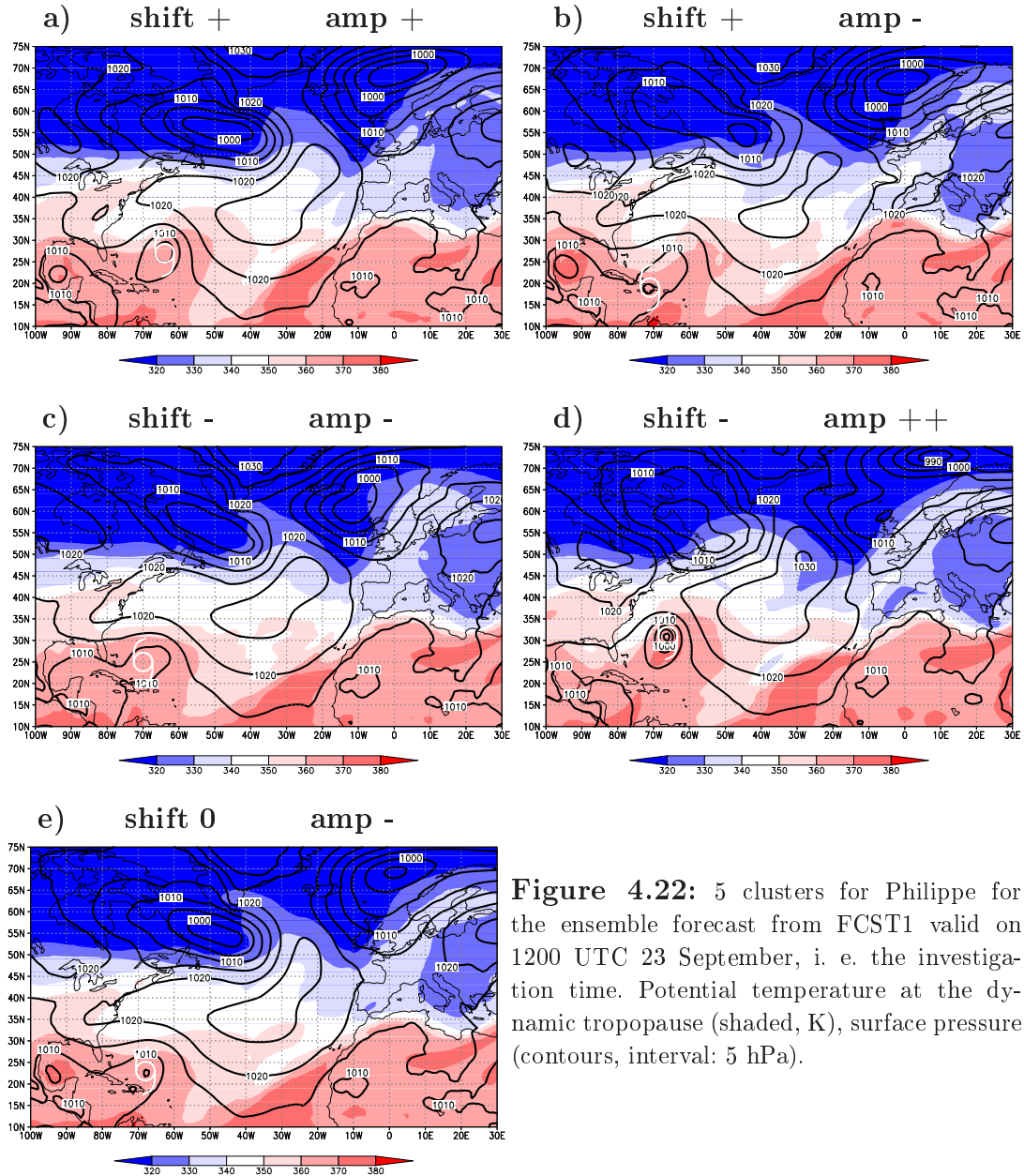


Figure 4.22: 5 clusters for Philippe for the ensemble forecast from FCST1 valid on 1200 UTC 23 September, i. e. the investigation time. Potential temperature at the dynamic tropopause (shaded, K), surface pressure (contours, interval: 5 hPa).

Time development: Amplitude pattern

Analogous to the time development of positive and negative shift, the time development of the ET systems in the clusters which contribute positively and negatively to the ampli-

tude pattern can be investigated examining the low level temperature. Again the clusters of Maemi are chosen because those which contribute to the amplitude pattern do not contribute to the shift pattern. In the interest of clarity, the cluster that contributes positively to the amplitude pattern (Fig. 4.4.2 b) is referred to as „positive amplitude“ and the cluster that contributes negatively to the amplitude pattern (Fig. 4.4.2 a) as „negative amplitude“. As for the shift patterns (Fig. 4.20) the time development of positive and negative amplitude is shown from 00 UTC 13 September to 00 UTC 15 September (Fig. 4.23).

At 00 UTC 13 September the temperature gradient in negative amplitude (Fig. 4.23 a) is further away from Maemi than in all the other clusters at this time (Figs. 4.20 a, b, 4.23 b) indicating a very unfavorable position for Maemi to re-intensify. There is no indication of a beginning southward transport of low temperature air. In contrast, a steep cold front can be seen in positive amplitude quite closely upstream of Maemi at this time already (Fig. 4.23 b). Even though ex-Maemi has moved close to the temperature gradient on day later in negative amplitude (Fig. 4.23 c) still no development of a baroclinic system is indicated. In positive amplitude (Fig. 4.23 d) the cold front is oriented rather meridionally and the advection of cold air deepens the baroclinic system strongly. Hence, ex-Maemi is located in an area of strong baroclinic development and can re-intensify strongly. A second system has developed downstream. On 15 September a weak temperature wave can be seen in negative amplitude (Fig. 4.23 e) with the remnants of Maemi at the rear of the ridge. No development is seen and the ex-TC has decayed in this cluster. In positive amplitude (Fig. 4.23 f) a weakening temperature gradient indicates a starting decay of the ET system. The downstream baroclinic system, however, has intensified. The warm and cold front in this system have nearly occluded.

Outliers

Another noticeable parallel can be found in the clusters for Fabian, Tokage and Philippe. Both of them have one comparatively small cluster (Table 4.2), with a mean that exhibits a markedly different development of the atmospheric flow pattern than the ensemblemean

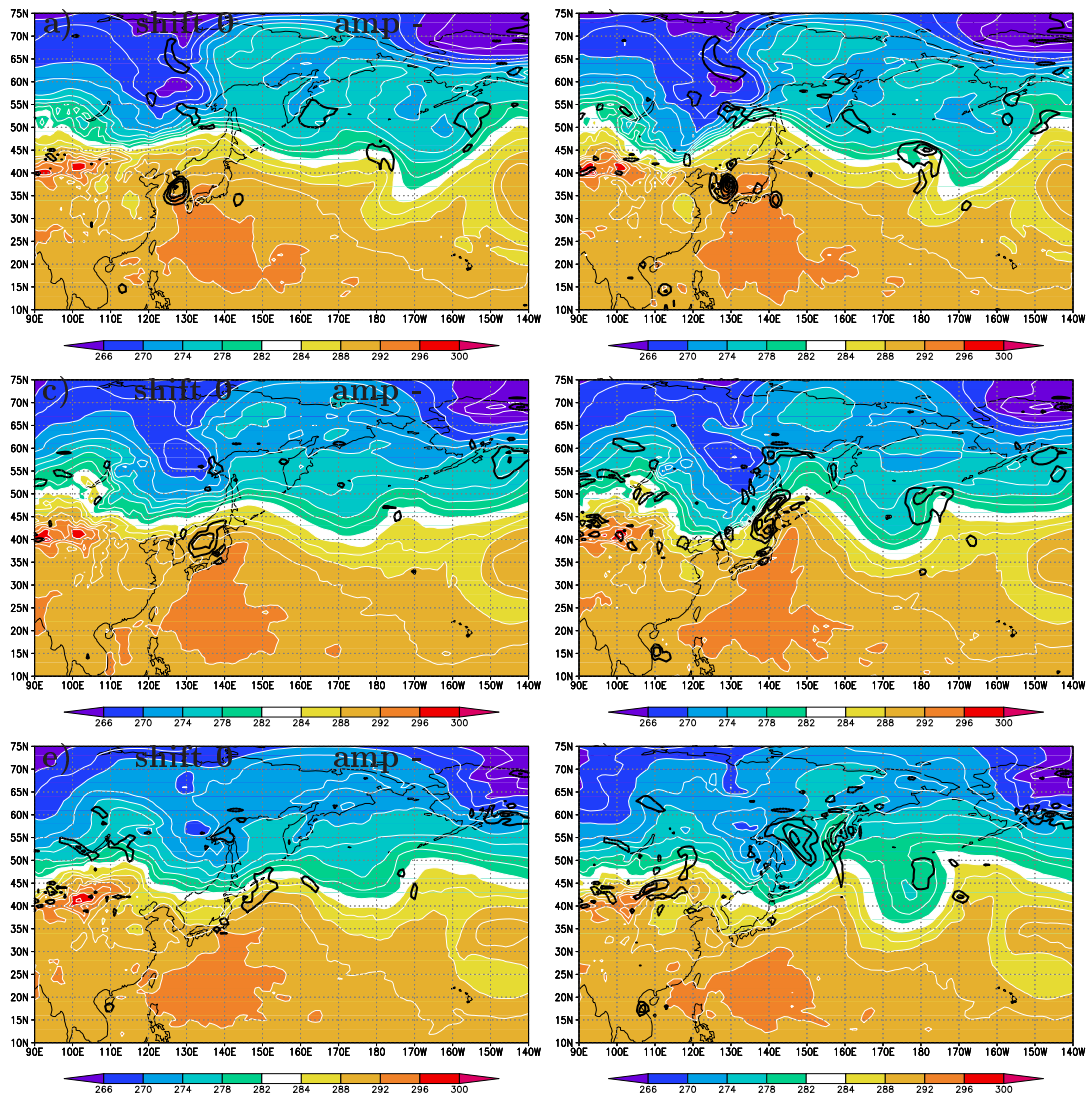


Figure 4.23: As Fig. 4.20 for clusters contributing in a negative (left) and positive (right) sense to the amplitude pattern for Maemi

and the other cluster means (Figs. 4.16 b, 4.18 a). For Maemi such an extreme cluster exists also (Fig. 4.4.2 a), but it is not smaller than the others. The different development in the case of Tokage can be seen also in the strong positive contribution to the shift and in the case of Philippe in the strong positive contribution to the amplitude pattern. In the cases of Fabian and Maemi the extreme clusters show a quite zonal flow, as described above. In the case of Tokage the extreme cluster is the one that shows the fastest development and decay of the ET system. Here the dynamical tropopause is already flattening while in the other Tokage-clusters the ridge is in the process of steepening or reaching its

peak. For Philippe the outlier is the only one that shows a strong re-intensification. Note that the outliers show the highest differences to the analysis.

In each of the cases except for Saola the clusters found in the ensemble forecasts from FCST1 yield quite different possible atmospheric developments that all have comparable probabilities. Although the analysis is within the ensemble spread (section 4.2.1) none of the clusters resemble the analysis for Maemi and Tokage. That does not necessarily mean that no member is similar to the analysis, but that a low probability is assigned to the development that can be seen in the analysis. The ensemble forecast for Fabian yields one cluster (Fig. 4.16 c) that is in reasonable agreement with its analysis. The smaller standard deviation of the ensemble forecast of Fabian compared to the other strong events (section 4.2.1) suggests that the predictability for Fabian in FCST1 is higher than that for Maemi and Tokage. For Philippe the cluster that shows an ET with strong re-intensification (Fig. 4.4.2 d) is most similar to the deterministic forecast (not shown). From the number of members in the Philippe clusters (Table 4.2) it is concluded that the ensemble assigns a very low probability to the deterministic forecast and a distinctly higher probability to the clusters that do not show re-intensification and are therefore more similar to the analysis.

It is remarkable that for FCST2 the outliers do not appear in any of the cases (Table 4.3). Thus they are considered to play a major role in the high standard deviation for FCST1 (section 4.2) that decreases abruptly at the later forecast time. The number of clusters for FCST2 is equal (Tokage) or smaller (Table 4.3) with a noticeable decrease from 5 to 2 clusters for Maemi and Philippe. Furthermore, for all cases the largest or one of the dominant (Tokage) clusters is closest to the analysis in terms of the position of the ET system and of the development of the flow pattern. This indicates that forecasts initiated at times close to or after recurvature are characterized by a higher predictability. The initial conditions excluded the outlying developments that could be seen in the small clusters. Nevertheless, maxima in these standard deviations could still be seen for FCST2 (section 4.2). In the clusters for FCST2 the variability is associated with the tilt and the

amplitude of the trough-ridge-trough pattern. Similar relations between the development in the clusters and their contributions to the shift and amplitude patterns can be drawn for FCST2. It can be said that there is still a distinct variability associated with the ET systems that is not due to uncertainties in the forecast of recurvature.

Through the investigation of the two weak events it could be seen that the ensemble forecast yields valuable additional information to the deterministic forecast in assigning probabilities to it. The analysis method works even for the very weak case of Philippe and for the forecast from FCST2 for Saola. Inherently, the precondition that is necessary for applying the method successfully to analyse an event is that there is a high part of the total variability in the ensemble associated with that event. This was not the case for FCST1 for Saola. To capture the small number of members that do recurve it might be helpful to use a clustering method that takes into account a time period instead of only a single time.

5 Experiments

5.1 Overview over experiments

The complex physical interactions that occur during the structural changes associated with an ET often contribute to difficulties in the forecast of such events. In section 2.3 the problems that can arise in the numerical forecast during an ET event have been explained in detail. The approaches used in the ECMWF EPS to describe uncertainties in the initial conditions and model errors have been highlighted in sections 3.2.1 and 3.2.2 respectively. From the predictability studies of the five ET cases in section 4.2 it was evident that the ensemble reflects the high uncertainties associated with the ET events.

To demonstrate the importance of the decaying TC undergoing ET for the reduction of predictability, it is interesting to which part unstable structures are associated with the TC and to which part with the midlatitude system. Furthermore, it is of interest, if the uncertainty in initial conditions which may impact the predictability in the environment of an ET system is described by the ensemble. The dispersion and downstream propagation of that impact yields a measure of how far the reduction of predictability due to an ET can reach. The description of the behavior of errors that may arise due to uncertainties in parametrized processes in the presence of an ET and their downstream propagation is of further interest. The comparison of the reduction of predictability due to initial uncertainties and uncertainties in the parametrized processes during an ET may give insightful information. Finally, the impact of the EPS resolution on the error representation during an ET is important.

The experiments are designed to give information about the representation of the error growth in the EPS due to the respective causes, initial uncertainty, uncertainty in parameterization and uncertainty due to coarse resolution. Typhoon Tokage was chosen for the experiments because it seemed to have the highest influence on the building of the trough-ridge-trough pattern as explained in section 4.2.1. Before its ET the midlatitude flow upstream of Tokage was zonally oriented. When the TC approached the strong potential temperature gradient on the dynamical tropopause a distinct ridge formed (Fig. 4.2 c). In the experiments new 10 day FCST1 and FCST2 ensemble forecasts were calculated with the ECMWF EPS of Tokage. For the EPS the resolution T255L40 and for the SV calculation the resolution T42L40 was used as mentioned in section 3.3.

The representation of initial condition uncertainties can be investigated by the aid of experiments concerning the perturbations targeted on the optimization region of Tokage (Fig. 3.3). To be consistent with the model cycle used for the experiments the SVs were recalculated. The targeted singular vectors describe the structure of the highest instabilities and are used to simulate small errors in the initial conditions in the optimization region into which Tokage is forecast by the EPS to propagate as explained in section 3.2.1. By investigating their structure and location, information is obtained about which part of the instabilities and the resulting error growth can be attributed to the ex-TC and which part to the upstream trough.

In the first experiment a new model run without the perturbations targeted on Tokage was performed and compared to a new model run with the same configuration but with targeted perturbations. The difference yields a measure of the influence of the targeted perturbations on the description of uncertainties in the ensemble. To reduce the difference between the two runs solely to that associated with the targeted perturbations the stochastic physics was switched off. The SVs that are used to initialize the ensemble were recalculated as well. For the runs without the additional perturbations targeted on Tokage the script in PrepIFS that is responsible for the linear combination of SVs (Eq. 3.27) is modified such that the additional SVs for Tokage's optimization region (Fig. 3.3: green box) do not contribute to the initial perturbations \mathbf{x}_j . In other words, the optimization

region for Tokage is switched off. Hence, the two model runs differ only in the additional SVs targeted on Tokage.

In the second experiment the representation of uncertainties due to parametrized processes is investigated by examining the impact of the stochastic physics. The EPS was ran without targeted perturbations around Tokage but with stochastic physics. These runs were compared to equivalent runs but without stochastic physics. To switch off the stochastic physics the perturbed parametrized tendencies from the calculation of the ensemble members \mathbf{e}_j in Eq. (3.32) are just excluded. That is done by setting $r_j(\lambda, \phi, t)$ equal to 1 in Eq. (3.33).

In the third experiment the behavior of the ensemble during the presence of an ET with the high resolution configuration (T399L62), implemented in February 2006, was tested. The experiment is performed with and without the targeted perturbations on Tokage but without stochastic physics. In addition to the representation and downstream propagation of uncertainties due to ET our attention was turned to the ability of the high resolution ensemble forecast to capture the weakening of our ET case Tokage after its landfall on Japan. The experiments are listed in Tables 5.1 and 5.2 together with some results which will be discussed later.

One focus of our analysis of these experiments lies with the correct representation of the track and intensity spread of the TC ensemble forecast. An important criteria is the representation of the analysis by the ensemble members, i. e. if the analyzed track is contained in the ensemble ((Puri et al., 2001)) and if some members are closed to the analysis. Moreover, the question is posed as to whether the ensemble spread is “realistic”, i. e. if it is large enough to describe the uncertainties but does not overestimate the uncertainties. This question is addressed through comparing the root-mean-squared error (RMSE) of the ensemble mean with the root-mean-squared difference (RMSD), a measure of ensemble spread that determines the average distance of all the ensemble members to the control forecast. Alternatively, the standard deviation can be used as measure of spread within the ensemble members (Buizza et al., 2004) as shown in the case studies (4.2). If the RMSE is equal to the RMSD or the STD the spread is assumed to be represented

correctly. If the RMSE is lower or higher then the spread is over- or underestimated.

The dispersion and downstream propagation of the influences due to the targeted perturbations and the stochastic physics is examined by calculating the spread differences in the geopotential at 200 and 500 hPa between the runs in the respective experiments. The rapidity and mechanisms of the downstream propagation of the respective errors were explored. In principle the experiments can be seen as a simulation of the impact that an ET can have on the predictability in its vicinity and downstream.

Finally, the spread and diversity of the synoptic patterns shown by the individual ensemble members in the experiments, can be investigated by grouping them analogous to the case studies. For this purpose the analysis method described in section 4.3 is applied.

5.2 Structure of the singular vectors

The additional perturbations targeted on TCs are calculated using only initial SVs. In section 5.3 differences between the experiments with and without additional perturbations will be shown.

The structure of the singular vectors, with which the targeted perturbations on Tokage in the experiments are initialized, has been investigated to gain insight into where the regions of high uncertainty in association with Tokage's ET are and what is the structure of the SVs that grow most strongly in 48 hours and lead to the differences between the experiments with and without targeted perturbations. Our interest was focused on the role that Typhoon Tokage and its interaction with the midlatitudes plays in the growth of disturbances compared to the preexisting baroclinicity in the midlatitude flow. For this purpose the properties of the singular vectors targeted on Tokage that were recalculated for the experiments were compared with some properties found in previous investigations of extratropical singular vectors.

The previous studies found that the perturbation energy for the extratropical SVs at initial time is typically largest in lower tropospheric levels and propagates upwards during

Table 5.1: As Table 4.2 for the T255L40 resolution experiments with the ECMWF ensemble prediction system IFS.

	Clusters	Members	Shift pattern	Contrib.	Amplitude pattern	Contrib.	ET	Fig.
Resolution T255L40								
		11		+		-	0	5.17 a
Pert/		12		-		-	3	5.17 c
Nosto	4	8	11.2 %	+	18.4 %	+	3	5.16 a
		14		o		+	3	5.16 b
		14		+		o	3	5.16 c
Nopert/	3	18	20.7 %	-	10.1 %	+	3	5.16 d
Nosto		11		-		-	2	5.17 b
		9		+		-	2	/
Pert/		13		-		-	3	/
Sto	4	10	9.9 %	+	19.2 %	+	3	/
		11		-		+	3	/
		19		o		+	3	5.25 a
Nopert/	3	14	19.3 %	-	9.6 %	-	3	5.25 b
Sto		9		+		-	3	5.25 c

optimization (Hartmann et al., 1995; Buizza and Palmer, 1995; Reynolds et al., 2001; Peng and Reynolds, 2006). Badger and Hoskins (2000) use a simple 2 dimensional (x,z) model to describe structures that lead to strong transient growth of perturbations which exceeds the growth of the normal modes during a short time period. They use the Eady basic state which implies a constant vertical shear ($\bar{u} = \Lambda z + u_0$). They explain the strong growth conceptually through the mechanism of PV “unshielding”.

In Fig. 5.1 (a) a region of positive potential vorticity is located in the center of the model domain. The shielding by the negative PV on top and beneath it inhibits the flow

Table 5.2: As Table 4.2 for the T255L62 (Lowres) and T399L62 (Highres) resolution experiments with the ECMWF ensemble prediction system IFS.

	Clusters	Members	Shift pattern	Contrib.	Amplitude pattern	Contrib.	ET	Fig.
Resolution T255L62 (Lowres) and T399L62 (Highres)								
Pert/		12		+		+	3	5.30 b
Nosto/	4	8	22.4 %	-	9.4 %	+	3	5.31 b
Lowres		12		-		-	2	/
		14		+		-	3	5.30 d
Nopert/		20		+		+	3	/
Nosto/	3	8	17.9 %	+	7.7 %	-	2	/
Lowres		14		-		-	3	/
Pert/		12		+		+	3	5.30 a
Nosto/	4	13	20.7 %	+	9.7 %	-	2	5.30 c
Highres		9		-		+	3	5.31 a
		9		-		-	2	5.31 b
Nopert/		17		o		+	3	/
Nosto/	3	10	17.7 %	+	7.7 %	-	2	/
Highres		14		-		-	3	/

associated with the PV anomaly from creating a thermal anomaly at the boundaries. In this constellation no growth is possible. However, as soon as the basic zonal flow advects the PV anomalies the negative anomalies are displaced eastward and westward respectively, relative to the positive PV anomaly (Fig. 5.1 b) which is therefore no longer shielded from the upper and lower boundary. Interaction with the boundaries takes place and thermal anomalies are induced through temperature advection by the meridional wind. These thermal anomalies can be regarded as PV anomalies in turn. The difference between day 0 and 0.5 (Fig. 5.1 c) shows that the meridional wind is tilted westward inducing positive PV anomalies that become phase-locked. The wind and pressure fields

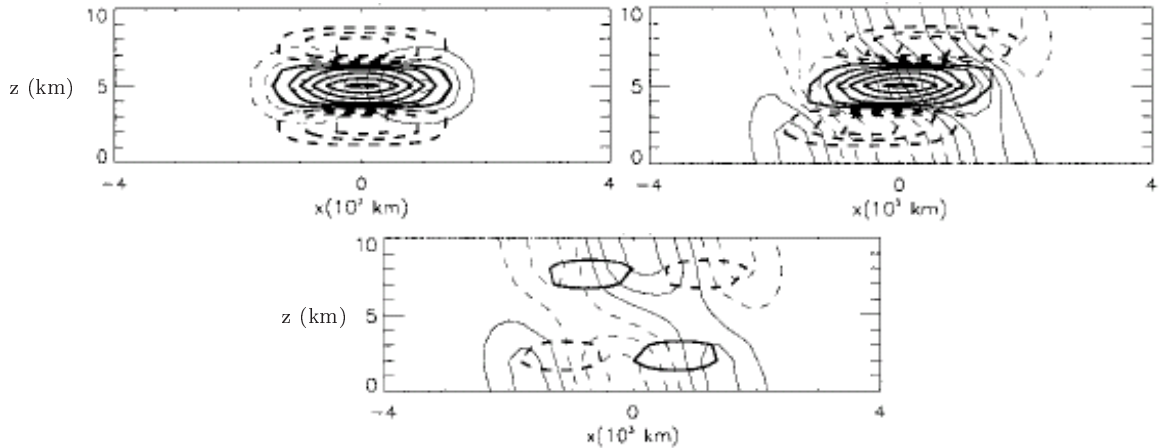


Figure 5.1: Perturbation potential vorticity (thick contours, interval : 10^{-5} s^{-1}) and meridional wind (thin contours, interval: 0.25 ms^{-1}) for a perturbation with 4000 km horizontal and 8 km vertical scale. Dashed lines are negative and solid lines positive values. (a) day 0, (b) day 0.5. (c) difference between (b) and (a).

are tilted against the shear and disturbances can propagate up- and downwards. As soon as the positive PV anomaly is unshielded, i. e. between day 0 (Fig. 5.1 a) and day 0.5 (Fig. 5.1 b), rapid growth occurs during a short period followed by a period of slower sustained growth due to the coupling of interior PV anomalies and boundary thermal anomalies (Reynolds et al., 2001). For shorter horizontal scales the negative PV anomalies would be displaced more rapidly and a stronger and faster growth would follow. This agrees with the statement of Hartmann et al. (1995) that the energy growth is faster for initial perturbations of sub-synoptic scale waves than for larger scale initial disturbances (Hartmann et al., 1995). The former adopt quickly structures of synoptic scale waves in an optimization interval of 1.5 to 3 days.

Reynolds et al. (2001) found leading SVs, i. e. strongest perturbation growth, below upper level PV features which they explained by the initial unshielding and upward propagation of energy. Singular vectors produced with the total energy norm show an upscale energy cascade from subsynoptic to synoptic scales during their optimization time (Buizza and Palmer, 1995; Hoskins et al., 2000). Because of this feature the total energy is a suitable norm to describe error growth in the modeling of the atmosphere because initial errors are in general subgrid scale and influence the forecast of the synoptic scale flow.

The strong growth of small scale initial disturbances is reminiscent of the “butterfly effect” (Lorenz, 1963b) in the sense that small scales can influence large scales. Singular vectors localized in wave packets tilted strongly against the shear (Badger and Hoskins, 2000; Hoskins et al., 2000) become tilted towards the vertical by shear and grow. This is visualized using a schematic of the superposition of two waves which have the same wavelength and amplitude but opposite tilts. The lines designate the phase lines. It can be seen that initially the waves have the same tilt. After some time the tilt of the upshear tilted wave decreases and the tilt of the downshear tilted wave increases. The upshear tilted waves extract energy from the mean flow in the process of untilting them (Reynolds et al., 2001).

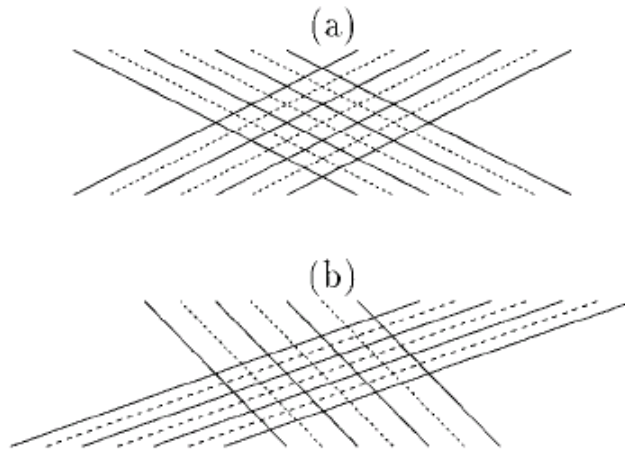


Figure 5.2: Schematic of two plane waves in potential vorticity with equal and opposite tilt at initial time (a) and some time later (b). The shear of the flow has changed the tilt of the lines representing equal phase.

It can be said that extratropical SVs evolve from baroclinic to more barotropic structures. Initially they are tilted strongly with height consistent with upward propagation of wave activity as the group velocity is directed into the jet (Buizza and Palmer, 1995). After their optimization time they are quite vertically oriented (Buizza and Palmer, 1995; Hartmann et al., 1995). This structural change can be transferred to barotropically developing waves as well. Here, the SVs are associated with waves tilted against the barotropic shear (Buizza and Palmer, 1995).

Several authors who investigated the influence of moist physics on SVs in detail (Ehrendorfer et al., 1999; Barkmeijer et al., 2001; Coutinho et al., 2004; Hoskins and Coutinho, 2005) found that they grow stronger and faster than dry SVs. Moist SVs have a shorter optimization interval, i. e. only 24 h. Coutinho et al. (2004) stated that the large-scale condensation is the dominant process in the full physics package. The rapid grow of moist SVs is due to large-scale latent heat release. Further studies have been conducted where an additional term for the specific humidity was included in the total energy norm (Ehrendorfer et al., 1999; Barkmeijer et al., 2001). However, during the optimization interval all energy is transformed in the specific humidity component, i. e. the total energy is dominated by the specific humidity. Hence, the moist total energy norm is not useful when interested in a general probability forecast also for other components such as temperature and wind (Barkmeijer et al., 2001). Consequently, the dry total energy norm without inclusion of the specific humidity term is used operationally at the ECMWF. However, the tropical SVs are calculated from the tangent linear model including the full physics package (moist SVs).

5.2.1 Spatial structure

The horizontal and vertical structure of the leading SV (SV1) with regard to barotropic and baroclinic tilt is investigated firstly by only using the temperature component of the initial SV1 (Fig. 5.3) for 1200 UTC 16 and 1200 UTC 18 October at 200 hPa, 500 hPa and 850 hPa. The temperature component has been chosen as it is proportional to the potential energy which is in general higher for extratropical initial SVs than the kinetic energy (Hoskins and Coutinho, 2005; Peng and Reynolds, 2006). SV1 is used because it dominates the characteristics of the first 5 SVs integrated vertically over the atmosphere (Eq. 3.21) as will be confirmed in section 5.2.4. On both dates the singular value for SV1 is about twice as high as the singular value for SV2.

The behavior of the leading SV parts that are located around Tokage, i. e. in the subtropics, are quite different to the parts in the midlatitudes confirming the findings of Barkmeijer et al. (2001). Therefore, they are described separately in the following and are

referred to as tropical parts and midlatitude parts respectively. At 200 hPa on 16 October (Fig. 5.3 a) the tropical parts of SV1 cover a rather large area around Tokage. On 18 October (Fig. 5.3 b) only two small rings of the tropical SV that have weak amplitude are located east and west of Tokage in the upper troposphere. The amplitude of the tropical parts on 16 October is higher at 200 hPa than at 500 hPa (Fig. 5.3 c) while on 18 October only structures of weak amplitude can be found south east of the TC at 500 hPa (Fig. 5.3 d). At 850 hPa few SV1 structures are around the outermost closed isobar around Tokage on 16 October (Fig. 5.3 e) and on 18 October (Fig. 5.3 f). No distinct barotropic tilt of the tropical SV structures can be seen at none of the two times. The only shear in the vicinity of Tokage is due to its cyclonic winds. Consequently, other mechanisms than untilting of upshear tilted waves are responsible for the growth of disturbance energy. The location of the tropical parts of the SVs in the upper troposphere may be explained by the statement of Reynolds et al. (2001) that the steering level is higher up in less baroclinic environments like the tropics or summer time midlatitudes. Initial SVs tend to be located at the steering level as will be illustrated in detail below.

The midlatitude parts of the leading SV structures cover the largest area and have the highest amplitude at 500 hPa on 16 October (Fig. 5.3 c) compared to 200 and 850 hPa. At 200 hPa (Fig. 5.3 a) only quite small amplitude structures can be found in the trough and the ridge upstream of Tokage. The largest parts of SV1 on 500 hPa can be found in the midlatitudes directly north of Tokage at the axis of the thermal trough (Fig. 5.3 c). A trough in the geopotential is situated east of these low temperatures indicating a growing baroclinic system because cold polar air is advected into the trough acting to further deepen it. Reynolds et al. (2001) stated that SVs occur in regions of large mid-level thermal gradients which corresponds to the location of the parts of SV1 directly north of Tokage. In a trough upstream in the midlatitudes some structures are seen as well. Even though the trough is not the one with which Tokage will interact, the SV indicates that this region of high baroclinicity has a distinct influence on the TC development and motion. The upstream parts of the midlatitude SV at 500 hPa seem to indicate instability and possible error growth connected with the recurvature and the interaction of Tokage with the midlatitudes. Deviations in the initial conditions may result in a constellation

that is favorable for a phase-locking of Tokage with the upstream trough which could result in a strong re-intensification or at least acceleration towards the east many hours before the analyzed ET. This would imply large forecast errors. Moreover, a rather strong temperature gradient can be found directly at the location of the upstream part of SV1 indicating a deepening of the small trough seen in the geopotential through advection of cold air. On 18 October at 500 hPa (Fig. 5.3 d) the amplitudes and the area covered by SV1 upstream in the midlatitudes is much larger than on 16 October. They could be associated with the upstream midlatitude flow influencing the TC motion. This is not surprising as the analyzed recurvature is on 0000 UTC 19 October. Hence, small uncertainties in place and time of the interaction of the TC with the region of high baroclinic instability in the midlatitudes, indicated by the strong temperature gradient, will cause large error growth. While on 16 October almost no structures in the midlatitude SV can be seen at 850 hPa on 18 October rather high amplitude structures are located in the midlatitudes (Fig. 5.3 f). Moreover the signal in the subtropical high, which is located at about 130 - 160° E and 25 - 45° N, is much more distinct giving evidence of its influence on the TC motion through blocking it from moving northwards so that the storm moved along the periphery of the high.

The midlatitude SV structures are tilted against the shear implying energy growth of the disturbances (Badger and Hoskins, 2000). This barotropic tilt is much stronger on 18 October than on 16 October at 500 hPa. This might be associated with the stronger horizontal shear denoted by the stronger geopotential gradient indicating higher barotropic instability.

The structures both on October 16 and 18 are small scale, i. e. they cover less than 15°, as reported for initial extratropical SVs in Buizza and Palmer (1995). This is an inherent property of SVs calculated with the total energy norm. SVs of small scales are favorable for strong growth, as explained in the previous section. The midlatitude SV structures and almost all of the SV structures on 18 October have extratropical SV properties. There is almost no amplitude at 200 hPa and the highest amplitudes are around 500 hPa, the typical steering level for the midlatitudes, at initial time. As mentioned in the

previous section the perturbation energy of these disturbances is expected to propagate upwards during optimization time. The scales of SV1 are similar both on 16 October at 200 and 500 hPa and on 18 October at 500 and 850 hPa. Nevertheless, on 16 October some meridionally larger scales can be found at 200 hPa west of Tokage as well, indicating slower growth of SV1 during the optimization time in that region west of Tokage.

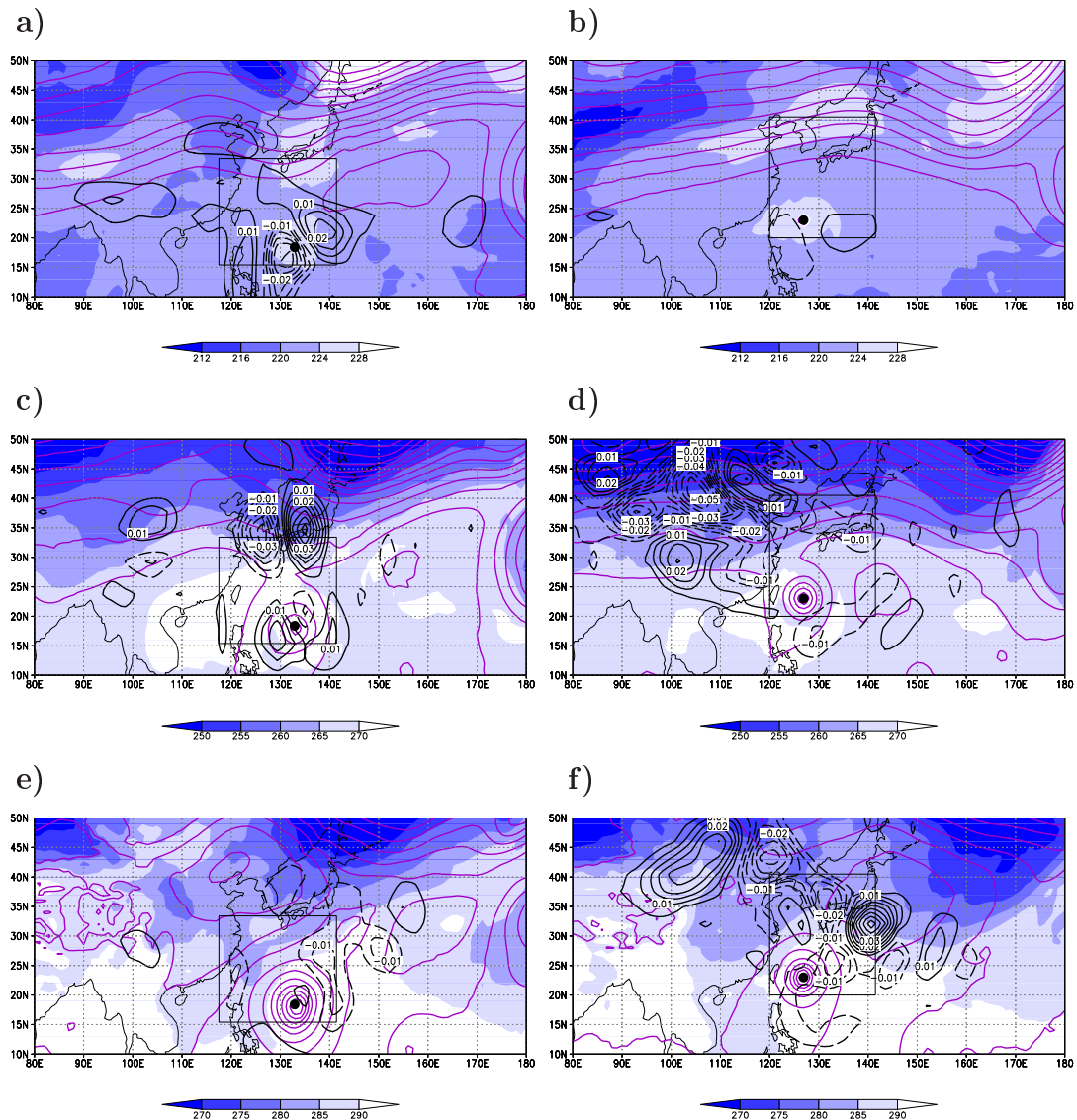


Figure 5.3: Temperature component (K, black) of the leading initial SV targeted on Tokage. Top row: model level 10 (about 200 hPa); middle row: model level 20 (about 500 hPa) and bottom row: model level 29 (about 850 hPa) on 12 UTC 16 October 2004 (left) and 12 UTC 18 October 2004 (right). Geopotential height of control forecast at initialization time on the respective level (m, purple). Tokage is marked by a black dot. Optimization regions for Tokage are shown as black boxes.

The parts of SV1 that are located around the TC at 200 hPa on 16 October may be associated with the TC outflow. The anticyclonic circulation of the outflow and the small values of the Coriolis parameter in the tropics might be the causes that the absolute vorticity is negative in large parts northeast of Tokage (Fig. 5.4 a) so that the criteria for inertial instability (Holton, 1992) is fulfilled. Furthermore, the criteria for barotropic instability is satisfied in the region of the tropical parts of SV1 at 200 hPa as well because the gradient of the absolute vorticity changes sign south and east of the TC close to the TC center. SV1 indicates the instability in this region. Similar results have been found by Barkmeijer et al. (2001). The response of the SVs to these instability criteria can be seen clearly at 500 and 850 hPa also. At all three levels the vorticity is strongest in the center of the storm and decreases away from it until it reaches a local minima or changes sign. These locations of the tropical SVs confirm the findings in the composites of Peng and Reynolds (2006) who investigated 85 tropical cyclone cases which they divided into groups of straight moving, recurving and irregular-motion cases. They found the SVs approximately at 500 km away from the storm center in regions where the vorticity gradient changed sign. This distance would correspond to the 500 hPa level (Fig. 5.4 b) in our case. Here the SVs are located rather to the southeast and southwest of the storm (Fig. 5.4 b). Peng and Reynolds (2006) justified their results by the Rayleigh condition of instability ($\frac{\partial \bar{q}}{\partial y}$ changes sign, where q is the potential vorticity) and the inertial instability of the vortex near the outer part of the storm. Hence, it can be concluded that in the vicinity of the storm the instability mechanisms are different than in the midlatitudes leading to a different appearance of tropical SVs than extratropical SVs.

Reynolds et al. (2001) found in their composites of 38 cases that initial SV maxima lie beneath distinct upper-level PV features. They attribute this to the fastest growth occurring through PV unshielding and upward propagation of energy from mid to upper levels.

It is obvious that the midlatitude SV parts at 500 hPa (Fig. 5.4 b) lie directly beneath the upper-level trough north of Tokage (Fig. 5.4 a). At 200 hPa (Fig. 5.4 a) the midlatitude SV parts can be found in regions of relatively weak vorticity gradients. Palmer et al. (1998)

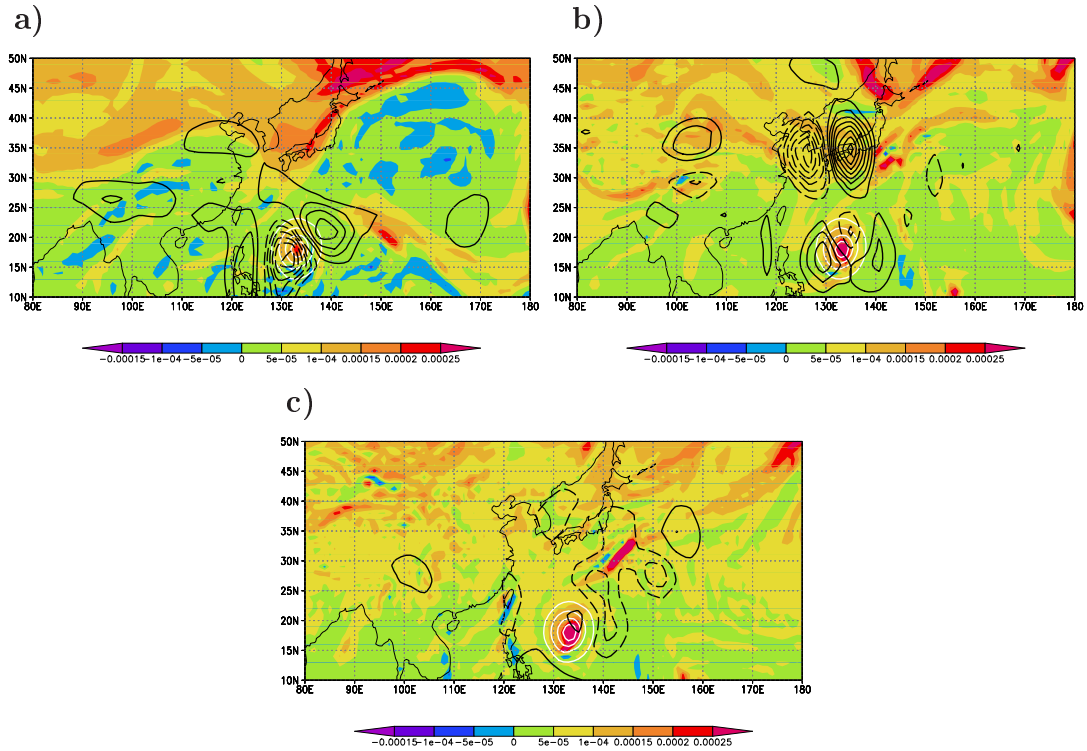


Figure 5.4: Absolute vorticity (shaded, s^{-1}), temperature component of initial SV1 (black contours, K) and mean sea level pressure ≤ 1000 hPa (white contours, m) at 200 hPa (a), 500 hPa (b) and 850 hPa (c) on 16 October 12 UTC. Tokage is marked by a black dot.

explained that the SV growth is associated with the propagation of planetary Rossby waves from weak PV gradient regions to strong PV gradient regions.

5.2.2 Distribution of energy

Interesting differences in the behavior of tropical and extratropical SVs can be found by comparing the available potential energy and the kinetic energy. The APE for the different levels has been calculated from the first term of Eq. 3.21 by setting u and v equal to zero and the kinetic energy by setting T equal to zero. The respective components of SVs 1 to 5 have been weighted by their singular values and summed.

As seen in the comparison of the temperature component for 16 and 18 October (Fig. 5.3) the APE of the tropical part of the SVs has highest values at 200 hPa on 16 (Fig. 5.5 a). On 18 October a much smaller-scale structure of SV APE is seen in the region

of the TC. At this level, both on 16 and 18 October the SVs are merely associated with the typhoon. At 500 hPa they still cover a distinct area around the TC on 16 October (Fig. 5.5 c) while on 18 October (Fig. 5.5 d) the tropical part is as small as at 200 hPa. However, at this level both on 16 and 18 October the amplitude and area covered by SV APE in the midlatitudes is much larger than in the subtropics.

In the midlatitudes SV APE is only seen at 500 hPa on 16 October. On 18 October the midlatitude parts of the SVs are in the mid (Fig. 5.5 d) and lower (Fig. 5.5 f) troposphere. As found by Peng and Reynolds (2006) for the straight moving cases, tropical SV APE can mainly be seen to the rear of the TC, i. e. in the southeast, of Tokage's on both dates with the exception of 850 hPa on 16. Investigating the wind vectors it is obvious that the SV APE is in regions where the flow is directed towards Tokage. At 500 hPa on 16 and 18 October, for example, the midlatitude SVs are only seen in the upstream part of the trough directly north of Tokage corresponding with the region of the flow moving towards the storm. In contrast, the storm evolution in this case does not seem to be sensitive to the eastern part of the trough where the wind blows away from the storm. Similarly, on 18 October at 850 hPa the extratropical SVs are also upstream of the TC and the tropical SVs are mainly in the southwestern part of the subtropical high where the wind blows towards the storm. Peng and Reynolds (2006) state that the inward flow is associated with the steering flow of a TC and that, hence, the maximum uncertainty affecting its motion, i. e. the leading SV, is linked to it. The fact that leading SVs are found in the upper troposphere around the TC indicates that the flow in the upper regions may have a steering influence on Tokage as well, whereas the steering level for extratropical systems is rather in the midtroposphere. The distinct difference between the two days is that while on 16 October both on 200 and 500 hPa distinct parts of the SVs are associated with the storm the SVs are connected almost only to midlatitude features like the upstream trough at 500 hPa (Fig. 5.5 d) and the subtropical high (Fig. 5.5 f) on 18 October.

The kinetic energy of the SVs is found in the mid- and lower troposphere only. In Fig. 5.6 the 500 (top) and 850 hPa (bottom) levels are shown for 16 (left) and 18 (right) October. The vertical energy distribution corresponds to that in Peng and Reynolds (2006) where

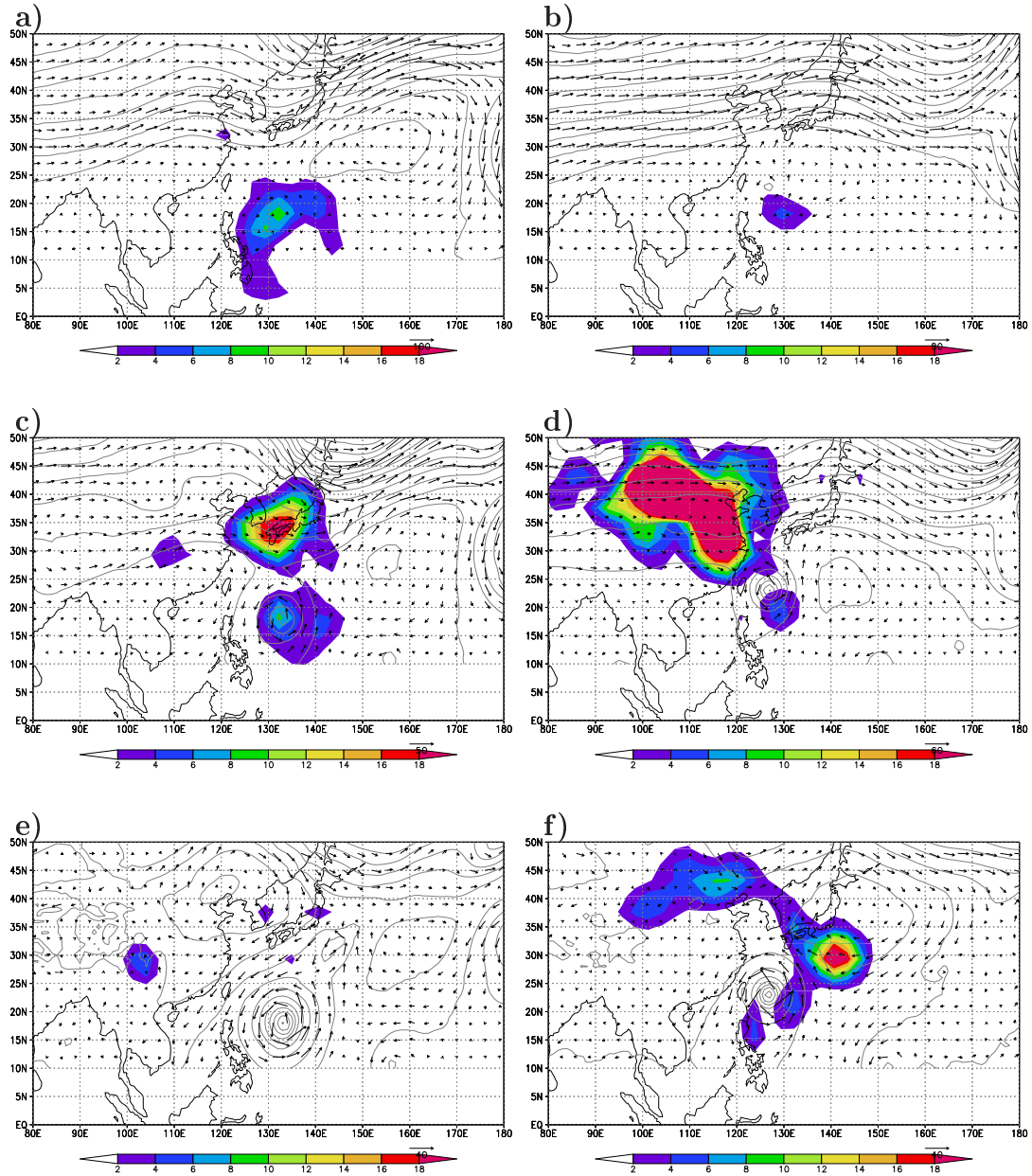


Figure 5.5: APE (shaded, 10^{-3}Jkg^{-1}) of the leading initial SV targeted on Tokage. Top row: model level 10 (about 200 hPa); middle row: model level 20 (about 500 hPa) and bottom row: model level 29 (about 850 hPa) on 12 UTC 16 October 2004 (left) and 12 UTC 18 October 2004 (right). Horizontal wind (black arrows, ms^{-1}) and geopotential height of control forecast at initialization time on the respective level (m, gray contours).

the potential energy for the leading initial SVs was located at about 500 hPa and the kinetic energy at about 700 hPa. In contrast to the APE of the SVs, at lower levels a large part of the kinetic energy of the SVs is located around the TC. Peng and Reynolds (2006) point out that the dominance of the kinetic energy around the TC is typical and represents a significant difference between extratropical and tropical cyclone SVs. As for the APE of the SVs, the kinetic energy lies mainly in regions in which the flow is directed towards the storm but is more equally distributed in an annulus around the TC, especially on 16 October at 500 hPa (Fig. 5.6 a). On 16 October the kinetic energy is located almost only around the TC while on 18 October the behavior is more like that of midlatitude SVs in that the energy can be found in regions of high baroclinicity in the midlatitudes.

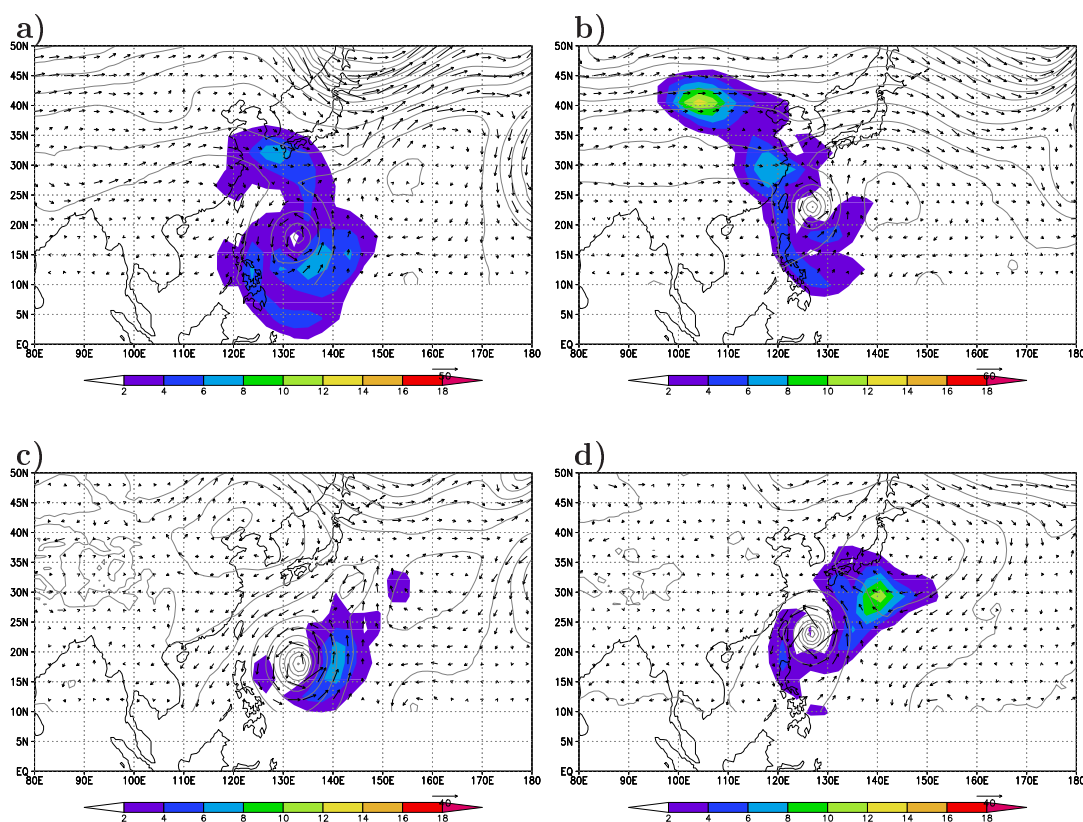


Figure 5.6: As Fig. 5.5 for kinetic energy (shaded, 10^{-3}Jkg^{-1}). Only 500 hPa (a, b) and 850 hPa (c, d) are shown.

5.2.3 Temporal evolution

The time evolution of the vertical structure of the leading SV can be examined by investigating the five initialization times in 24 hour intervals from 14 October 12 UTC, i. e. 108 hours before recurvature, to 18 October 12 UTC, i. e. 12 hours before ET. It is of interest to examine how the SV structure changes from a tropical to a more extratropical one as the TC approaches recurvature. To investigate the tropical parts separately from the midlatitude parts initial SV1 has been divided into two latitude bands. The tropical parts of SV1 have been averaged between a latitudinal band between 0° - 20° N from 14 to 16 October and between 5° - 25° N on 17 and 18 October (black contours). The midlatitude parts of SV1 have been averaged between 20° - 40° N from 14 to 16 October and between 25° - 45° N on 17 and 18 October.

In the previous section it was found that the highest amplitude of the leading singular vector is at rather high levels at times well before recurvature (Fig. 5.3, left). Figs. 5.7 a, b and c illustrate that from 1200 UTC 14 October (Fig. 5.3 a) structures in the vicinity of the TC are located to a large part above model level 20 and extend as far as model level 10. Their amplitudes and heights in the tropics around the TC grow between the initialization times 14 to 16 October (Figs. 5.7 a - c). In the midlatitudes north of Tokage and upstream, i. e. polewards from 20° N, the SV1 structures can be found around model level 20 (500 hPa) and below from 14 (Fig. 5.7 a) to 18 October (Fig. 5.7 e). On 17 and 18 October the baroclinic upshear tilt of the extratropical parts is much stronger than at earlier times before recurvature and SV1 extends further downwards. On 18 October (Fig. 5.7 e) structures can be seen at model level 35 which is well inside the boundary layer.

The high levels of the parts around Tokage suggest sensitivity to small errors associated with the impinging of the outflow on the jet. At latitudes around Tokage SV1 shows a tilt to the east with height, especially on 16 October. Examination of the high level wind and the meridional temperature distribution demonstrated that from 300 hPa on, an easterly shear direction predominates, connected with a weak increase in temperature from 0° to 15° (not shown). Thus, SV1 is tilted against the vertical shear, suggesting growth in this

region as well. At the initialization time 1200 UTC 17 October the SV1 parts around the TC are less and decrease in amplitude while more parts can be found in the midlatitudes especially upstream (Fig. 5.7 d). On 1200 UTC 18 October almost no structures at high levels (level 15) are left and the largest part of SV1 is concentrated in the midlatitudes between level 20 and 25, i. e. about 500 to 700 hPa, (Fig. 5.7 e) resembling more to the behavior of extratropical SVs as mentioned in the previous section. At this time the SV structure indicates sensitivity and error growth associated with the recurvature of Tokage.

In this section and the previous it has been demonstrated that the leading SV shows different features, for example an eastward tilting structure and high amplitudes at higher levels, at the initialization time longer before recurvature when it is mainly in the tropics. Possible error growth is rather associated with instabilities through the TC and a possible interaction with the midlatitudes. At the later initialization times the largest possible error growth seem to be connected to the baroclinic zone and to the recurvature of Tokage.

5.2.4 Comparison with Eady-Index

The simplest model for baroclinic instability is the Eady model (Eady, 1949). An f-plane is assumed. A constant negative meridional temperature gradient is in thermal wind balance with a linear increase in wind speed with height. The system has fixed upper and lower boundaries. The ‘‘Eady index’’ is based on the growth rate of the most unstable normal mode in the Eady model:

$$\sigma_E = 0.31 \frac{f}{N} \frac{d\mathbf{u}}{dz} \quad (5.1)$$

with the Coriolis parameter f , the Brunt-Väisälä frequency N and the uniform vertical wind shear $\frac{d\mathbf{u}}{dz}$ in thermal wind balance with a N-S temperature gradient. It is used to illustrate regions of baroclinic instability in atmospheric flow, i. e. where baroclinic growth can occur (Hoskins and Valdes, 1990). For the calculation of the Eady index in pressure coordinates the mean temperature T_M and pressure p_M as well as the potential temperature gradient and the vertical shear have been calculated between 200 and 850 hPa from the ECMWF analyses.

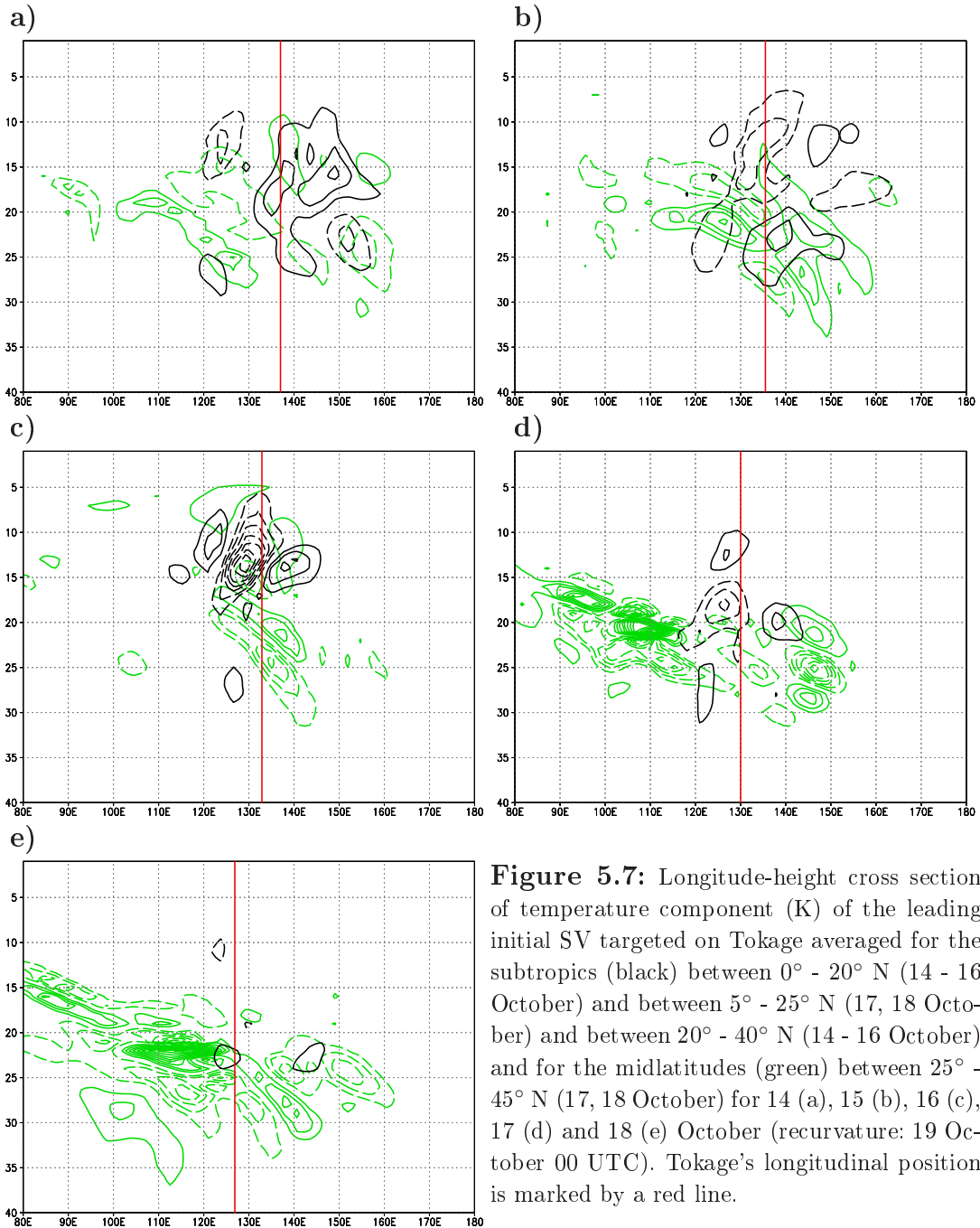


Figure 5.7: Longitude-height cross section of temperature component (K) of the leading initial SV targeted on Tokage averaged for the subtropics (black) between $0^\circ - 20^\circ$ N (14 - 16 October) and between $5^\circ - 25^\circ$ N (17, 18 October) and between $20^\circ - 40^\circ$ N (14 - 16 October) and for the midlatitudes (green) between $25^\circ - 45^\circ$ N (17, 18 October) for 14 (a), 15 (b), 16 (c), 17 (d) and 18 (e) October (recurvature: 19 October 00 UTC). Tokage's longitudinal position is marked by a red line.

It would be expected that SVs are situated in regions of strong vertical wind shear which is necessary for PV unshielding as explained above. The Eady index yields an appropriate means to determine to which extent the SVs react on baroclinic instability and which part can be attributed to instability mechanisms like inertial instability and barotropic instability associated with the TC. In Fig. 5.8 the Eady index is shown from 14 - 18 October together with the sum of total dry energy (Eq. 3.21) of the 5 SVs targeted on Tokage weighted with their respective singular values integrated over 1000 - 200 hPa ($\sum_{i=1}^5 \int (\text{total energy } SV_i) dp$) and the geopotential height on 200 hPa.

Local maxima of baroclinic growth rate can be found in the jet a fact that is implied by the highest vertical shear. It is obvious that from 14 to 16 October (Figs. 5.8 a, b, c) the total energy of SV1 - SV5 is mainly distributed around Tokage indicating that uncertainties in its environment through inertial or barotropic instability have much more influence on Tokage's development than the baroclinic instability in the midlatitudes. The parts in the midlatitudes are just upstream of the maxima of the Eady index as found in the statistics of Buizza and Palmer (1995). Perturbations in this unstable region can influence the TC motion as they are designed to grow optimally in the region around Tokage in the two following days. On 17 and 18 October (Figs. 5.8 d, e) the highest amplitudes of the SVs in the midlatitudes are connected to the relatively high Eady index indicating that the growing instabilities are driven by baroclinic energy conversion. On 17 October a local maxima of the SVs is still seen around Tokage while on 18 October the SVs are almost only confined to the midlatitudes. Rather distinct maxima in the total energy can be seen downstream of Tokage as well. They are almost completely determined by the low level temperature component (Fig. 5.3 f) and the logarithm of the mean sea level pressure in Eq. (3.21) and can be explained through the influence of the subtropical high pressure system that influences Tokage's motion.

The structure of the total energy from SV1 - 5 confirms the behavior explained in previous sections that well before recurvature the SVs are rather associated with instabilities (inertial, barotropic) due to the properties of the tropical cyclone. The parts in the midlatitudes are associated with baroclinic instability indicated by the Eady index and with

the influence of the upstream trough on the TC motion, i. e. recurvature. As the time of recurvature approaches the main part of the structures is associated with baroclinic instability in the midlatitudes. As the structures of the sum of the integrated total energy over SV1 - 5 is similar to just the temperature component of SV1, it is demonstrated that the temperature component of the leading SV shown in sections 5.2.1 and 5.2.3 yields a lot of information about the regions of largest possible error growth in our case and that the available potential energy plays a larger role for initial SVs than the kinetic energy.

5.3 Influence of targeted perturbations

In this section the impact of including the additional SVs targeted on Tokage in the calculation of the initial perturbations is examined. Ensemble runs with and without the additional initial SVs are investigated using the measures of spread described in section 5.1. In the following the runs with the additional initial perturbations targeted on Tokage will be referred to as “Pert” and the runs without the additional initial perturbations as “Nopert”. The perturbation of parametrized tendencies during the model run through stochastic physics was switched off.

5.3.1 Effect on tracks

In Fig. 5.9 the ensemble track forecast for Tokage from FCST1 based on the central mean sea level pressure is shown for Pert (Fig. 5.9 a) and Nopert (Fig. 5.9 b). For comparison the analysis (black line with circles), the deterministic forecast (black line with triangles) and the best track (black line with crosses) is presented.

The best track is a subjective representation of a tropical cyclone’s location and intensity over its lifetime evaluated by operational forecasters. Best track positions and intensities are based on a post-storm assessment of all available data (NHC, 2006). Hence, the best track can be seen as the best estimate of the track that can be obtained.

A distinct difference between the two runs can be seen around the recurvature time

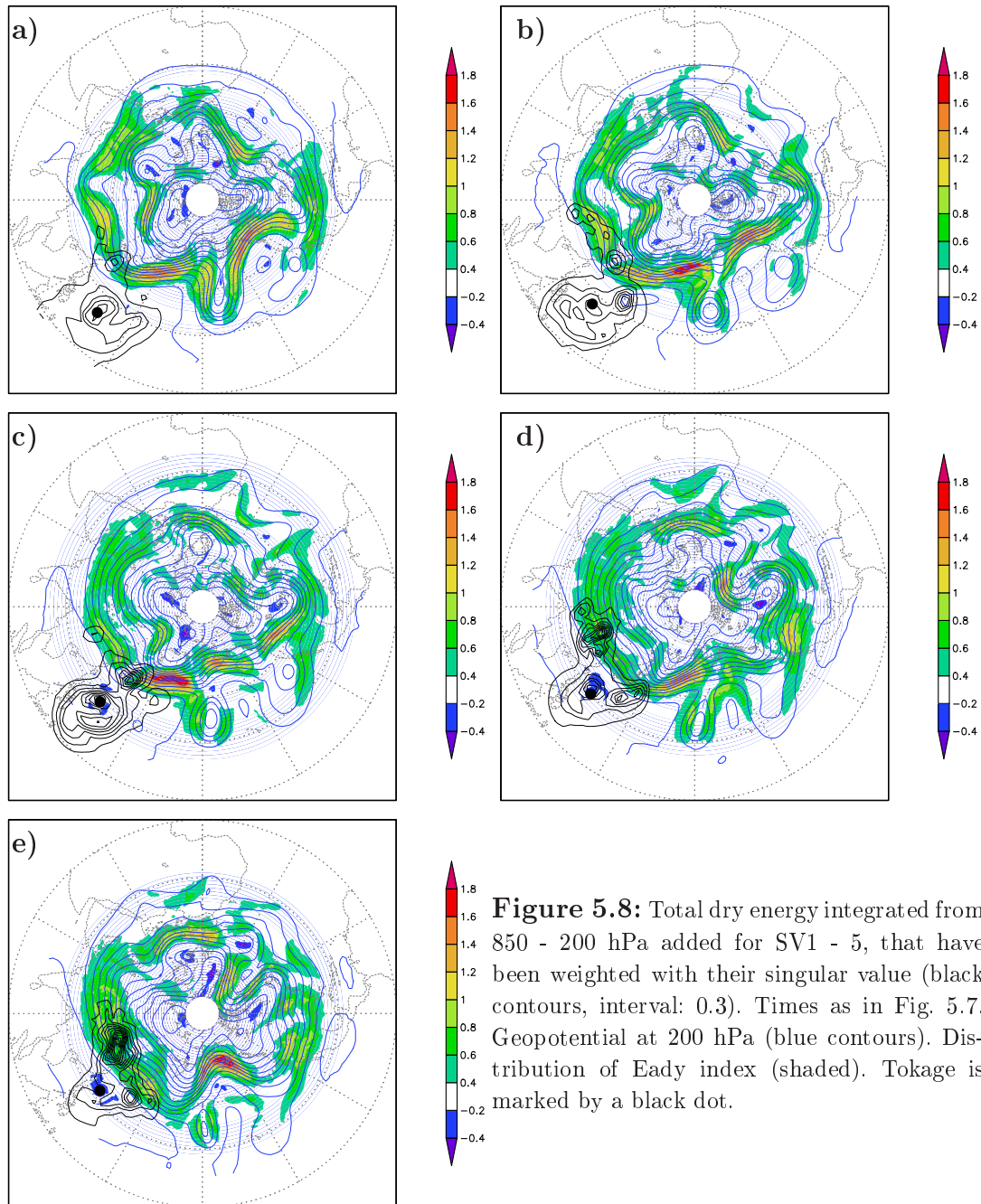


Figure 5.8: Total dry energy integrated from 850 - 200 hPa added for SV1 - 5, that have been weighted with their singular value (black contours, interval: 0.3). Times as in Fig. 5.7. Geopotential at 200 hPa (blue contours). Distribution of Eady index (shaded). Tokage is marked by a black dot.

(60 h after initialization). In Pert (Fig. 5.9 a) the locations of the ensemble members extend over more than 500 km and both the analysis, corresponding well to the best track at this time, and the deterministic forecast lie close to the edge of but fall within the ensemble tracks. In the case of Nopert (Fig. 5.9 b) the deterministic forecast lies at the edge of the ensemble tracks and the analysis even outside for 48 h and 60 h forecast lead time. The spatial separation of the ensemble members has decreased to about 200 km. As the analysis lies outside of the ensemble members the smaller spread in Nopert around the recurvature cannot be attributed to higher predictability. Thus, the uncertainty is underrepresented here.

Close to ET time (the line of analysis and best track are dashed after ET-time) in Nopert (Fig. 5.9 b) the analysis and the best track are in the vicinity of the three southernmost ensemble members and apart from the main group that follows the deterministic forecast. After ET they lie in the gap between the southerly and the main group of the ensemble members such that no member overlaps with the analysis or with the best track. In Pert (Fig. 5.9 a) several members overlap with analysis and best track around ET-time and a few more members can be found south of analysis and best track. No clear gap can be seen in Pert. Thus, the coverage of the area around the analysis by the ensemble members is better than in Nopert.

As the distribution of the positions of Tokage forecast by the ensemble for one individual time cannot be recognized well in the track plots because several tracks cover each other the positions are shown at the analyzed ET time only (bottom right corner of Figs. 5.9 a, b). The analysis, the best track and the deterministic forecast are only shown until ET time. In Pert a larger number of possible ET positions are shown. In more members the storm moves more slowly than in the analysis and thus is situated over southern Japan at ET time. More members than in Nopert are distributed around the analysis and best track. In Nopert a big part of the forecast positions of Tokage are constrained around a region north of the analysis and the best track and hence a quite high probability is assigned to erroneous position forecasts. Even though in Pert a lot of the forecasts, especially those showing the slow TC motion, are far away from the truth, the broad

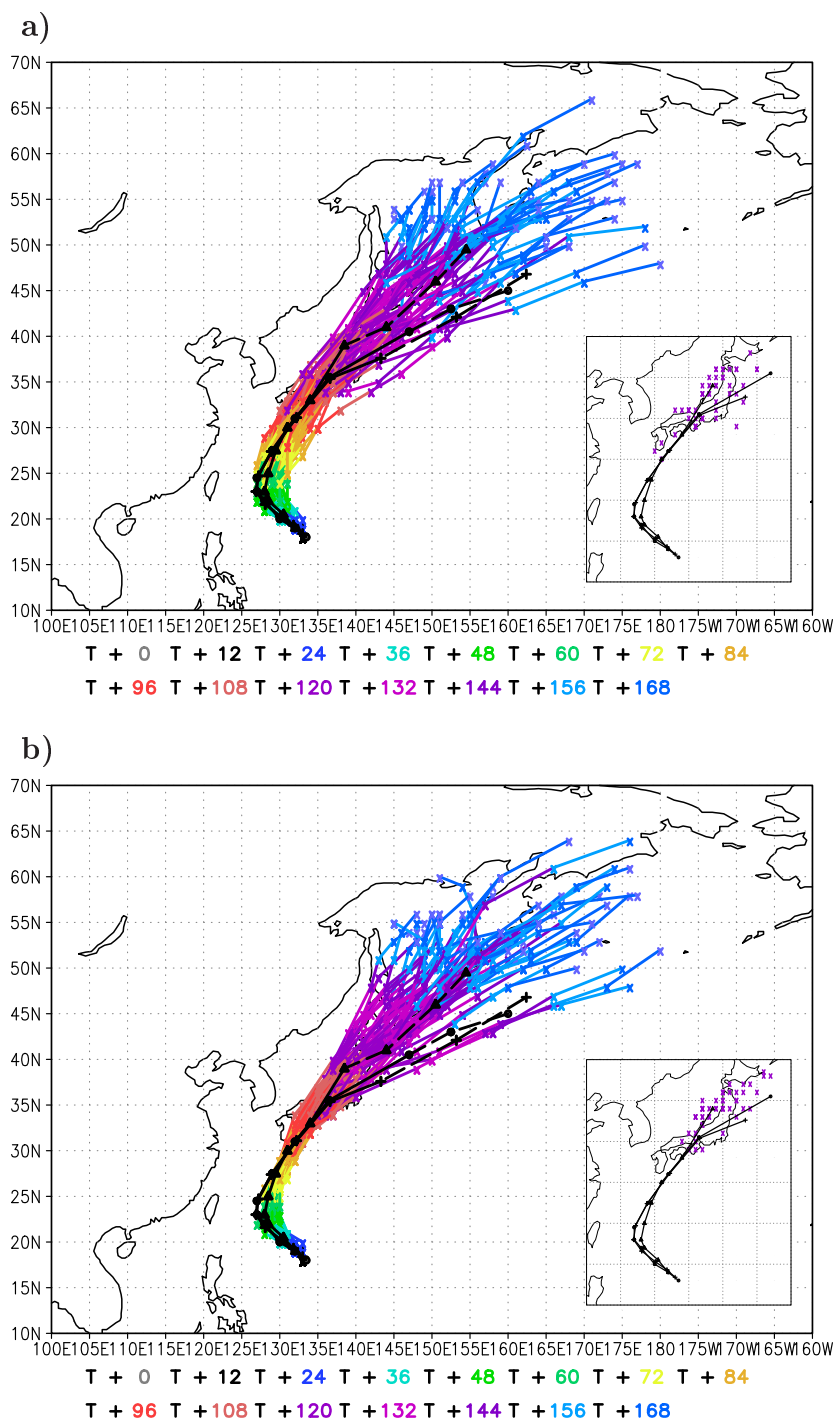


Figure 5.9: Tracks for Tokage based on location of minimum sea level pressure for the runs with (a) and without (b) targeted perturbations on the TC. ECMWF analysis (black line with circles), best track (black line with crosses), deterministic forecast (black line with triangles) and ensemble forecast (colors) from FCST1 for 7 days. Analysis dashed after ET. Right lower corner: Positions of the ensemble members at ET time (purple x), analysis, best track and deterministic forecast only shown until ET time.

distribution of probable positions indicates that the forecast is uncertain. The analyzed position of Tokage is reflected neither in Pert nor in Nopert but in Pert more members show the TC around the position that is assumed to be real, i. e. the position shown by the best track.

It is seen that the SVs targeted on Tokage have an influence on the track spread. Through their rather large scales they perturb the broad structures and the environment around the TC that are resolved sufficiently by the global model for it to have some skill in forecasting TC tracks.

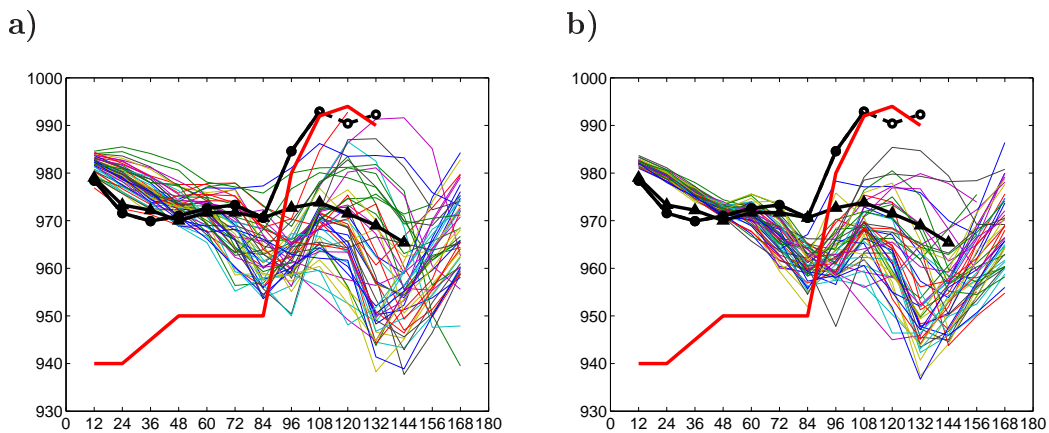


Figure 5.10: Analysis (black line with circles), best track (red line), deterministic forecast (black line with triangles) and ensemble forecast (colors) of the central mean sea level pressure of Tokage from FCST1 for the runs with (a) and without (b) targeted perturbations on the TC.

The ensemble forecast of Pert and Nopert is further examined with regard to its capability to represent the central mean sea level pressure (Fig. 5.10). The resolution of the operational model that has been used to calculate the deterministic forecast is twice as high as that of the ensemble. Therefore the ensemble is expected to show much weaker central pressure values than the deterministic forecast for Tokage in the stage when it is still a tropical cyclone. Moreover, it is not surprising that the best track central pressure lies far from the analysis since global models like the IFS do not have adequate resolution to represent the inner cores of tropical cyclones accurately. However, both analysis and best track show a steep increase of central mean sea level pressure from 20 October 00 UTC to 20 October 12 UTC. Between these two times Tokage made landfall and weak-

ened considerably. From 20 October 12 UTC analysis and best track lie close together in terms of central mean sea level pressure. Shortly after initialization time the spread of central pressure in Nopert (Fig. 5.10 b) is much smaller than in Pert (Fig. 5.10 a) where a notable spread can be seen already at short forecast times.

Both in Pert and Nopert most of the ensemble members show a weakening around 84 - 108 h and re-intensification around 120 - 144 h forecast lead time but of different magnitude. During recurvature (48 h - 72 h) the spread is larger in Pert. In particular, the weak pressures around 980 hPa are not shown in Nopert. For the track forecast the analysis lies outside of the ensemble members in Nopert shortly after recurvature at 84 h while in Pert there are several members that are weaker than the analysis or overlap with it. Some members show a weakening about 12 to 24 hours later than the analysis but only two of them reach the high pressure values seen in the analysis and in the best track. However, the reason for the weakening of these members does not lie in the landfall but in an unfavorable position, i. e. they lie too far south of the TC relative to the midlatitude trough. Only one member of Pert (purple) shows the weakening after landfall corresponding to the analysis of Tokage with a delay of about 24 h. It reaches the pressure value of the analysis after 132 hours forecast time and re-intensifies strongly after a further 24 hours.

Several of the members in Pert and Nopert that show deeper pressure values weaken slightly after landfall as well, but their central pressures remain too deep and the systems subsequently re-intensify strongly. Most of the members in Nopert show even lower pressures than the deterministic forecast. A lot of members show a weakening in Nopert with subsequent re-intensification but the weakest value is about 980 hPa while in the analysis Tokage has weakened to about 990 hPa.

These results can be related to the findings of Puri et al. (2001) who showed that the use of SVs in the tropics leads to an overall weakening of the cyclone in the sense that the ensemble mean forecast has higher pressure than the control ensemble forecast in their two Pacific and Atlantic cases. Nevertheless, all but one of the Pert ensemble runs fail to reflect the weakening of Tokage after landfall sufficiently.

5.3.2 Effect on the amount of spread

The spread in the ensemble forecast from 16 October 2004 12 UTC in terms of the RMSD has been compared to the average RMSE between the ensemble members and the analysis in Pert and Nopert runs to get information about where the spread is represented correctly or where it is under- or even overestimated. In Fig. 5.11 the difference between the RMSE and the RMSD at 200 hPa for the geopotential height is shown. The uncertainty is optimally represented in the ensemble if the RMSD is equal to the RMSE. The areas in that the difference between RMSE and RMSD is between -10 and 10 m (Fig. 5.11), are designated as areas in which the spread is well represented. For better comparison the sizes of the areas of well represented spread in Nopert are visualized in the plot for Pert by black lines (Fig. 5.11 a).

It can be seen that between 19 October 00 UTC in some regions and 21 October 00 UTC in others the dark colored areas with negative values begin to grow markedly. Here the RMSE becomes higher than the spread. These time periods are approximately consistent with the results of Buizza et al. (2004) who found that the three major operational ensemble prediction systems ECMWF, the National Centers for Environmental Prediction (NCEP) and the Meteorological Service of Canada (MSC) exhibit a lack of spread after about 5 days forecast lead time. However, in Pert (Fig. 5.11 a) two plumes in which the spread is well represented can be found downstream of the ET of Tokage expanding from about 150° E to 180° and from 170° W to about 160° W at 21 October 00 UTC and stretching downstream with forecast time. In contrast, the plume located directly downstream of the ET event in Nopert is narrower and the spread is well represented only from 21 October 12 UTC (Fig. 5.11 b).

The first plume directly downstream of Tokage is associated with the representation of the trough downstream of Tokage. If the analysis lies at the edge of the ensemble the RMSE is higher than if it lies close to the ensemble mean. Analogous, if the control forecast lies at the edge of the ensemble the RMSD is higher than if it lies close to the ensemble mean. Hence, if the control forecast lies close to the mean and the analysis at the edge, in other words, if the whole ensemble lies farther from the analysis, the spread is

underrepresented. This is the case in Nopert in the trough downstream of Tokage at ET time as found examining spaghetti plots (not shown). Here the ensemble members show distinct ridges and almost no trough. In Pert both the analysis and the control forecast lie close to the mean in the downstream trough at ET time. Here some members show distinct troughs and ridges. Therefore, the region downstream of ET at 21 September 00 UTC (Fig. 5.11) in which the spread is well represented is larger in Pert than in Nopert.

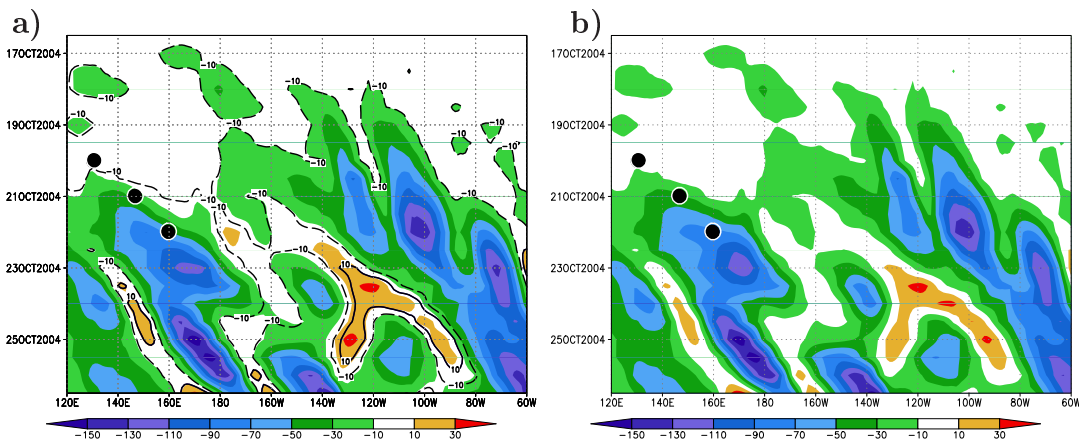


Figure 5.11: Hovmoeller plot of the difference $\text{RMSD} - \text{RMSE}$ of the geopotential height (m) at 200 hPa within the ensemble runs for Pert (a) and Nopert (b) averaged between $30^\circ - 60^\circ$ N. 10-day forecast from FCST1. TC positions are marked by black dots. The isolines that define the regions in which the spread is well represented in Nopert (b) are marked by black lines (-10: dashed, 10: solid) in (a).

Both in Pert (Fig. 5.11 a) and in Nopert (Fig. 5.11 b) negative values can be seen around the TC position from 21 October 00 UTC but in Pert the TC lies rather at the edge while in Nopert the TC is located well within these negative values. The fact that in Pert the spread represents the uncertainty in the trough downstream of the ET event correctly in a relatively large area compared to Nopert can be seen as an improvement in the ensemble forecast around ET time through the perturbations targeted on Tokage.

Comparing the regions in of well represented spread of Nopert marked by black lines with those of Pert (Fig. 5.11 a) it is interesting that until 22 October 12 UTC the plume directly downstream of Tokage is broader in Pert than in Nopert while the second plume further downstream is almost equally broad in Nopert than in Pert. From about 23 October 00 UTC the situation is reversed. In the second plume further downstream the plume of values close to zero or positive values is larger in Pert than in Nopert while in the

first plume the regions of well represented spread are almost equally broad in Pert and in Nopert. This suggests that the better representation of the spread through the targeted SVs propagates downstream with about 25° per day. This corresponds approximately to the results of Szunyogh et al. (2002) who found a propagation of the signal due to targeted observations with dropsonde data of 30° per day.

Note that the improved representation of spread due to the targeted perturbations can only be seen through the difference between Pert and Nopert. The two plumes of well represented spread downstream of Tokage's ET which are present in Nopert as well cannot be attributed to the better representation of spread due to the targeted perturbations.

Information about the dispersion and downstream propagation of the changes in spread due to the targeted perturbations can be obtained by comparing the RMSD of Pert with the RMSD of Nopert. This difference can be referred to as signal of the additional targeted perturbations. Using the RMSD as measure of spread instead of, for example, the standard deviation has the advantage that only the differences in the perturbed ensemble members are compared as the same control forecast is used in each case. If the STD would be used there would be an additional signal due to the differences in the ensemble means.

The results are presented at 200 hPa (Fig. 5.12, left) and 500 hPa (Fig. 5.12, right) together with the geopotential height of the control forecast at these levels. Additionally the Eady index is presented at 200 hPa to get information about the coincidence of regions of high baroclinic instability with the growth of the signal. The analyzed position of Tokage is shown by a black hurricane symbol.

Two days before Tokage underwent ET the typhoon can be seen at about 130° E and 25° N (Fig. 5.12 a, b). At this forecast time a small-scale positive signal is located around it and a larger one north of it in the midlatitudes at 200 hPa (Fig. 5.12 a) indicating higher spread in Pert. At 500 hPa (Fig. 5.12 b) a signal of higher positive values than at 200 hPa can be found around Tokage. A noticeable difference between the 200 hPa and 500 hPa level is that in the latter the signal is constrained around the TC before ET time (Fig. 5.12 b, d) while the larger part in scale and value in the former (Fig. 5.12 a, c) can be found in the midlatitudes north and downstream of the TC from 2 days before

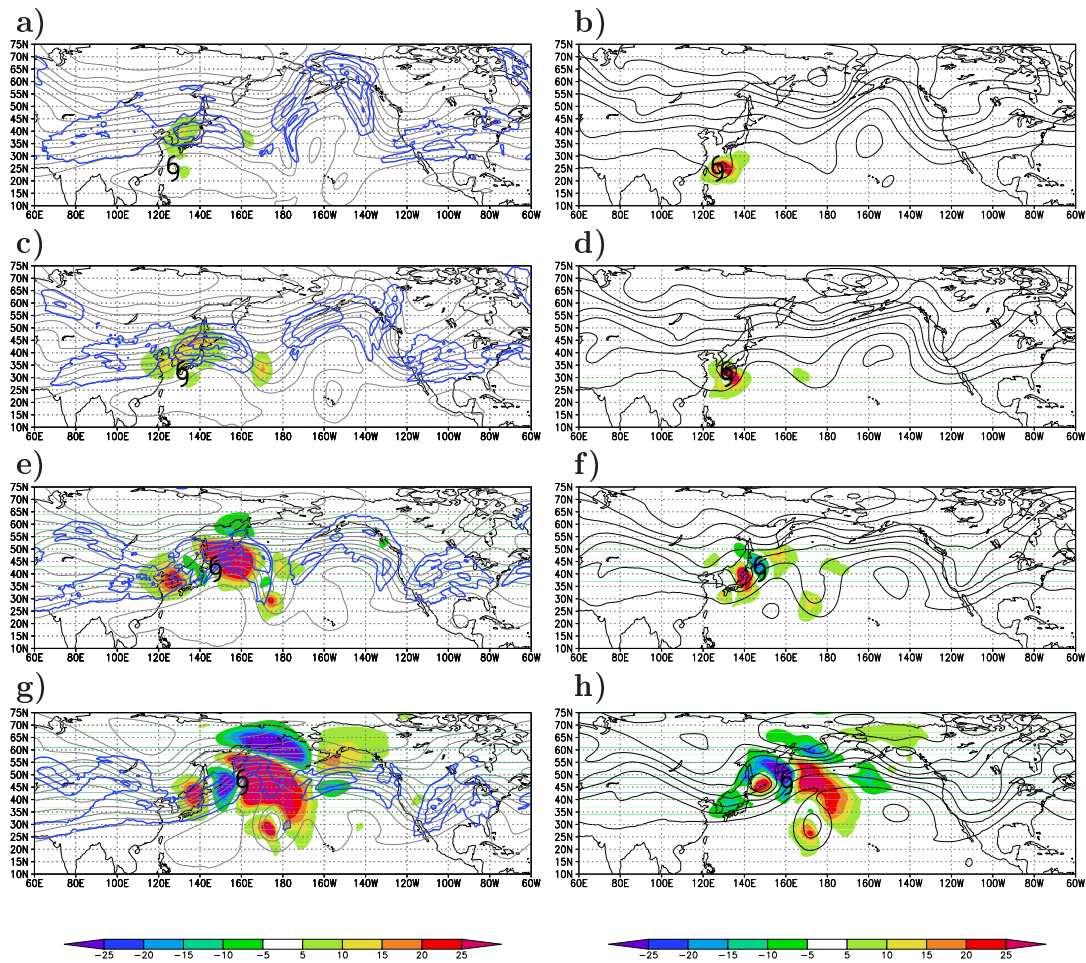


Figure 5.12: RMSD difference of the geopotential height (m) at 200 hPa (a, c, e, g) and 500 hPa (b, d, f, h) between the ensemble forecasts from FCST1 with and without targeted perturbations on Tokage (shaded). Forecasts for 48 hours prior to ET (a,b), for 24 hours (c,d) prior to ET, for ET (e,f) and for 24 hours after ET (g,h). ECMWF control forecast of geopotential height (black contours). Eady index (blue contours, values ≥ 0.6 , interval: 0.4).

ET already. Moreover, the signal at 500 hPa does not seem to grow neither in amplitude nor in scale until ET time. In contrast, strong growth of the signal at 200 hPa in the midlatitudes can be seen directly upstream of a maximum of the Eady index.

This may be understood considering that the major parts of the initial midlatitude SVs were located at 500 hPa (section 5.2). From there, the energy of extratropical SVs propagates upwards in the atmosphere when the initially upshear tilted SVs are untilted (Buizza and Palmer, 1995; Badger and Hoskins, 2000; Reynolds et al., 2001) as explained in section 5.2. Around the TC itself the initial SVs were higher up in the atmosphere. Badger

and Hoskins (2000) showed in their investigation of baroclinic growth mechanisms that perturbations in the upper troposphere do not have a strong effect on perturbation growth further downwards. In contrast, perturbations in the lower or midtroposphere strongly influence perturbation growth further upwards. Therefore, in the midlatitudes strong growth of the spread in scale and amplitude is found for Pert in the upper troposphere and not so much around the TC at 500 hPa and 200 hPa. Both the signals at 200 hPa and 500 hPa propagate downstream in the midlatitudes. It is supposed that through the close connection between the processes in the inner core of a TC and its outflow disturbances in the core (Fig. 5.12 b, d) lead to disturbances in the outflow.

The evolution from 2 days to 1 day before ET at 200 hPa (Fig. 5.12 a, c) follows that discussed in section 2.3.3. It is hypothesized that the advection of potential temperature due to the anticyclonic circulation in the outflow of Tokage has steepened the ridge and it is advected downstream by the high upper level wind speeds. This leads to a shift of the anticyclonic part relative to the cyclonic part of the circulation of the TC. The signal is advected with the outflow. Through the northerly winds at the east of the outflow the downstream trough deepens and finally a cut-off low is formed. The signal seems to have propagated from the outflow into that cut-off low in which the signal remains stationary from ET time until at least 24 hours thereafter (Fig. 5.12 e, g). The southerly flow both at the west of the outflow and the east of the cyclonic circulation associated with the core of the TC act to steepen the ridge.

From ET time on the signal in the cut-off low grows markedly at 500 hPa as well (Fig. 5.12 f, h). Such a shift in time between the propagation of the signal at higher and lower levels has been found by Szunyogh et al. (2002) as well. The surface signal of their targeted observations followed the 300 hPa signal with 12 - 24 h delay.

The small scale signal around the TC at 200 hPa (Fig. 5.12 e near 125° E and 35° N) starts to grow strongly as soon as it interacts with the baroclinic zone. This might be attributed to the growth of uncertainties due to the unshielding of the typhoon's PV through the high vertical gradient of horizontal wind. At ET time the increase in spread in Pert compared to Nopert at 200 hPa (Fig. 5.12 e) exceeds the values seen at 500 hPa (Fig.

5.12 f). Two smaller-scale positive signals can be seen in the upstream and downstream trough of the trough-ridge-trough pattern associated with the ET of Tokage and a larger-scale positive signal is located at the crest of the ridge at 200 hPa. At 500 hPa all the signals are of smaller scale with one small negative region. From 24 hours after ET the negative values at 200 hPa and 500 hPa grow (Fig. 5.12 g, h).

Examining the spaghetti plots (Fig. 5.13) of Pert (blue) and Nopert (red) provides the information that the negative signals can be explained in parts by a shift of the regions of high variability in the ensemble members. At 24 hours after ET the negative signal directly east of Japan at 200 hPa (Fig. 5.12 g) is due to the further eastward position of one of the locations of high variability in the Nopert (red) members (Fig. 5.13 a). Around $150^\circ - 160^\circ$ E some Nopert members can be seen on the southern side of the members further south east than the Pert members. West of Japan some blue members are located further to the west than all of the red members. Hence, the region of high variability in Nopert is shifted to the east relative to that of Pert leading to the positive signal west of Japan and the negative signal east of Japan (Fig. 5.12 g).

This shift can be seen more clearly in the region of larger negative and positive signals between 160° E and 180° (Fig. 5.13 a). A lot of red members are situated north of 60° N describing higher amplitude ridges where only three of the blue members are found. In contrast, there are several blue members around 50° N and further south forming deeper troughs. Here no red member is seen. Consequently, the high variability of Pert is shifted south relative to the high variability in Nopert. Comparing the ensemble means of Pert (black, solid line) and Nopert (black, dashed line) confirms both the east-west shift to the west of Japan and the north-south shift between 160° E and 180° .

At 500 hPa (Fig. 5.13 b) the shift lies rather in the transition from the upstream trough to the ridge that is associated with high variability in the ensemble members between 140° and 165° E. The Pert members are located further to the west. A lot of them are seen between 140° and 150° E. No Nopert member is seen in the area north of 45° N and west of 148° E. This is where the small region of positive values is seen in Fig. 5.12 h. Again the trough-ridge pattern in the red members reaches 160° E earlier than the blue

members. The ensemble means demonstrate the shift as well. It is obvious, however, that the positive signals cover a larger area and the values are higher than the negative values. Hence, the shift is responsible for the higher spread in Pert only in relatively small parts.

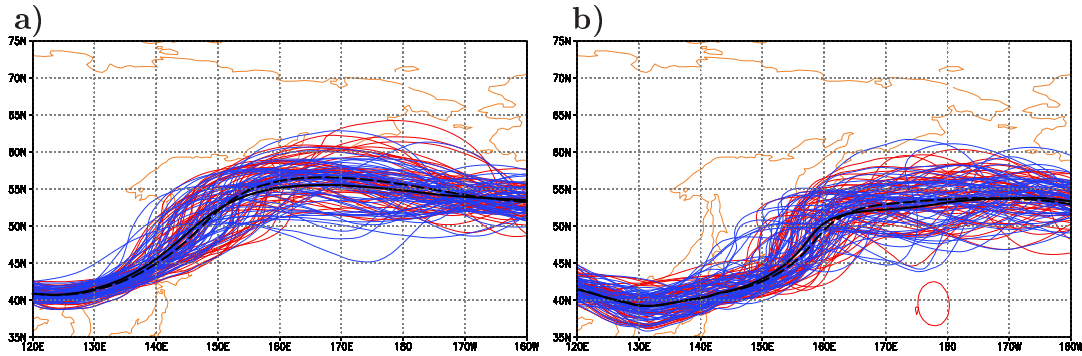


Figure 5.13: Spaghetti plots of the 1150 gdam geopotential height at 200 hPa (a) and the 545 gdam geopotential height at 500 hPa (b) of the ensemble forecasts from FCST1 for Pert (blue) and Nopert (red) targeted perturbations on Tokage (shaded) for 24 hours after ET (corresponding to the time of Figs. 5.12 g, h). Ensemble mean of Pert (black, solid) and Nopert (black, dashed).

Comparing the locations of the large regions of positive values in Fig. 5.12 from ET time on with the regions of well represented spread in the difference of spread and RMSE (Fig. 5.11) illustrates that the perturbations targeted on Tokage are responsible for the correct representation of the spread in this region. Furthermore, the higher spread in the runs with Tokage perturbations and its downstream propagation illustrates that uncertainties induced by an ET event can reduce the predictability in the vicinity of the event and far downstream.

It is obvious that the leading edge of the signal propagates with a speed of over 20° per day to the east which is a bit slower than the signal propagation of 30° day found by Szunyogh et al. (2002).

It is a fundamental property of waves that they transport energy over long distances compared to the displacement of the individual fluid particles and hence can cause disturbances far downstream of the region where the initial perturbations were introduced. The amplitude of the envelope of a wave packet determines where there is wave energy (Pedlosky, 1987). The farthest location to where the signal can propagate is the leading edge of the wave packet. In other words the signal can travel with the group velocity. The

leading edge of the wave packet is also the most likely location of downstream cyclogenesis (Szunyogh et al., 2002).

The group velocity of the Rossby-wave-train excited by Tokage's ET and its coherence with the propagation speed of the perturbations is illustrated with the aid of Hovmoeller-plots. The development of the same signal between the RMSD of Pert and the RMSD of Nopert as shown in Fig. 5.12 during 10 days is visualized at 200 hPa and 500 hPa averaged over 30 - 60° N (Fig. 5.14). In addition, the analyzed meridional wind component which indicates the excitation and propagation of the Rossby-wave-train is presented.

The ridge steepening from 20 October 00 UTC associated with the outflow of Tokage at 200 hPa can be seen by the dipole in the meridional wind component at 125 - 170° E in the Hovmoeller plot (Fig. 5.14 a). The positive values associated with southerly winds can be seen slightly further east at 500 hPa (Fig. 5.14 b) indicating a developing system. The alternating positive and negative values of the meridional wind component illustrate a downstream propagating Rossby wave (marked by a blue dashed line). To the east of Tokage's ET a preexisting wave can be seen but clearly the wave emanating from the dipole did not exist before. This suggests that it was excited by Tokage's ET even though the downstream propagating of the wave starts only 3 days after the ET.

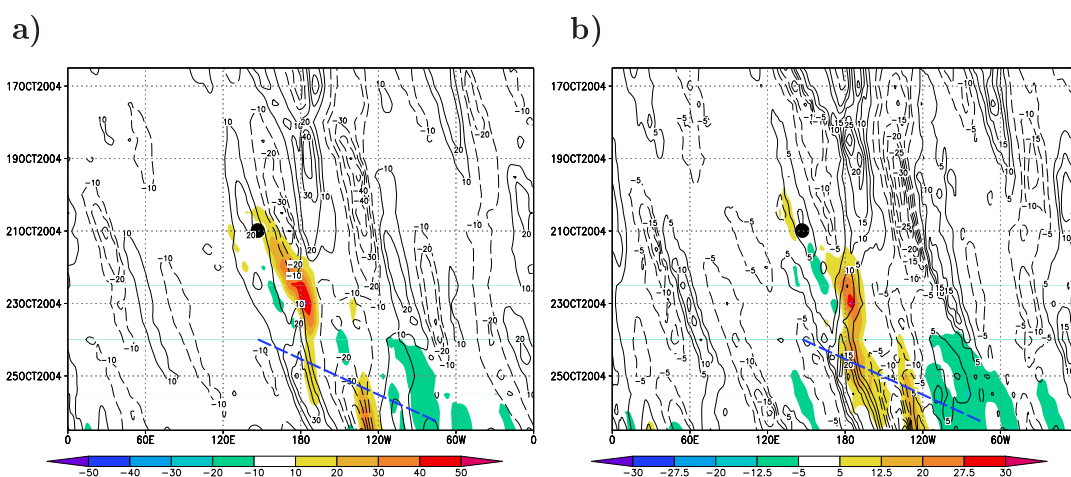


Figure 5.14: Hovmoeller plot of RMSD difference of the geopotential height between the ensemble runs with and without targeted perturbations on Tokage (shaded, m) and analyzed meridional wind component (contours, ms^{-1}) at 200 hPa (a) and 500 hPa (b) averaged between 30° - 60° N. 10-day forecast from FCST1. ET position is marked by a black dot.

The regions of high uncertainty located upstream at about 125° E and downstream of the ET of Tokage from about $150 - 160^{\circ}$ E at 200 hPa (Fig. 5.14 a) are associated with the upstream trough and the ridge directly downstream of the ET system (see Fig. 5.12 e). The uncertainty propagates downstream with increasing forecast time. The weak signal in the upstream trough can be seen from 00 UTC 21 until 00 UTC 22 October. Subsequently, the signal in the ridge grows, broadens and travels with the ridge to the east. From about 23 October the signal remains stationary around the cut-off low at about 180° for two days and becomes narrower again. At 24 October 00 UTC, i. e. 2 days after the time shown in Fig. 5.11 g and h, it is associated with the trough downstream of the ridge. At the end of the forecast interval a positive signal is located in the downstream trough that has traveled to 120° W.

The propagation of the signal with the Rossby-wave-train can be seen even more clearly at 500 hPa (Fig. 5.14 b). The uncertainty is associated with the same features as at 200 hPa, the trough-ridge-trough, however, is shifted to the east compared with 200 hPa which is a necessary condition for growing baroclinic disturbances. The signal is associated with the interaction of Tokage with the midlatitudes first, than it travels downstream into the uncertainty associated with the downstream ridge and finally it can be found in the trough downstream of the ridge analogous to 200 hPa. For this longer time interval of 10 days this would again result in an average propagation speed of over 20° per day both at 200 hPa and at 500 hPa as seen in Fig. 5.12. The phase velocity of the Rossby wave can be estimated to be about 10° per day. The signal between Pert and Nopert seem to propagate at the leading edge of the wave packet confirming the results of Szunyogh et al. (2002). The negative signals downstream of the positive ones result mainly from a shift of the ensemble mean of Pert to the west versus the ensemble mean of Nopert as seen earlier.

The growth and downstream propagation of the perturbations that have been calculated for the optimization region around Tokage illustrates the possible impact of forecast errors growing during ET. They can reduce the predictability over an entire ocean basin up to the west coast of the next continent.

5.3.3 Response on Clustering

The regions of higher spread in Pert compared to Nopert have been investigated with the analysis method described in section 4.3 to get information about the synoptic development and to see if the differences between Pert and Nopert described above are manifested in the clustering.

The EOF patterns in Pert (Figs. 5.15 a, b) show the highest variability in the amplitude pattern while in Nopert (Figs. 5.15 c, d) the highest percentage of the total variability is explained by the shift pattern (Table 5.1). The large minimum and maximum of the variability at the front and the rear of the ridge in EOF1 of Nopert (Fig. 5.15 c) are shifted upstream in Pert (Fig. 5.15 a) such that they are located at the crest of the ridge and in the upstream trough with a small additional minimum in the downstream trough. That corresponds to the upstream shift of the uncertainty in Pert versus Nopert that caused the negative values in Fig. 5.12. The variability patterns in EOF2 have smaller scales both for Pert and Nopert. If the signs of EOF2 of Nopert are exchanged, the centers of action for EOF2 in Pert are shifted upstream of those in Nopert also. The center of action at the crest of the ridge in Nopert can be seen to the west of the ridge in Pert while the center of action in the downstream trough in Nopert seems to be shifted to the east of the ridge in Pert.

Grouping the ensemble members according to their contribution to the first two EOFs, four clusters are obtained in Pert and only three in Nopert. Two of the Pert clusters are shown in Figs. 5.16 a, b and two of the Nopert clusters in Figs. 5.16 c, d for 21 October 12 UTC (12 hours after ET). The two clusters of Pert that contribute positively to the amplitude pattern are very similar to two of the Nopert clusters that contribute positively and neutrally to the amplitude pattern. However, in the Pert clusters the central pressures vary more. While in Nopert the minimum values are about the same, in Pert one of the clusters shows a 10 hPa higher (Figs. 5.16 a, c) and the other one a 5 hPa lower (Figs. 5.16 b, d) central mean sea level pressure than the respective most similar Nopert cluster. In the clusters that contribute positively to the shift pattern (Figs. 5.16 a, c) the ET system has developed quickly and the central mean sea level pressure is further to the east than

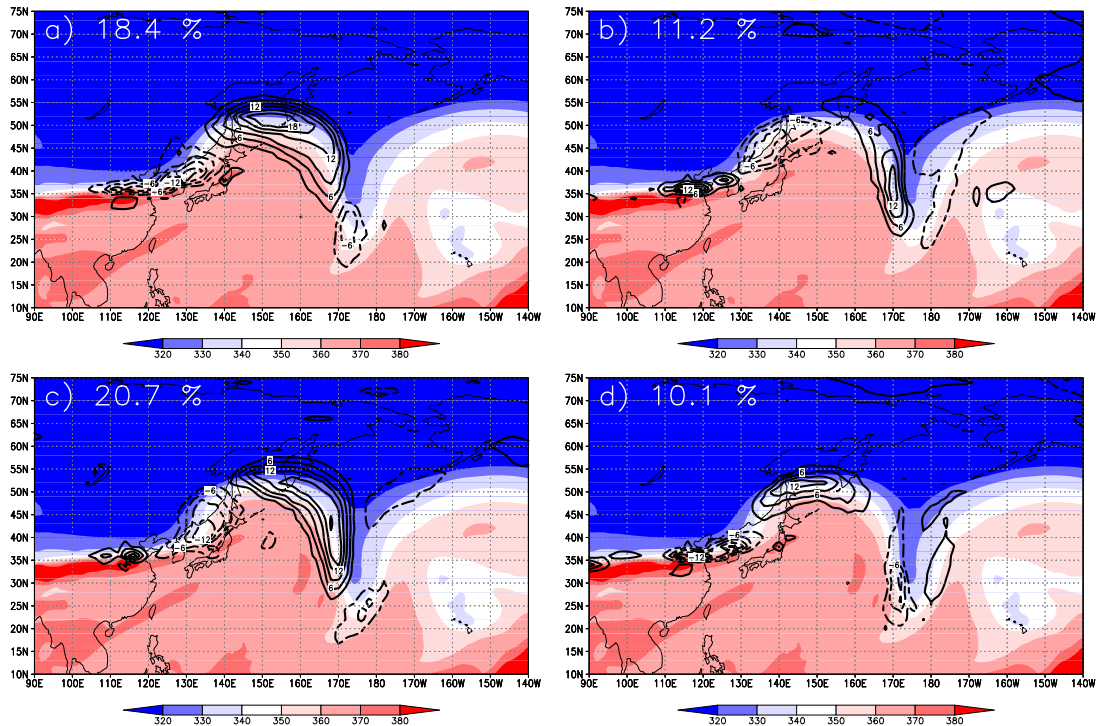


Figure 5.15: Ensemble mean of potential temperature on the dynamic tropopause (shaded, K) for Pert (top) and Nopert (bottom) for the forecast from FCST1. EOF1 (a, c) and EOF2 (b, d) are shown in contours at an interval of 3.0 K. The percentage of their contribution to the total variability is marked in white in the top left corner.

in the clusters that contribute neutrally (Fig. 5.16 b) or negatively (Fig. 5.16 d) to the shift pattern.

All the clusters in Fig. 5.16 contribute positively or neutrally to the amplitude pattern leading to high ridges and deep downstream troughs that developed to cut-off lows. The clusters that contribute neutrally (Fig. 5.16 b) or negatively (Fig. 5.16 d) to the shift pattern form a sharp upstream trough that wraps up cyclonically (Thorncroft et al., 1993) leading to strong re-intensifications of the ET systems. In each of the clusters in Fig. 5.16 Tokage re-intensifies strongly.

In Fig. 5.17 clusters of Pert and Nopert that contribute negatively to the amplitude pattern are shown. Fig. 5.17 a shows a rather zonal development in the midlatitudes polewards of the Ex-TC and no re-intensification. The downstream trough is weaker and broader and no cut-off low is seen. In this cluster the position of the TC is too far south

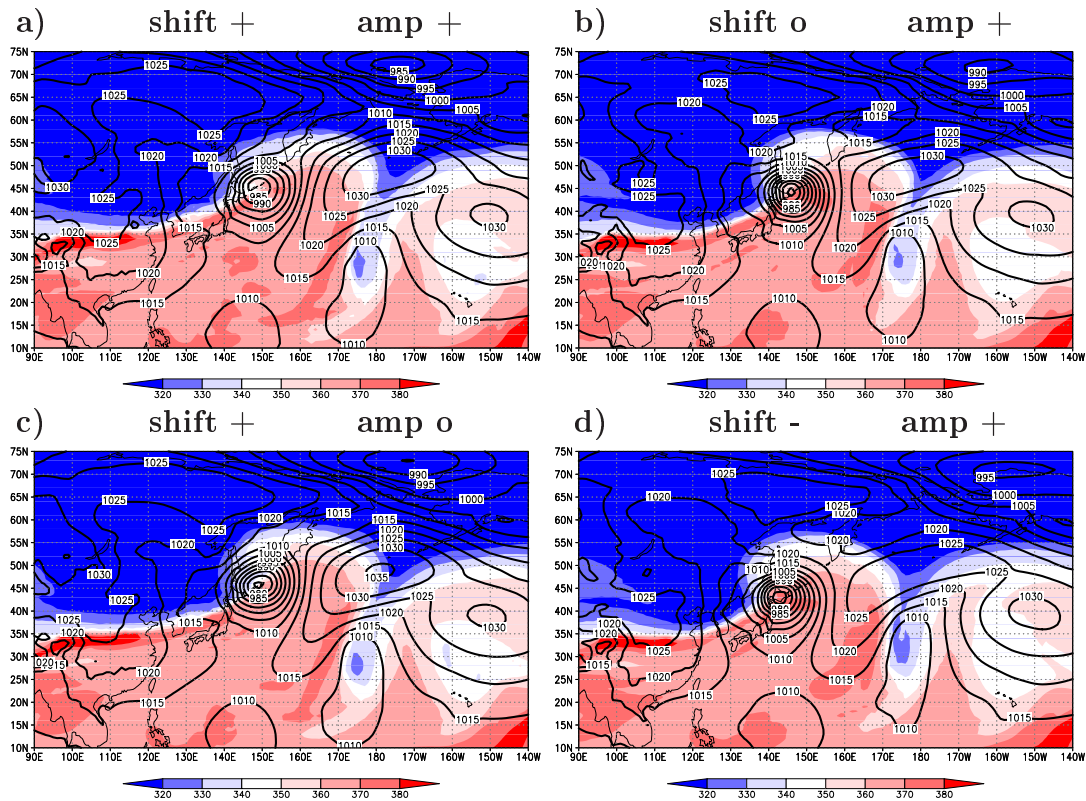


Figure 5.16: 2 of 4 clusters for Tokage in Pert (a, b) and Nopert (c, d) for the ensemble forecast from FCST1 valid on 21 September 12 UTC, i. e. 12 hours after the investigation time.

of the midlatitude trough upstream, a position that is not favorable for re-intensification.

The cluster in Fig. 5.17 b contributes negatively to the shift pattern. This results in an ET system that is rather in an earlier stage than the ensemble mean but will re-intensify strongly. The midlatitude flow pattern in the Nopert cluster (Fig. 5.17 c) is of higher amplitude than that in the Pert cluster that contributes positively to the shift pattern (Fig. 5.17 a) but not as high as that in the Pert cluster contributing negatively to the shift pattern (Fig. 5.17 b). The downstream trough is almost as weak as in the Pert cluster in Fig. 5.17 a. Furthermore the central mean sea level pressure in the Nopert cluster is about 10 hPa deeper than in the weakest Pert cluster (Fig. 5.17 a).

Comparing the clusters in Figs. 5.16 and 5.17 to the analysis of Tokage (Fig. 4.2) the impression is obtained that the analyzed structure of the midlatitude flow is most similar to the cluster in Fig. 5.16 a but the intensity of the central mean sea level pressure is in

between the clusters in Figs. 5.17 a and b. The important difference between the weakest Pert cluster (Fig. 5.17 a) and the analysis is that the weak central pressure in the cluster does not result from the landfall as in the analysis but from the unfavorable relative positions of the TC and the midlatitude trough. All the clusters without the additional targeted perturbations around Tokage represent the ET system stronger than the analysis in agreement with the results of section 5.3.1.

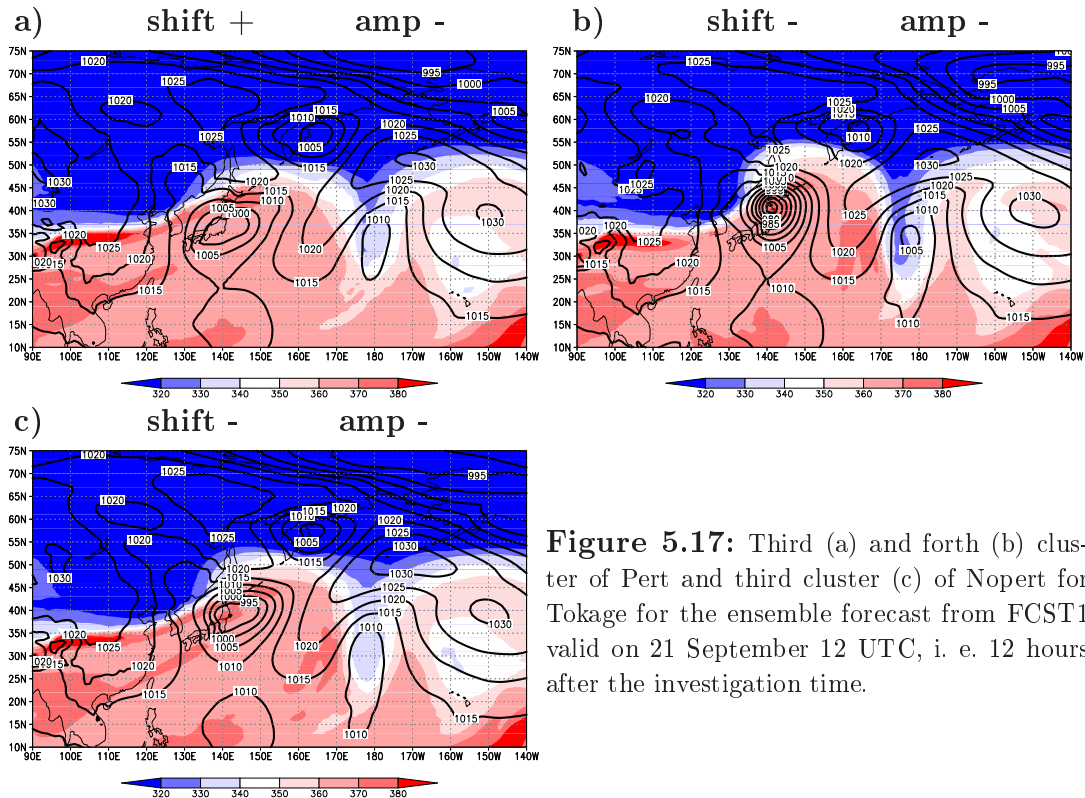


Figure 5.17: Third (a) and fourth (b) cluster of Pert and third cluster (c) of Nopert for Tokage for the ensemble forecast from FCST1 valid on 21 September 12 UTC, i. e. 12 hours after the investigation time.

The comparison of the experiments, in which additional perturbations around Tokage were not calculated, with the experiments with Tokage perturbations illustrates that the targeted perturbations are essential in representing the spread directly downstream correctly. Even though the abrupt filling of Tokage after landfall could neither be captured by the ensemble with nor by the ensemble without Tokage perturbations, the targeted perturbations yield a higher amount of possible ET scenarios that accounts for the uncertainty associated with the ET of Tokage. The ensemble forecast without the targeted perturbations would assign a too high probability to a wrong atmospheric development. The weakening of Tokage is encompassed in the runs even though it is due to the unfa-

favorable position of Tokage relative to the upstream trough and not due to landfall. The higher spread due to the targeted SVs propagates downstream faster than the phase of the trough-ridge-trough pattern illustrating the influence of forecast errors due to an ET on the predictability in regions far downstream.

The clustering method is capable of identifying a group of weaker members in the Pert runs that is essential in including the comparatively weak development of the analysis in the ensemble.

5.4 Influence of stochastic physics

In this section the impact of the perturbations of the parameterized tendencies through stochastic physics on the ensemble spread during the model run is investigated. In the following the runs with and without stochastic physics are referred to as “Sto” and “Nosto” respectively. For the purpose of isolating the influence of the stochastic physics on the ensemble run, the optimization region around Tokage, on which the additional perturbations are targeted, is switched off as in “Nopert”.

5.4.1 Effect on tracks

The ensemble track forecast, the analysis, the deterministic forecast and the best track have been investigated as in section 5.3.1. It was found that the track forecast in the Nopert/Sto runs (Fig. 5.18) showed slightly higher spread around the recurvature than Nopert/Nosto such that the analyzed track was at the edge of the ensemble tracks or slightly outside only at 60 h forecast lead time. In the Nopert/Nosto runs the analysis laid outside of the spread for the forecast lead times 48 h and 60 h (Fig. 5.9 b). Around ET time both runs yield quite similar track forecasts. Still a gap comparable to Nopert/Nosto can be seen after the analyzed ET. The analysis and the best track are located in this gap from 12 hours after ET.

At later forecast times (156 h - 168 h) the ensemble members are more widely distributed

than in Nopert/Nosto and also than in Pert/Nosto (Fig. 5.9). A lot of ensemble members forecast a more north-south track of Tokage from 144 hours forecast time resulting in an interaction with the midlatitude flow west of the Kamchatka peninsula in contrast to the rather southwest-northeast tracks in Pert/Nosto and Nopert/Nosto. In fact, the most of the tracks are west of the deterministic forecast assigning a high probability to a north-south track of Tokage. However, slightly more members can be seen south of the analysis as well and hence, through the stochastic physics, a higher probability is assigned to the typhoon moving into this more southern region.

Consequently, the range of probable tracks forecast by the ensemble runs with the stochastic physics diverge further from each other than the Nosto runs at the end of the forecast interval. Thus Nopert/Sto accounts sufficiently for the high uncertainty but more weight is given to the erroneous development west of the deterministic forecast than in the Nosto runs.

Inspecting the forecast positions of Nopert/Sto for the analyzed ET time (bottom right corner of Fig. 5.18) it is found that they are more widely distributed than in Nopert/Nosto, i. e. more positions are forecast further to the west, and two members forecast the position very close to the analyzed position at ET time. However, less members than in Pert/Nosto forecast Tokage to the south of the analysis and the positions forecast by the very slow members that are located above Kyushu in Pert/Nosto are not seen in Nopert/Sto. Hence, less emphasis is laid on the analyzed track than in Pert/Nosto.

Thus, the runs with stochastic physics yield a slightly better agreement with the analysis and the best track at recurvature. Furthermore, the stochastic physics is mainly responsible for enhancing the spread at later forecast times, i. e. it accounts for the uncertainty after long times. However, the runs with the stochastic physics put too much emphasis on the wrong tracks and the uncertainty both around the recurvature and the ET is still underrepresented. Consequently, the stochastic physics alone cannot account for the uncertainties associated with the ET of Tokage.

Comparing the spread in terms of central mean sea level pressure for Sto and Nosto the rapid increase of spread close to initialization time in Nopert/Sto (Fig. 5.19) attracts

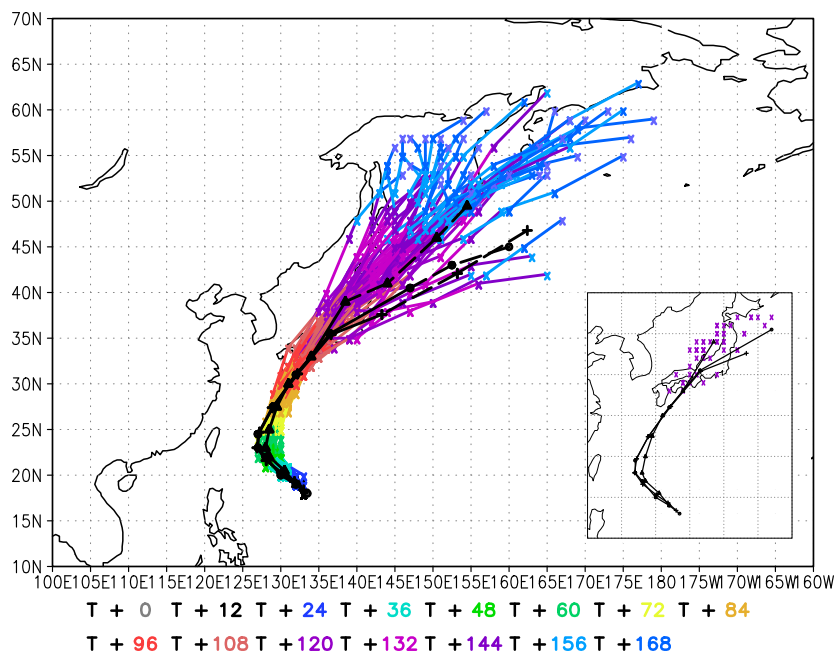


Figure 5.18: Same as Fig. 5.10 b but for the runs with stochastic physics.

attention. Around 48 to 84 h forecast lead time the spread in the central mean sea level pressure for Nopert/Sto is higher than for Pert/Nosto (Fig. 5.10 a). However, only two of the members in Nopert/Sto (Fig. 5.19, thin black lines) show a weakening to the pressure values of the analyzed Tokage with a delay of about 12 hours. The weakening can be attributed to landfall for only one of them. The other one has a track too far south of the strong midlatitude tropopause potential temperature gradient in an unfavorable position for an interaction. A third member (purple) shows a weakening of the system almost to the central pressure values of the analysis after 144 hours forecast time with a strong re-intensification thereafter. This member weakens due to the landfall as well and develops in a quite similar manner to the analysis. While in the Pert/Nosto runs several members have central mean sea level pressure values between 980 and 990 hPa between 108 and 120 hours, all but three members in Nopert/Sto stay below 980 hPa central mean sea level pressure until 156 hours forecast lead time.

The increase of the spread in the central mean sea level pressure of the ensemble members for shorter forecast times and our results for the track forecasts of Nopert/Sto agrees

with the conclusions of Puri et al. (2001) who found that stochastic physics leads to a smaller spread in the TC tracks than targeted initial perturbations but to a much larger spread in the central pressures also at shorter forecast times. As stated for the targeted perturbations (section 5.3.1) the explanation lies in the scales. The targeted singular vectors have larger scale structures (compare section 5.2.1) and thus they influence the tracks. The stochastic physics act on the smaller scale features like convection and thus have an impact on the central pressure. Puri et al. (2001) attribute large variation in the central pressures to the convective forcing in the stochastic physics. They ran the EPS with and without the convective forcing included in the stochastic physics and found that the spread in the central pressures without the convective forcing resembled the runs without stochastic physics. Therefore, most of the variation seems to be due to perturbations in the temperature and moisture field.

However, in the case of Tokage after ET a shift of the central mean sea level pressure to deeper values can be seen rather than a larger variability. The pressures in Nopert/Sto decrease even stronger than in Nopert/Nosto (Fig. 5.10 b) such that at 144 h forecast lead time all but the three weak members fall below 965 hPa. In Nopert/Nosto several members can be seen that have central mean sea level pressures between 980 and 965 hPa. Puri et al. (2001) found that while the targeted perturbations are responsible for capturing the weakening of the TC the stochastic physics leads to an overall deepening in central pressure. For the cases that Puri et al. (2001) investigated this led to an improvement of the representation of the analysis by the ensemble. In the case of Tokage, however, the deepening shown by a large part of the members leads to a decrease of the skill of this forecast. In the ensemble track forecast for Nopert/Sto it was seen that a lot of tracks are located west of the deterministic forecast. The position of these members around ET time seems to be closer to the tropopause potential temperature gradient and even more favorable for an interaction with the upstream trough and a deep re-intensification than the position in the deterministic forecast.

Clearly, distinct uncertainties must be associated with the boundary layer parametrization and the smoothing of the orography. The low resolution of the EPS is not able

to represent mountains like the Fujiyama (over 3700 m) and islands with a horizontal extension of about 400 km like Japan correctly.

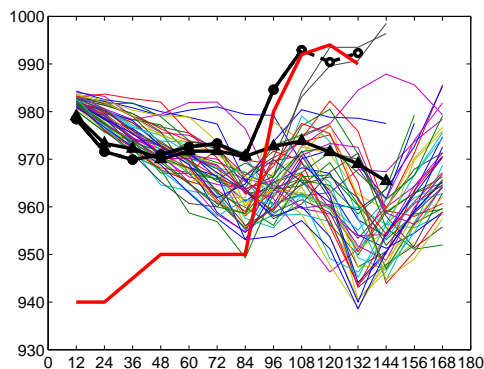


Figure 5.19: Same as Fig. 5.10 b but for the runs with stochastic physics.

The stochastic physics yields a beneficial impact on the ensemble runs only before the weakening after landfall and by yielding one more member that shows a weakening after landfall. Otherwise it leads to a further deviation of the most ensemble members from the analysis than the runs without stochastic physics and without targeted perturbations. It cannot account sufficiently for the weakening of Tokage after landfall.

5.4.2 Effect on the amount of spread

The correct representation of the spread in Nopert/Sto with regard to the RMSE has been investigated analog to Fig. 5.11. The results have been interpreted relative to Nopert/Nosto and Pert/Nosto (section 5.3.2). The sizes of the areas of well represented spread in Nopert/Nosto are visualized in the plot for Nopert/Sto by black lines (Fig. 5.20).

At ET time on 21 October 00 UTC the region of well represented spread downstream of the TC is larger in Nopert/Sto (Fig. 5.20) than in Nopert/Nosto (Fig. 5.11 b). The two plumes of nearly zero or positive values downstream of Tokage are wider than in Nopert/Nosto indicating a better but also a slight overrepresentation of the spread through stochastic physics. It is of interest to investigate the influence on the spread due to the stochastic physics alone (Fig. 5.20) compared to that due to the targeted perturbations

(Fig. 5.11 a). Directly downstream of the ET from 150° E to 180° at 21 October 12 UTC the region of well represented spread in Nopert/Sto is smaller than in Pert/Nosto and stays so in this plume until 22 October 12 UTC.

In spaghetti plots of the 200 hPa geopotential (not shown) it is seen that most of the ensemble members in Nopert/Sto tend to form high amplitude ridges and show higher values of geopotential than the analysis. The analysis lies at the edge of the ensemble members leading to a higher RMSE. However, the plume downstream starting from 170° W to 160° W on 21 October 00 UTC is broader than in Pert/Nosto. Here, in contrast, more members form troughs and show lower values of geopotential than the analysis. Hence the analysis is rather in the ensemble mean leading to a smaller RMSE.

From about 23 October 00 UTC the plume originating from directly downstream of the ET event in Nopert/Sto is broader than in Pert/Nosto. This confirms the statement that the stochastic physics is important in representing the spread correctly for longer forecast intervals as found by Buizza et al. (2004). Further differences between Pert/Nosto and Nopert/Sto can be seen in regions remote from the ET. Before ET time, distinctly broader regions of well represented spread in Nopert/Sto can be seen compared to Nopert/Nosto, especially directly east of 180° (Fig. 5.20). In contrast, in Pert/Nosto the differences between RMSD and RMSE were equal compared to Nopert/Nosto before the ET time (Fig. 5.11 a).

Consequently, while the targeted perturbations play the main role in representing the spread directly downstream of the ET and in the plume further downstream at later forecast times, it is obvious that the stochastic physics is responsible for a better representation of the spread everywhere and especially at later forecast times. This is seen also by the weaker negative maxima compared with Pert/Nosto.

The influence of the stochastic physics on the spread and the downstream propagation of this influence is investigated by the aid of the difference between the RMSD in the runs with and without stochastic physics as in section 5.3.2. On the one hand, this gives information about the impact that the parametrized tendencies can have on the error growth when the remnants of a TC interact with the midlatitudes. If the parametrized

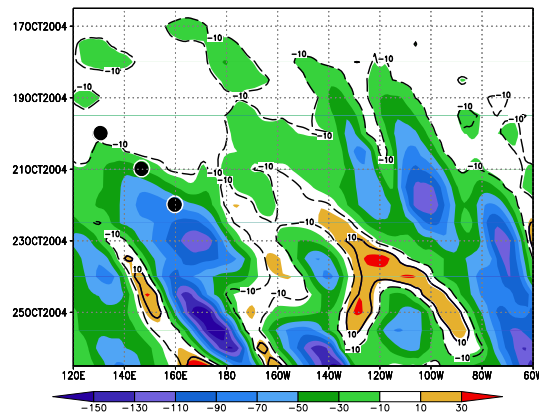


Figure 5.20: Hovmoeller plot of the difference $\text{RMSD} - \text{RMSE}$ of the geopotential height (m) at 200 hPa within the ensemble runs for Nopert/Sto averaged between $30^\circ - 60^\circ$ N. 10-day forecast from FCST1. TC positions are marked by black dots. The isolines that define the regions in which the spread is well represented in Nopert/Nosto (Fig. 5.11 b) are marked by black lines (-10: dashed, 10: solid).

processes during an ET are important, the perturbations of the parametrized tendencies by the stochastic physics are large (Eq. 3.33) and consequently the spread is high. On the other hand, the role that stochastic physics plays in generating more spread can be compared with that of targeted perturbations.

Until 20 October 00 UTC (Fig. 5.21 a) small localized influences of the stochastic physics (also called signal in the following) can be seen distributed over the whole western North Pacific and partly over North America at 200 hPa. At this level and forecast time parametrized processes associated with the upper part of the TC, for example the outflow, seem to be no more important than those in the midlatitude flow that are not localized close to the ET system. Note that at the same time the targeted perturbations influenced the midlatitude flow downstream of Tokage distinctly (Fig. 5.12 c). Hence, at that time the generation of the spread in the 200 hPa geopotential height in the vicinity of the ET event is almost only associated with the targeted perturbations.

At 500 hPa (Fig. 5.21 b) a clear signal can be seen at the location of Tokage. The strong convection at lower levels within a TC is almost entirely parametrized in global forecast models because of its small scales. Consequently, the higher spread at Tokage is probably generated through perturbing temperature and humidity with the stochastic physics. The stochastic physics is important in generating spread in the 500 hPa geopotential height

but comparing Fig. 5.21 b to Fig. 5.12 d it is clear that the influence of the targeted perturbations at this time is larger.

One day later, at ET time, three regions of high amplitude signal can be seen at 200 hPa (Fig. 5.21 c). These have grown strongly in the last 24 hours and are fairly confined. One is located upstream of Tokage (at about 130° E and 35° N) around the position where most of the ensemble members show the trough that interacts with the typhoon (as seen in spaghetti plots, not shown), i. e. further west than the analyzed position. The second, that is the largest in scale and amplitude at ET time, is seen downstream of Tokage associated with more variability in the representation of the ridge. The signals up- and downstream of Tokage are still smaller in scale and amplitude than the signal between Pert and Nopert (Fig. 5.12 e) at ET time. The third region is farther downstream at about 150° W and 55° N and almost stationary. It has grown strongly from 24 hours before ET (Fig. 5.21 a) and is not connected to the ET event. Because this third region at 200 hPa is hardly visible at 500 hPa it is supposed that the parametrized tendencies associated with upper-level turbulence are responsible for the perturbation growth in this region. This signal is responsible for the better representation of the spread in the plume at about 170° W to 160° W stretching downstream from 21 October 00 UTC (Fig. 5.20).

At 500 hPa (Fig. 5.21 d) the signal upstream of Tokage's analyzed position is still small-scale. Presumably, it is connected to the convective cores of the TCs shown by some of the ensemble members (compare TC centers in bottom right corner of Fig. 5.18). Around 147° E and 17° N a similar signal in the stochastic physics associated with Typhoon Nock-Ten (2004) can be identified.

One day after ET the signals at 200 hPa (Fig. 5.21 e) have grown further and a small part of the signal directly downstream of Tokage has propagated into the cut-off low that is located at about 175° E and 30° N. The influence of the stochastic physics has not grown as strongly as the influence of the targeted perturbations yet. This agrees with the comparison of the RMSD with the RMSE (Fig. 5.20).

A part of the signal associated with Tokage at 500 hPa (Fig. 5.21 f) has propagated downstream one day after ET time. Three days after ET (not shown) the signal covers

an area of 30° in longitudinal and 20° in latitudinal direction at 200 hPa. Almost no negative values can be seen in Fig. 5.21. Thus, in contrast to Pert/Nosto, the plume of Nopert/Nosto ensemble members, and hence the variability in Nopert/Nosto, is not shifted compared to the variability in the members in Nopert/Sto.

These results confirm the statement found by investigating the differences of RMSD and RMSE (Fig. 5.20) that for longer forecast times the stochastic physics is mainly responsible for the generation of spread.

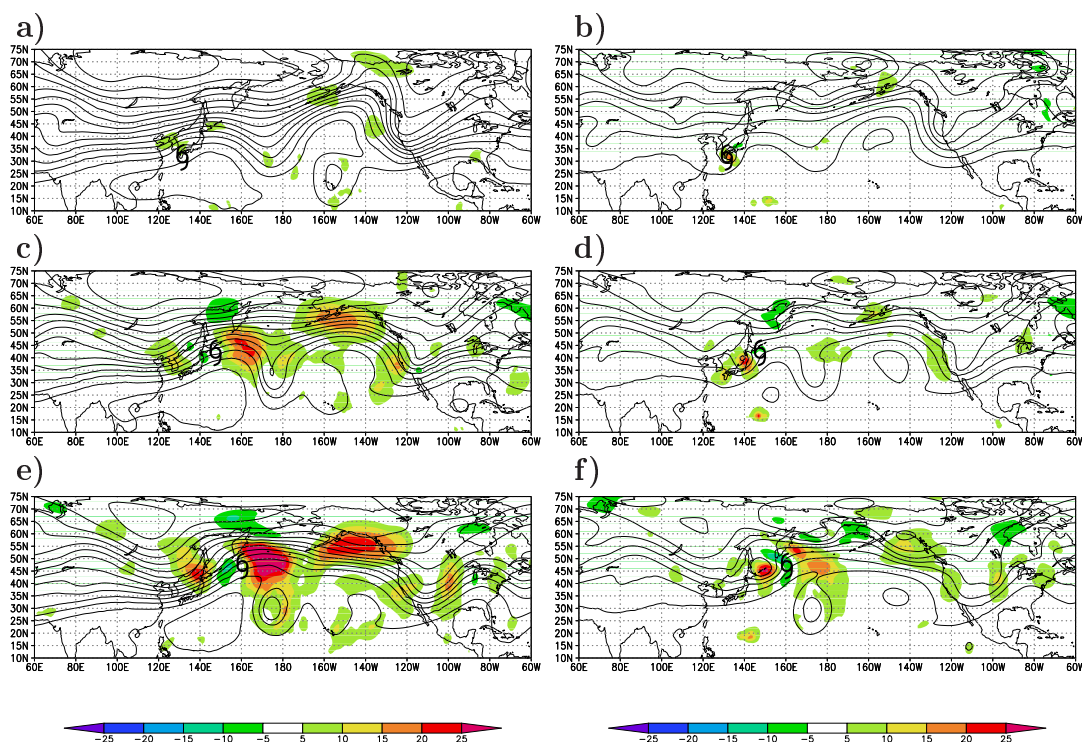


Figure 5.21: Same as Fig. 5.12 but for ensemble runs with and without stochastic physics. Forecasts for 24 hours prior to ET (a, b), for ET time (c, d) and for 24 hours after ET (e, f). The position of Tokage is marked by a black hurricane symbol.

A better physical understanding of this role can be gained by investigating the change in spread of variables like temperature and wind because, together with specific humidity, these are the variables that are perturbed by the stochastic physics (Buizza et al., 1999). It is supposed that parametrized processes in the mid-troposphere are represented to large parts by gridscale temperature tendencies (Puri et al., 2001) and that parametrized processes in the upper troposphere, e. g. turbulences in the jet, are represented by gridscale

tendencies in the wind field as convection plays no role in the upper troposphere. Therefore, the 500 hPa RMSD difference in the temperatures and the 200 hPa RMSD difference in the horizontal windspeed between Sto and Nosto is shown for forecasts from FCST1 (Fig. 5.22). Additionally, the control forecast of the temperature is shown at 500 hPa (Fig. 5.22, right) and the control forecast of the potential temperature on the dynamic tropopause (Fig. 5.22, left).

One day before ET a signal in form of a large ring can be seen covering the strong gradient in the potential temperature at the dynamic tropopause that describes the shape of the ridge downstream of Tokage. Considering a satellite picture of Tokage taken on 20 October 2004 0156 UTC (Fig. 5.23), i. e. about 2 hours after the time shown in Fig. 5.22 a and b, it is obvious that the outer rim of the cloud shield from Tokage's outflow corresponds well with the ring of enhanced spread. This suggests uncertainty in the ridge building associated with Tokage's outflow.

At ET time the annular signal of the outflow at 200 hPa (Fig. 5.22 c) has grown in amplitude and radius. It extends further downstream into the upper level trough at about 175° E. The signal still covers the region of the high gradient in the potential temperature associated with the ridge. Signals can be seen in remote regions from the TC also, for example in the deep tropics and in a ridge close to the west coast of the United States, but these signals are smaller in amplitude, less spatially constrained and not connected with the ET of Tokage. In fact, the only signal that has a comparable amplitude with the signal due to Tokage's ET is that at 200 hPa (Fig. 5.22 c) around 140 - 150° E. Its location corresponds with that of Typhoon Nock-Ten and, therefore, is probably associated with the outflow of Nock-Ten.

One day later two regions of large potential temperature gradient can be distinguished at the dynamic tropopause (Fig. 5.22 e) north of Tokage. One of them describes the form of the ridge belonging to the trough-ridge-trough pattern associated with the ET, the other one is associated with a wider weaker extension of that ridge. Maxima of the influence of the stochastic physics can be found around the crest of the ridge directly downstream of Tokage and along the second potential temperature gradient around 60° N and 130 - 160°

E. The enhanced spread associated with the wider weaker extension of the ridge results from more variability in the ensemble members in representing a cyclonic wrap-up of the ridge (Thorncroft et al., 1993) as will be described in section 5.4.3 below.

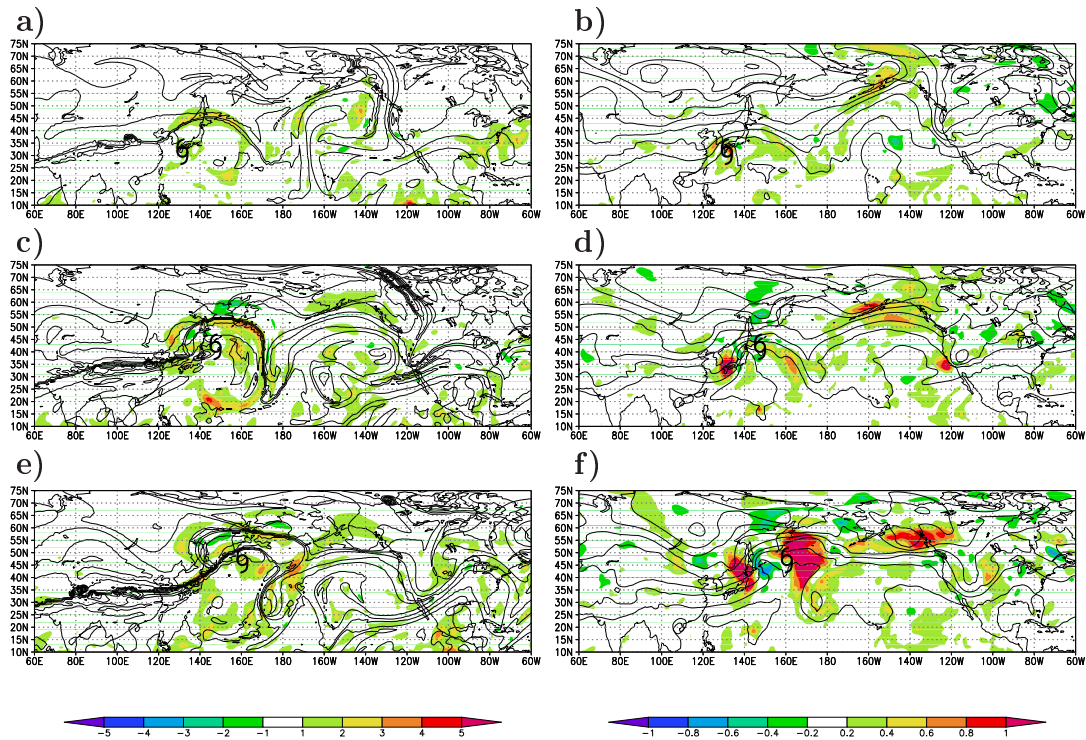


Figure 5.22: As Fig. 5.21 but RMSD differences (shaded) for Sto and $Nosto$ of the horizontal wind (ms^{-1}) at 200 hPa (a, c, e) superposed on the potential temperature on the dynamic tropopause (K, contours) and the temperature (K) at 500 hPa (b, d, f) superposed on the temperature of the control forecast (K, contours) as variable. Forecasts for the same times as in Fig. 5.21.

In the temperature field at 500 hPa (Fig. 5.22 b) a small-scale signal is located at the TC center. This signal is slightly further upstream than the signal in the geopotential (Fig. 5.21 d). The same is observed at ET time (Fig. 5.22 d) and 24 hours (Fig. 5.22 f) thereafter. The signal stays slightly west of the signal seen in the geopotential and grows in scale.

It seems very likely that the perturbations in the upper level wind field are associated with the interaction of Tokage with the midlatitudes. The higher spread caused by the stochastic physics demonstrates the distinct influence of the outflow of Tokage on the midlatitude flow. One cause for the growth of the signal in the wind field of the outflow may

be dynamical impacts of the perturbed temperature and moisture tendencies. Changes in the representation of the convective cores of the TCs, when perturbed by the stochastic physics in the mid-troposphere at previous times, have a direct impact on the variability in the region of the outflow. Alternatively, the ring of higher spread may be caused by uncertainty due to turbulence generated by the outflow when impinging on the midlatitude jet.

The position of the signal in the temperature further eastwards than in the geopotential can be attributed to the typical eastward tilt of the axes of same temperature throughout the troposphere of a developing baroclinic system whereas the troughs and ridges are tilted westwards (Holton, 1992).

The regions in which the stochastic physics strongly enhances the variability in the ensemble are those where the interaction of Tokage with the midlatitudes takes place. It was seen that the higher spread in this region is important for the representation of the uncertainties associated with Tokage's ET (Fig. 5.20).

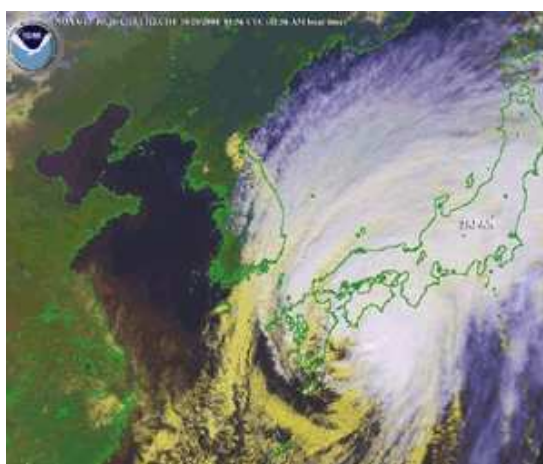


Figure 5.23: Satellite picture (NOAA-17) of Tokage over Japan at 20 October 2004 0156 UTC (National environmental satellite, data, and information Service, <http://www.ncdc.noaa.gov/oa/climate/research/2004/oct/hazards.html>).

In Hovmoeller plots it is seen that at both levels the difference between the RMSD of Nopert/Sto and the RMSD of Nopert/Nosto (the signal) starts to grow later and more slowly compared to in the comparison of Pert and Nopert (Fig. 5.14). The signals seem to propagate with the group velocity of the Rossby-wave-train as well. Clearly, the

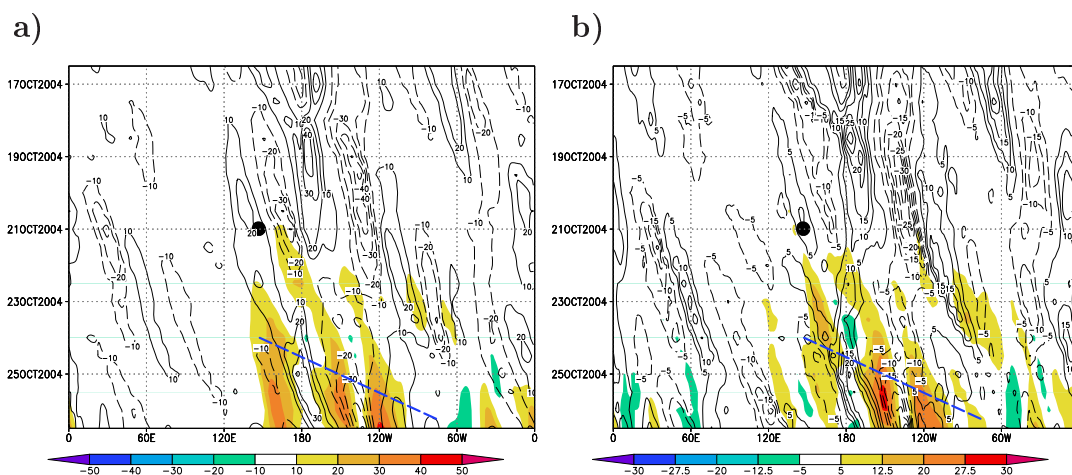


Figure 5.24: Hovmoeller plot of RMSD difference of the geopotential height between the ensemble runs with and without stochastic physics without targeted perturbations on Tokage (shaded, m) and analyzed meridional wind component (contours, ms^{-1}) at 200 hPa (a) and 500 hPa (b) averaged between $30^\circ - 60^\circ$ N. 10-day forecast from FCST1. ET position is marked by a black dot.

easternmost signal is situated too far downstream to be associated with the wave packet originating from Tokage's ET. However, at later forecast times, when all three signals have grown distinctly, parts of the signal due to the ET of Tokage have traveled into the downstream trough at about 120° W and merged with the downstream signal.

The notable growth of the signal due to the stochastic physics in the sphere of influence of the ET is remarkable because the perturbation by the stochastic physics is applied to the parametrized tendencies all over the globe. It demonstrates the important role of the parametrized tendencies during an ET. Uncertainties due to parametrized tendencies seem to have an influence on the reduction of the downstream predictability. However, note that new random numbers are added to the parametrized tendencies every 6 hours (section 3.2.2). Hence, a large signal can disappear quickly with increasing forecast time while somewhere else a signal grows. Hence, the downstream influence of uncertainties in the parameterization is not as clear as that of targeted perturbations. The uncertainties enhanced by the ET yet continue growing beyond a forecast time of 10 days.

5.4.3 Response on Clustering

The EOF and cluster analysis is performed for the Nopert/Sto runs. The EOF patterns (not shown) are very similar to those of Nopert/Nosto (Fig. 5.15 c, d) and their percentage of contribution to the total variability is also similar (Table 5.1). This corresponds with there being no shift of the locations of high variability between Nopert/Sto and Nopert/Nosto in contrast to Pert/Nosto and Nopert/Nosto (section 5.4.2).

Three clusters were obtained in Nopert/Sto, as in Nopert/Nosto. Two of them are very similar to two of the clusters in Nopert/Nosto. The clusters that contribute positively to the shift pattern in Nopert/Sto (Fig. 5.25 c) and Nopert/Nosto (Fig. 5.16 c) develop quickly and show the central pressure of the TC further east than all of the other Nopert clusters. Small differences can be seen only in the depth of their central pressures.

The clusters that contribute positively to the amplitude pattern of Nopert/Sto (Fig. 5.25 a) and Nopert/Nosto (Fig. 5.16 d) both show high amplitude ridges, the TCs are close to the upstream troughs which wrap up cyclonically at the dynamical tropopause. All of the clusters both in Nopert/Sto and Nopert/Nosto that contribute positively to one of the variability patterns show a deep re-intensification of the ET system and their downstream troughs form cut-off lows.

Differences can be seen in the clusters of Nopert/Sto (Fig. 5.25 b) and Nopert/Nosto (Fig. 5.17 c) that contribute negatively to both of the variability patterns. The Nopert/Sto cluster has a more distinct trough-ridge-trough pattern at the dynamical tropopause than the weakest Nopert/Nosto cluster. The rear of the ridge is steeper, possibly due to a stronger outflow of the TC whose central mean sea level pressure is about 5 hPa deeper than for the cluster in Nopert. The downstream trough is deeper also and oriented north-southwards in Figs. 5.25 a, b. The orientation of that downstream trough in the Nopert/Nosto cluster in Fig. 5.17 c was the same but the trough itself was much weaker. The cluster in Fig. 5.25 b shows the weakest ET and re-intensification for Nopert/Sto. However, the weakest Nopert/Sto cluster shows deeper central pressures than the weakest Nopert/Nosto cluster (Fig. 5.17 c) which in turn shows deeper central pressures than the

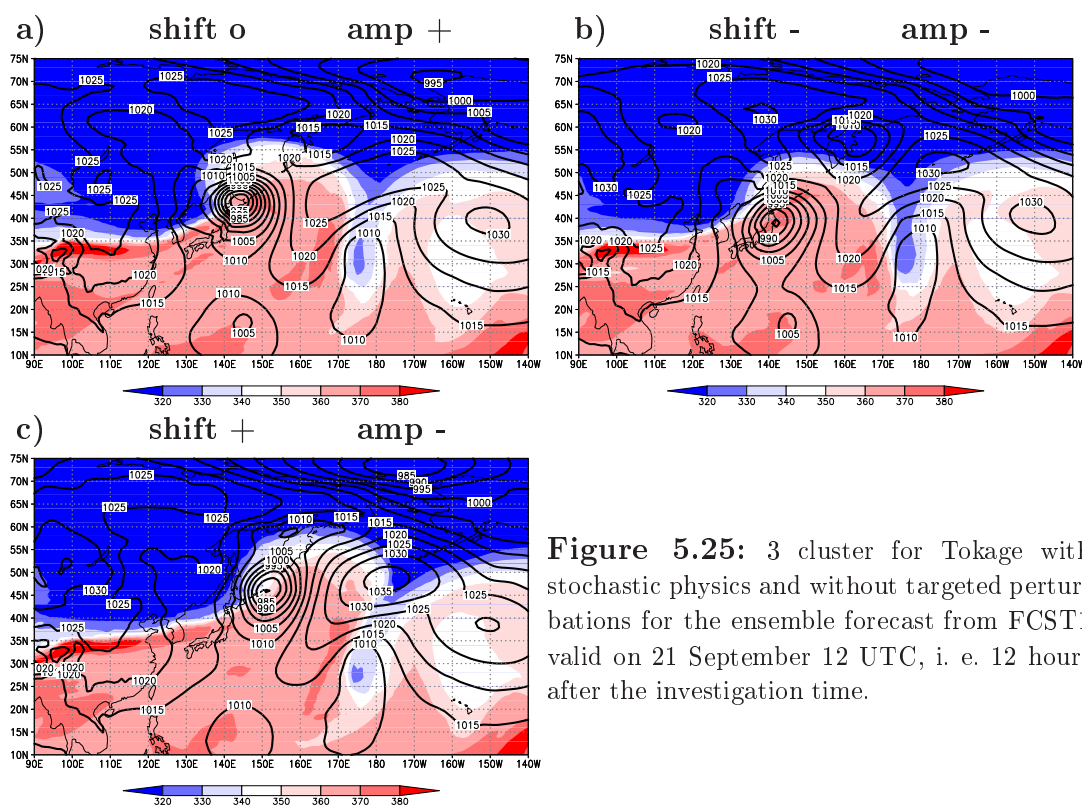


Figure 5.25: 3 cluster for Tokage with stochastic physics and without targeted perturbations for the ensemble forecast from FCST1 valid on 21 September 12 UTC, i. e. 12 hours after the investigation time.

weakest Pert/Nosto clusters (Fig. 5.17 a).

As stated above, the stochastic physics rather seems to deepen the central mean sea level pressures in the ensemble members leading to systems that are even stronger than in Nopert/Nosto. For systems with a very strong re-intensification the stochastic physics might draw the ensemble members closer towards the analysis. In the case of Tokage, however, the central pressure of ensemble members in the runs with the stochastic physics are further from the analysis.

5.5 High resolution experiments

On 1 February 2006 a new configuration was implemented at the ECMWF in the course of which the operational deterministic forecast in the IFS was upgraded from a resolution of T511L60, i. e. truncation after wave number 511 (grid spacing ~ 40 km) and 60 vertical levels, to T799L91 (grid spacing ~ 25 km). The upgrading of the EPS was from T255L40

(grid spacing ~ 80 km) to T399 (grid spacing ~ 50 km) (Untch et al., 2006). To initialize an ensemble forecast with the new EPS the initial perturbations are generated using SVs with higher vertical resolution. They are calculated with T42L62, i. e. with 62 levels in the vertical, instead of T42L40. In the new operational model cycle (30r1) several other important changes were implemented with regard to the assimilation of the grid point humidity and ozone, the coefficient for the ozone calculation, and the wave height information.

This high resolution configuration of the EPS was tested performing the same experiments without stochastic physics as in section 5.3 but with the latest model cycle (31r1). One question of interest is whether the improved representation of orography (over 3700 m) and of the horizontal extension of Japan leads to a better forecast of the weakening of Tokage after its landfall as seen in the analysis.

As the results in section 5.3 were calculated with an earlier model cycle it would not be accurate to use them for a comparison between the low and high resolution. Thus, the forecasts for the Pert/Nosto and Nopert/Nosto experiments had to be rerun with initial perturbations calculated with T42L62 SVs and with the new model cycle. Consequently, the difference between these high and low resolution runs using the same model cycle (31r1) consists only of differences in the horizontal resolution. In the following the new configuration with high horizontal resolution is referred to as “Highres” configuration and the new configuration with the low horizontal resolution is referred to as “Lowres” configuration. In the interest of clarity the earlier model cycle, with which the experiments in sections 5.2, 5.3 and 5.4 have been calculated and which has the ECMWF identifier 29r2, is referred to as L40_29r2. This is the configuration with both low horizontal and vertical resolution.

5.5.1 Effect on tracks

The representation of the recurvature in the high horizontal resolution ensemble track forecast, i. e. Pert/Nosto/Highres, for Tokage from FCST1 (Fig. 5.26 a) is compared with

the low horizontal resolution track forecast, i. e. Pert/Nosto/Lowres (Fig. 5.26 b).

Around the recurvature time many more members lie to the east of the analysis, best track and the deterministic forecast in Lowres (Fig. 5.26 b). The plume of ensemble tracks is shifted slightly to the west in Highres (Fig. 5.26 a) such that the analysis lies closer to the center. Shortly after recurvature the members in Highres are closer together. Only one track lies further east and one further west from the majority at 72 and 84 hours forecast time. The fact that analysis, deterministic forecast and best track lie close together about 1 day after the recurvature, i. e. 1 day prior to ET, indicates rather high predictability at this time. Consequently, it is supposed that the spread in the Lowres runs is a bit too high shortly after recurvature. Shortly before ET time the spread in the track forecasts in Highres is slightly larger than in Lowres. The best track at ET time lies at the edge of the ensemble members with only one member south of it in Lowres while in Highres several members are south and east of the best track at ET time. In this area the analysis, the best track and the deterministic forecast deviate from each other indicating lower predictability. After ET time neither the analyzed track nor the best track are represented by the ensemble.

This comparison suggests that the model runs with the high resolution have a more realistic spread in the TC track forecast as they account for a high predictability with a smaller spread and for a low predictability with a larger spread than Lowres. The positions of the ensemble members closer to the analyzed ET position and, hence, further east at ET time seems to be due to the new model cycle because they are seen in Lowres as well.

In the L62 runs for Pert/Nosto/Lowres a bifurcation in the central pressure values of the ensemble members seems to exist (Fig. 5.27 b). One small group of members follows the filling of Tokage and re-intensifies only weakly or not at all, the members in the other group do not fill but re-intensify deeply. The highest values of mean sea level pressure in the weak group are slightly lower and the minimum values in the strong re-intensifying group are about 10 hPa deeper than in the Pert run with 40 vertical levels (Fig. 5.10 a). The weakening of the small group seems to be due to the landfall of the TC. However, their central pressure values remain too deep. Comparing the L40_29r2 (Fig. 5.10 a)

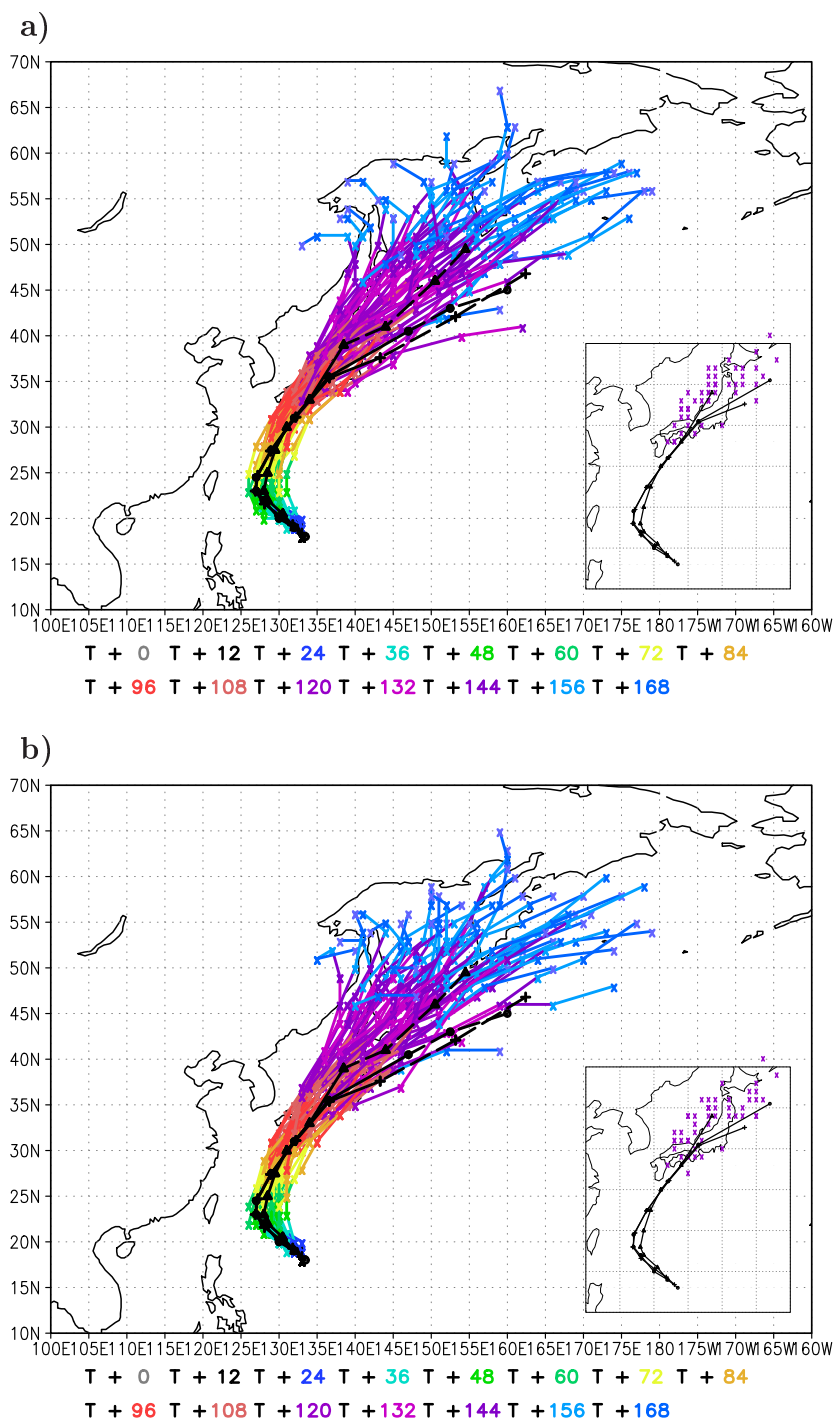


Figure 5.26: Same as Fig. 5.9 a but calculated with the new model cycle (31r1) for a) Pert/Nosto/Highres and b) Pert/Nosto/Lowres.

and L62 (Fig. 5.27 b) runs with low horizontal resolution for Pert from 144 to 168 hours forecast time gives the information that the runs calculated with the new model cycle yield much more spread for longer forecast times.

The splitting of the ensemble members in a group that shows a filling due to landfall combined with a weak or no re-intensification after ET and another group that shows a deep re-intensification can be seen in Highres as well (Fig. 5.27 a). Two of the members among the weak group even reach the high mean sea level pressure values shown by the analysis with 12 and 24 hours delay respectively and slightly more members than in Lowres (Fig. 5.27 b) do not re-intensify at all. One of the members that re-intensify deeply reaches a value of 926 hPa at 144 hours forecast time. The spread in the mean sea level pressure in Highres is larger from ET time on.

The high resolution is capable of representing the weakening seen in the analysis with a delay. Furthermore, the Highres runs yield an improvement of the ensemble forecast in that more members do not re-intensify or do only re-intensify weakly and hence describe the behavior of the analysis even though they show mostly deeper pressure values. Finally, the higher resolution leads to higher spread for long forecast intervals improving the repeatedly mentioned lack of spread after about 5 days forecast time. However, even in the runs with higher horizontal and vertical resolution the abrupt filling of Tokage is not forecast by the ensemble.

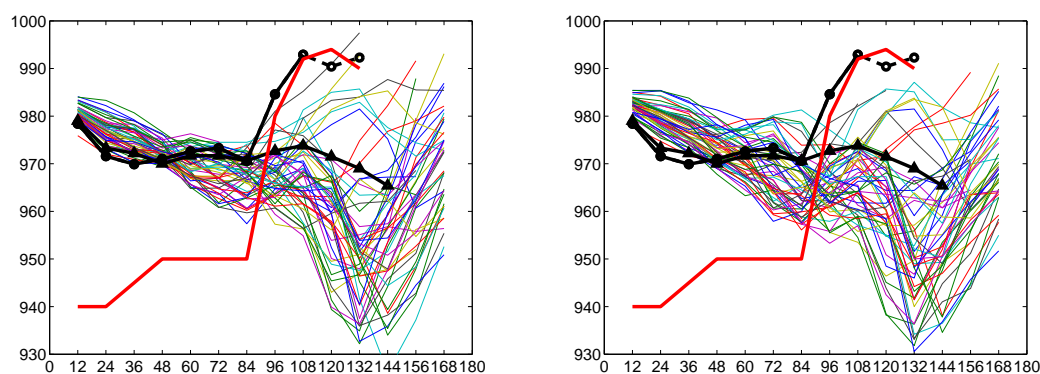


Figure 5.27: Same as Fig. 5.10 a but calculated with the new model cycle (31r1) for a) Pert/Nosto/Highres and b) Pert/Nosto/Lowres.

5.5.2 Effect on the amount of spread

The representation of the spread has been compared for Pert/Highres, Nopert/Highres, Pert/Lowres and Nopert/Lowres (Fig. 5.28). In this case the black lines in Pert/Highres (Fig. 5.28 a) represent the areas of well represented spread in Pert/Lowres (Fig. 5.28 c) and those in Nopert/Highres (Fig. 5.28 b) represent the areas of well represented spread in Nopert/Lowres (Fig. 5.28 d).

In the Pert and Nopert Lowres results with the L62 resolution (Fig. 5.28 c, d) the region of nearly zero values RMSD – RMSE downstream of the ET is broader than in the run with the L40_29r2 resolution and the earlier model cycle (Fig. 5.11 a, b). The two plumes have merged. The region in which the spread is represented correctly expands from 150° E to about 150° W without interruption and broadens with forecast time.

Investigation of spaghetti plots of the 200 hPa geopotential height (not shown) yields the information that the spread in the trough downstream of Tokage is much higher than in the run with low vertical resolution. More members that have high amplitude ridges and downstream troughs can be seen. In the region where the flow becomes more zonal again – downstream of the downstream trough – more members are close to the analysis giving a lower RMSE.

The areas in which the spread is overrepresented, however, have increased as well. As in the L40_29r2 runs there are some differences between Pert and Nopert Lowres in the broadness of the two plumes downstream of the ET. In Pert/Lowres broader regions of well represented spread can be seen than in Nopert/Lowres and the regions where the spread is underrepresented strongly, for example on 23 October 00 UTC at about 170° E and on 24 October 00 UTC at about 140° W, show weaker values in Pert/Lowres. However, the spread is overrepresented in larger regions in Pert/Lowres than in Nopert/Lowres. This was not seen in the runs with the older model cycle (section 5.3).

In Pert/Highres (Fig. 5.28 a) the positive values on 22 October 00 UTC in the region of the trough downstream of the ET (at about 170° W) are smaller than in Pert/Lowres (Fig. 5.28 c) and in Nopert/Highres the values are nearly zero (Fig. 5.28 b) indicating a

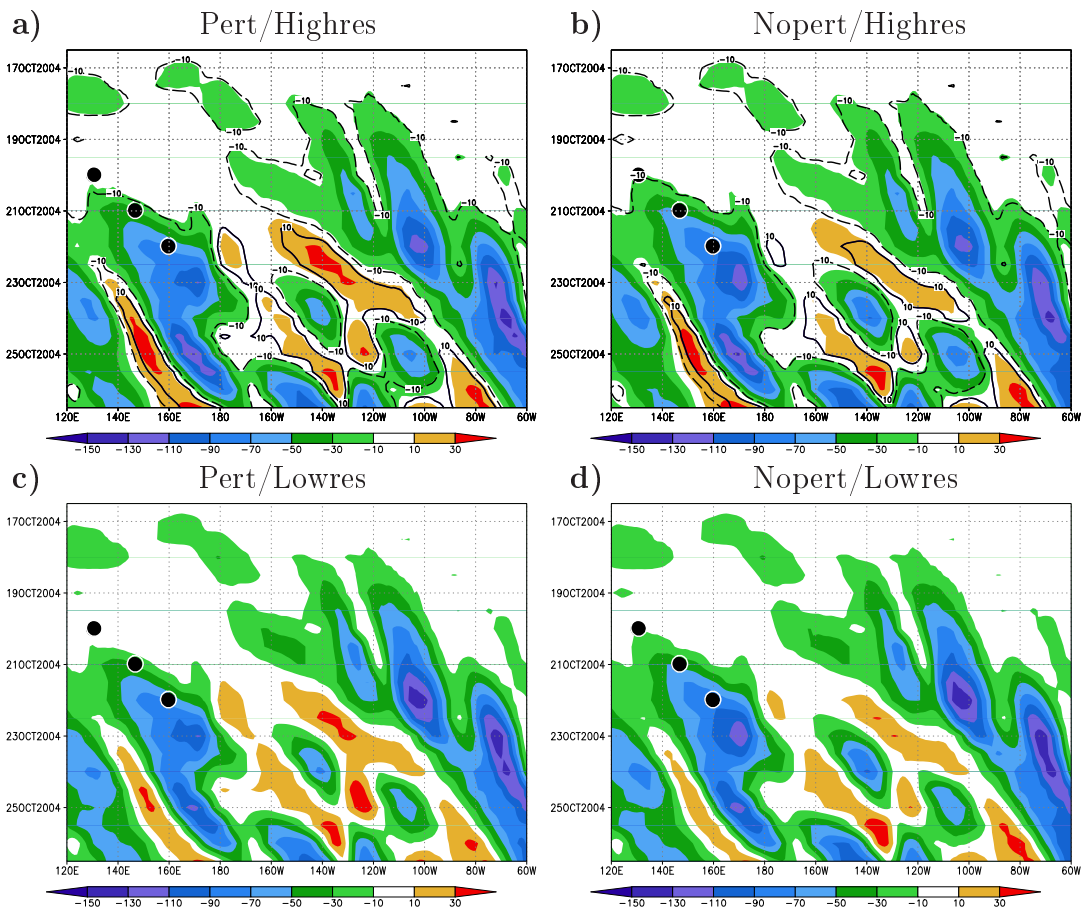


Figure 5.28: As Fig. 5.11 but calculated with the new model cycle (31r1) for (a, b) Highres and (c, d) Lowres. Left: runs with targeted SVs, right: runs without targeted SVs on Tokage. The isolines that mark the regions of well represented spread in (c) are marked by black lines (-10: dashed, 10: solid) in (a), those that mark the regions of well represented spread in (d) are marked in (b).

more realistic spread associated with the ET event. This confirms the results from the investigation of the tracks (section 5.5.1). Investigating the spaghetti plots (not shown) a better grouping of the members in this region can be noticed. The main group lies around the analysis that shows only a weak trough and a smaller one describes a deep trough or a cut-off low. Also before ET the spread is represented better by both Pert and Nopert Highres in many areas. However, from ET time until 2 days after ET the spread in the plume further downstream of the ET event starting from about 180° is overrepresented by the high resolution runs.

It can be concluded that the high resolution yields a better representation of the uncer-

tainties around the ET propagating downstream. The Highres ensemble forecast reduces, with few exceptions, the overrepresentation of the uncertainties in the ridge-trough system directly downstream of the ET event. However, further downstream the spread is still overrepresented.

5.5.3 Response on Clustering

The influence of the high horizontal resolution on the synoptic development is investigated with the analysis method described in section 4.3.

Four clusters were found for Pert and 3 for Nopert with both Highres and Lowres. An overview over the differences between the runs with the old and the new cycle is given by presenting the relative location of the trough-ridge-trough pattern at the tropopause versus the position of the TC in terms of mean sea level pressure in the different clusters (Fig. 5.29). The cluster means of the 350 K isentrope (solid) and the 995 hPa isobar (dashed) are shown in the same color within each cluster for the L40_29r2 runs (Fig. 5.29, left) and the L62_Lowres runs (Fig. 5.29, right), for Pert (Fig. 5.29, top) and Nopert (Fig. 5.29, bottom). Furthermore, the same color has been chosen for clusters with the same contributions to the variability patterns as given in Tables 5.1 and 5.2.

For the L62_Lowres runs the shift pattern describes much more of the total variability than the amplitude pattern for Pert and Nopert (Table 5.2) in contrast to the L40_29r2 runs where the amplitude pattern describes the highest percentage of variability in Pert (Table 5.1). This difference becomes manifest in more variability in the representations of the speed of the ET development and the inclination of the trough-ridge-trough pattern for Pert/Nosto in the L62_Lowres runs (Fig. 5.29 b). Three of the four ridges show their crests at about the same latitudinal position varying only in their inclination to the east or to the west. Smaller distances of the 995 hPa isobars to the upstream troughs are associated with higher amplitudes of the ridges in the clusters. In fact the relative location of the TCs to the upstream troughs in the clusters (Fig. 5.29 b) look like a time series of an ET event beginning with red, continuing over green and blue and ending with black.

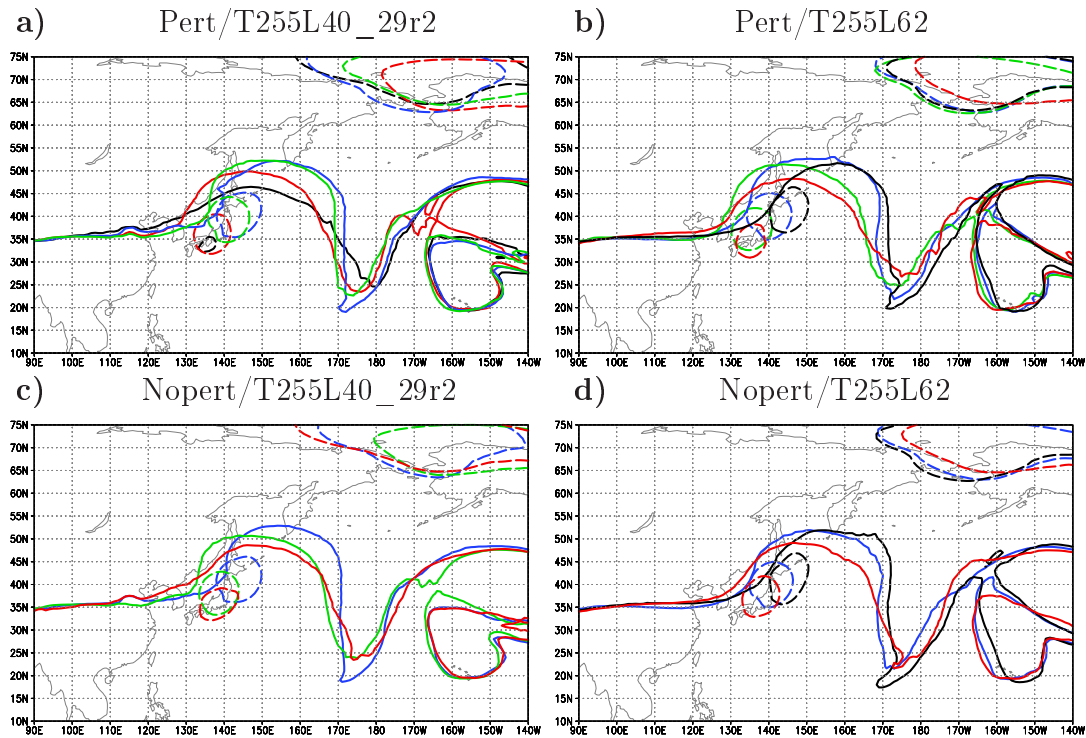


Figure 5.29: Spaghetti plots of the cluster means of the 350 K isentrope and the 995 hPa mean sea level pressure isobar. Ensemble forecast for Tokage with the old model cycle, i. e. T255L40_29r2 resolution, a) with and c) without perturbations and with the new model cycle, i. e. T255L62 resolution, b) with and d) without perturbations from FCST1 valid on 21 October 12 UTC, i. e. 12 hours after the investigation time. Same colors indicate same contribution to the variability patterns (compare Table 5.2).

The L40_29r2 runs for Pert show more variability in the amplitude of the trough-ridge-trough pattern (Fig. 5.29 a) leading to different intensities of the TCs during ET and to different strengths of re-intensification (see section 5.3 and Table 5.2). For Pert the black cluster in L62_Lowres (Fig. 5.29 b) which has the same signs of contributions to the variability patterns as the black cluster in L40_29r2 (Fig. 5.29 a), shows the quickest ET development. In L40_29r2 the black cluster shows a decay, however. The different developments of the black cluster in Pert for L62_Lowres and L40_29r2 is caused by the different strong contribution to the variability patterns. In L40_29r2 the black cluster contributes with 18.4 % to the amplitude and only with 11.2 % to the shift pattern. Therefore, the negative contribution to the amplitude pattern has a strong effect in this cluster and the TC decays. In 62_Lowres, however, the black cluster contributes with 22.4 % to the shift and only with 9.4 % to the amplitude pattern. Consequently, the positive

contribution to the shift pattern has a strong effect and the ET system moves quickly to the east. Furthermore, in Fig. 5.29 b it is seen that all of the clusters, and, consequently, also the ensemble mean, have quite high amplitude ridges. Note that in deducing the ET development in one cluster from the EOFs it is important to keep in mind the percentage contribution to the shift and amplitude pattern.

As described in section 5.3 the weakest (black) cluster cannot be found in Nopert/Nosto for L40_29r2 (Fig. 5.29 c). The development of the ET event in Nopert for L62_Lowres resembles a time series as well but the cluster that contributes negatively to both variability patterns (red in Fig. 5.29 d) is a combination of the two clusters that contribute negatively to the shift pattern in Pert (red and green in Fig. 5.29 b). As in Pert for L62_Lowres the black cluster shows the quickest ET development and is not present in Nopert for the L40_29r2 runs.

The differences in the old and the new model cycle with respect to the cluster formation are such that with the old model cycle the ensemble forecast tends to form more clusters that are weaker while with the new model cycle the forecast puts more emphasis on the clusters that show the ET system moving eastwards more quickly. In each of the runs, the cluster that shows the quickest development represents the position of Tokage best even though its central pressure is too strong and the amplitude of the ridge is too high. Note that the differences in the runs with the T255L40_29r2 and the T255L62 resolution cannot be attributed to the differences in vertical resolution alone as the old and the new model cycle differ in more than the resolution.

In the L62_Highres runs the clusters look quite similar to the clusters in L62_Lowres both for Pert and Nopert. Differences can be seen mainly in the central pressures shortly after their landfall, partly in their re-intensification and in the number of members that contribute to the different clusters (Table 5.2).

As the focus of the investigation of the high resolution ensemble forecast is on the landfall, the 4 Pert/Nosto/Highres clusters and 2 of the Pert/Nosto/Lowres clusters are shown in Figs. 5.30 and 5.31 for times corresponding to the earliest available time after their landfalls. These times are different for the different clusters according to the respective

speed of their ET development. Additionally, the time of the analyzed landfall of Tokage, i. e. 20 October 12 UTC is shown (Fig. 5.31 c). Firstly, the clusters that show a quick development of the ET, i. e. that have a positive contribution to the shift pattern (black and blue in Fig. 5.29 b, d) are compared for Pert/Lowres and Pert/Highres.

The first time after landfall is 20 October 12 UTC (Fig. 5.30), as in the analysis. The TCs in Highres (Fig. 5.30, left) weaken slightly more in terms of their central pressure values than in Lowres (Fig. 5.30, right). However, comparing them with the analysis (Fig. 5.31 c) it is obvious that the TCs are still much too strong. Furthermore, 12 hours later only the cluster that contributes negatively to the amplitude pattern (Fig. 5.30 c) re-intensifies moderately and all the others in Fig. 5.30 show a strong re-intensification after ET while the system in the analysis does not re-intensify (Fig. 4.2 c).

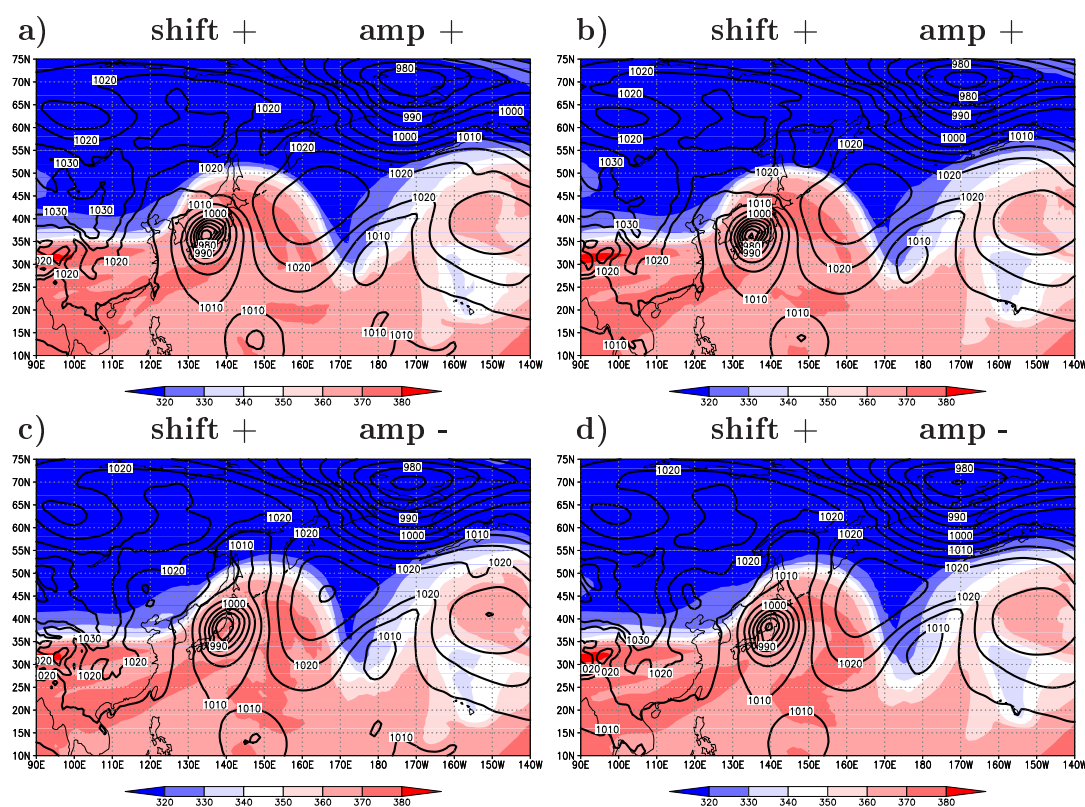


Figure 5.30: 2 of 4 clusters for Tokage that contribute positively to the shift pattern for Pert/Highres (a, c) and for Pert/Lowres (b, d) for the ensemble forecast from FCST1 valid on 20 October 12 UTC, i. e. 12 hours before the analyzed ET time.

For the clusters that contribute negatively to the shift pattern only the Pert/Highres

clusters are shown (Fig. 5.31) as the Pert/Lowres clusters that contribute negatively to that pattern are very similar to them. One of them (Fig. 5.31 b) made landfall at the ET time in the analysis, in the other one (Fig. 5.31 a) the landfall was just a bit earlier. The mean sea level pressure in the cluster with the positive contribution to the amplitude pattern (Fig. 5.31 a) is too deep and the TC has moved too far to the north. It is close to the upstream trough and re-intensifies strongly 12 hours later. In the cluster with the negative contribution to the amplitude pattern (Fig. 5.31 b) the weakening of the TC due to landfall and its location is represented best but remember that the time shown is 12 hours after the analyzed time of Tokage's landfall. After the time shown in Fig. 5.31 b) the TC approaches the upstream trough and re-intensifies moderately while the analyzed Tokage moves to the west, stays away from the upstream trough and weakens (Fig. 4.2 c).

The Nopert runs for Highres (not shown) look rather similar to the Nopert/Lowers runs in terms of the shape of the tropopause and the location of the 955 hPa isobar associated with Tokage (Fig. 5.29 d). In contrast to the weaker central pressures in the Pert/Highres compared with the Pert/Lowers runs, the central pressures in the clusters calculated with Nopert/Highres are slightly deeper than those in the clusters calculated with Nopert/Lowres. Consequently, the additional targeted perturbations make a bigger difference in the Highres than in the Lowres runs.

It can be concluded that in the high resolution runs the weakening of Tokage after landfall is slightly better represented because in two of the Highres clusters the central pressure directly after landfall is weaker than in Lowres. In Highres the range of possible developments is larger. Although in one of the clusters the TC weakens almost to the values of the analyzed central pressure with 12 hours delay, the analysis is not well represented as all of the clusters show a re-intensification. The non or weakly re-intensifying members seen in section 5.5.1 have been grouped in different clusters because their time of re-intensification is different.

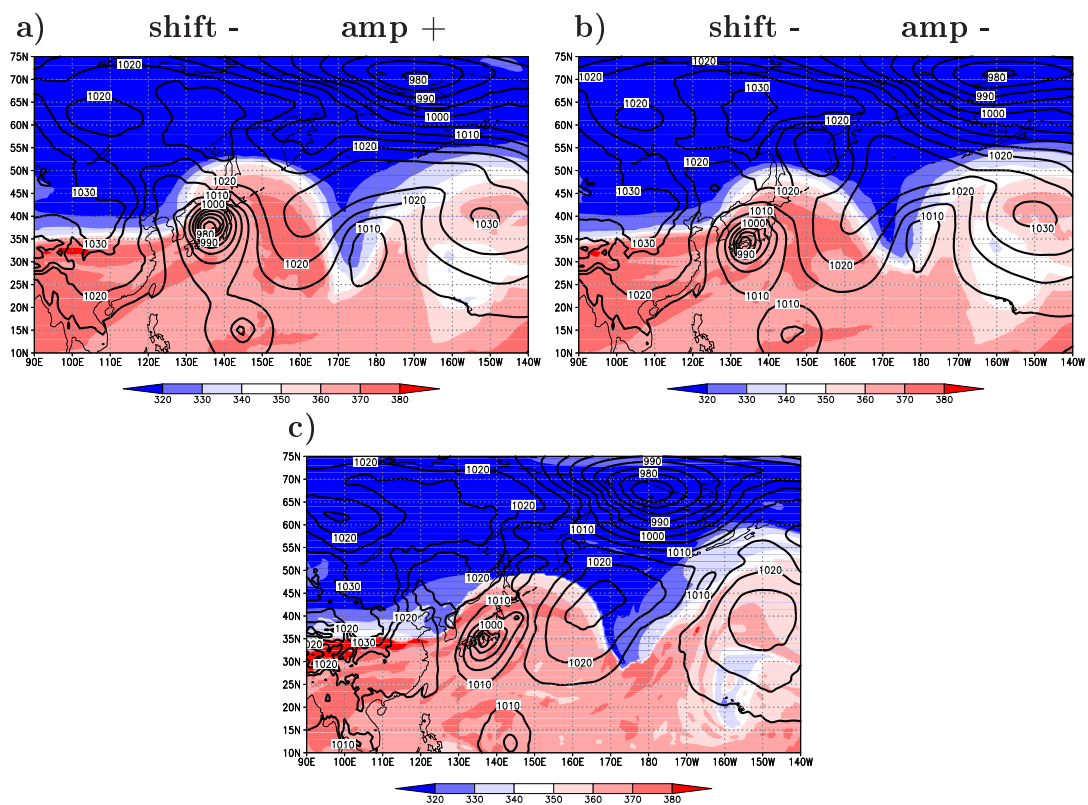


Figure 5.31: 2 of 4 clusters for Tokage that contribute negatively to the shift pattern for Pert/Highres (a, b) for the ensemble forecast from FCST1 valid on 21 September 12 UTC, i. e. at the analyzed ET time. c) analysis at 20 October 12 UTC, i. e. time of Tokage's landfall.

6 Conclusions

The variability in the ECMWF EPS system during the ET of five TCs has been investigated. The TCs covered a wide range of intensity on the Saffir-Simpson scale. Examples of strong and weak events in both the North Atlantic and the western North Pacific were investigated.

All five cases exhibited a characteristic trough-ridge-trough pattern in the midlatitudes on the dynamic tropopause, consisting of the trough that interacts with the respective TC, a ridge directly downstream and a second trough downstream of the ridge. It became evident that the ET events were associated with high uncertainty in the EPS.

The standard deviation, one of the conventional measures of spread, was used to quantify the uncertainty on 200 and 500 hPa. The regions of highest standard deviation in the major TC cases could be found from 18 to 60 h after ET in a trough upstream of the ET, directly associated with the ET and in a downstream trough. As the strong increase of standard deviation was always shortly after completion of the ET irrespective of the forecast interval prior to it, evidence is given that the uncertainty is tied to the ET. In the weak ET cases the highest uncertainties could be found slightly later after ET than for the strong cases, at the location where their remnants merged with the respective midlatitude system. While naturally, the uncertainty in the ensemble grows for longer forecast times, several days after ET the high values of standard deviation associated with the ET event decrease to more normal values compared with regions that are not influenced by the ET. This decrease further demonstrates the connection between the high variability in the ensemble and the ET event.

Uncertainties in the forecast could be associated both with the recurvature and with

the ET itself. The forecast of recurvature is very sensitive to small errors in the initial conditions. A small forecast error can result in the tropical cyclone not moving into the region relative to the upstream trough that is favorable for re-intensification. Initializing the forecast at times, when the relative location of the respective upstream trough to the recurving TC, i. e. the phasing, was better defined, yielded much lower uncertainty for the same forecast lead time. The connection of the increased variability among ensemble members to the respective ET is reduced but still a comparatively high uncertainty associated with the ET event remains.

With the aid of an analysis method that consists of the calculation of EOFs and the clustering of the principal components at times shortly after ET, it was found that the EOFs in all five investigated cases showed robust structures associated with the ETs. The variability in the EPS revealed by them is related to physical scenarios. The uncertainty was based mainly on two variability patterns: one pattern, that describes an east-west shift of the trough-ridge-trough pattern, and another one, that describes the amplitude of the trough-ridge-trough pattern. Although the maxima of variability associated with ET decreased with decreasing forecast time, the variability patterns remained connected to the synoptic features of the ET.

By the aid of a fuzzy cluster analysis ensemble forecasts were grouped into different clusters according to similar forecast scenarios associated with the ETs. It could be seen that similar signs of contribution of the individual clusters to the variability patterns in all five cases led to similar developments of the ETs. A higher amplitude of the trough-ridge-trough pattern in one cluster would imply a deeper re-intensification of the system and a lower amplitude would imply a weaker re-intensification than in the other clusters. An eastward shift of the trough-ridge-trough pattern implies a faster motion and development of the ET system, whereas a westward shift implies a slower motion and development than in the other clusters. These links have the potential to give the forecaster a hint on the future development of the system from examining the pattern of the dynamic tropopause during ET.

With the aid of the analysis method a range of very different possible atmospheric

developments in the regions of high variability were extracted. Through the clustering, probabilities could be assigned to each of these developments based on the number of members contained in each cluster. Furthermore, indications of atmospheric evolutions associated with the ETs that are not probable but possible are given. Hence, the large number of ensemble members, showing very different developments during ET, is reduced to a small for a forecaster easy managable amount of ET scenarios that are provided with a probability of the ET event occurring.

In most of the forecasts from FCST2 fewer clusters were found. These were consequently larger than those in FCST1. The fact that the largest clusters were most similar to the analysis is an indication of higher predictability. Clusters that showed a high deviation from the ensemble mean were no longer found. These results supports the hypothesis of Harr et al. (2007) that a lower uncertainty is associated with a decrease in the number of clusters.

The importance of ensemble prediction was confirmed using cases in which the deterministic forecasts were inaccurate. In one of the cases a low probability was assigned to the erroneous deterministic forecast and in another one an early indication was given of the development that could be found in the analysis but was not shown in the deterministic forecast.

For the purpose of making available the analysis method explained and used in this study consisting of EOF and fuzzy cluster analysis for operational forecast it would be desirable to find an objective measure of the correct number of clusters.

In the second part of the study EPS experiments for one specific case were carried out. The aim of the experiments was to compare the influence of targeted perturbations, stochastic physics and higher resolution on track and intensity forecast, representation of overall spread during an ET, downstream propagation of uncertainties introduced by an ET event and grouping of the ensemble members in the regions of uncertainties.

The case of Tokage was chosen because this tropical cyclone seemed to have the most active influence on the formation of the characteristic trough-ridge-trough pattern that is

inherent in all the investigated cases. Furthermore, the track and intensity forecasts for the recurvature and the ET of Tokage were barely captured by the ECMWF ensemble and the weakening after the TC's landfall on Japan was underestimated by all the ensemble members.

For the purpose of rerunning new ensemble forecasts the SVs were recalculated to be consistent with the model cycle used for the experiments. The recalculation of the initial singular vectors targeted for the optimization region of Tokage included the changes implemented in September 2004 in that the calculation of the optimization regions was extended to 50° latitude. The horizontal and vertical structures, the distribution of energy and the coincidence with a measure of baroclinic instability (the Eady index) of these targeted SVs were investigated and compared to well known features of extratropical SVs.

Subtropical SVs have different properties to extratropical SVs. Their different structures, smaller horizontal and vertical tilts and more equalized ratio of available potential and kinetic energy describe rather barotropic and inertial instabilities associated with the TC. These subtropical SVs have maximum amplitude at higher levels in the atmosphere, consistent with the higher steering flow influencing a TC. Extratropical SVs are located at lower levels and in regions upstream of baroclinic instability. Their initial total energy consists almost only of available potential energy and they are tilted strongly against the shear, consistent with well known characteristics.

The EPS experiments showed that sufficient ensemble spread in the track and improved spread in the intensity forecast depends strongly on the additional perturbations targeted on Tokage. Without these, the track spread in the forecasts, especially that around the recurvature and ET of Tokage, was underestimated and the analysis was not encompassed by the ensemble members. However, the higher resolution in addition to the targeted SVs yields a correction of the marginal overestimation of the spread shortly before ET.

In general, the targeted SVs are expected to be appropriate to perturb larger scale features associated with the track forecast. The stochastic physics is needed to perturb small scale processes, such as convection in the inner core of the TC, that determine the intensity (Puri et al., 2001). In our case, however, the stochastic physics mainly yields suf-

ficient spread in the intensity for the forecast times before ET. At ET time and thereafter, the targeted perturbations were responsible for weakening while the stochastic physics led to more deepening than seen in runs with neither targeted perturbations nor stochastic physics. For other investigated cases in the literature (e. g. Puri et al. (2001)) the stochastic physics was necessary to include the TCs deep central pressures in the ensemble because these are difficult to represent due the ensembles coarse resolution.

Clearly, the weakening, which was probably associated with the landfall due to Japan's orography in the investigated case, is a too high challenge for parameterization schemes. Other case studies of the representation of the intensity in the ensemble during the landfall of a Typhoon on Japan or other small islands might yield insightful comparisons.

The new high resolution model cycle with targeted perturbations shows the best spread in track and intensity forecast. More members that show a quick movement of Tokage are reflected which is, however, rather due to other innovations than to the higher horizontal resolution. Even with the new model cycle with high resolution and with the targeted perturbations on Tokage the ensemble forecast of the intensity does not encompass the analysis for a whole day.

The overall spread in terms of the geopotential is depicted best by the new model cycle with the high horizontal resolution even without targeted perturbations. The spread is represented correctly in more regions than with the low horizontal resolution in the sense that the root-mean-squared-error is equal to the root-mean-squared difference from the control forecast. The targeted SVs depict the spread correctly in a region constrained around the ET and propagating downstream. The effect of the stochastic physics is weaker but can be seen all over the forecast area. It grows stronger at later times.

The impact of the SVs targeted on Tokage propagates downstream with the group velocity of a Rossby-wave-train that has been excited by the interaction of Tokage with the midlatitudes. The amplitude of the wave packet determines the transport of wave energy which can trigger cyclogenesis far away from the ET event. At 20° per day the group velocity is slightly smaller than that found by Szunyogh et al. (2002). The growth and downstream propagation of the impact of the targeted SVs on Tokage yields a good

measure of the rapidity and the extent of the downstream propagation of errors growing in association with ET. The results indicate that an ET event can reduce the predictability over an entire ocean basin.

The strong growth of the effect due to the stochastic physics in the vicinity of the ET and the partly downstream propagation of this effect demonstrates that there is a distinct reduction of predictability due to parametrized processes associated with the ET. Stochastic physics can have an influence on the downstream predictability through perturbations caused by Tokage's outflow impinging on the midlatitude jet. The uncertainties due to parametrized processes continue growing beyond the medium range.

The use of the analysis method of the first part showed that 4 clusters were obtained only in the runs with targeted perturbations. In any other case, i. e. with stochastic physics only or with high resolution only, 3 clusters were found. Only the targeted perturbations with the old model cycle yield one cluster that shows no ET and, hence, is weaker than the analysis. The reason for the decay of Tokage in this cluster, however, was not the landfall as in the analysis, but that the TC was too far south of the midlatitude baroclinic zone. Even with the higher resolution and with targeted perturbations on Tokage only one cluster showed the weakening due to the landfall. However, in this cluster the ex-TC re-intensified as well as in all the other clusters. This is in contradiction to the analysis.

Apparently, the EPS must have had serious problems in predicting the weakening of Typhoon Tokage after landfall. The weakening found through the additional targeted perturbations seems to play an essential role in improving the forecast. However, the new horizontal resolution of the EPS which is about 60 km with 62 levels is clearly still not high enough for the comparatively small island of Japan with its fine orographical structures.

Because the targeted SVs on Tokage have the biggest benefits in weakening the central pressures in the ensemble both in the old low resolution and in the new high resolution model cycle it is expected that a further increase of the resolution, especially the horizontal resolution, with which the SVs are calculated would yield better intensity forecasts. Buizza et al. (1998) found that an increase in horizontal scale from T42 to T63 would give an extra 25 % growth of disturbances. Because of the high computational expense that an

increase of the resolution of SVs would involve it was decided at the ECMWF to first include more physics in the calculation of the tangent linear and the adjoint model to improve the calculation of the parametrized processes.

In this study the influence of targeted perturbations, stochastic physics and higher resolution on the representation of ET in ensemble forecast was done for the first time. Further experiments examining different ET cases are needed to investigate these influences on the representation of the uncertainty. It is important to test if the results found here can be carried forward to other cases. This applies in particular to cases of weaker ETs. Testing the representation of model uncertainties by a new stochastic physics scheme which has been developed recently at the ECMWF are of interest as well. Further experiments would allow a better interpretation of the impact that an ET event has on the decrease of predictability. It would be desirable to distinguish the influence due to the tropical cyclone from uncertainties which would have developed without the TCs influence in the midlatitudes.

Bibliography

- Badger, J. and B. J. Hoskins (2000). Simple initial value problems and mechanisms for baroclinic growth. *J. Atmos. Sci.* *58*, 38–49.
- Barkmeijer, J., R. Buizza and T. N. Palmer (1999). 3D-Var hessian singular vectors and their potential use in the ECMWF ensemble prediction system. *Q. J. R. Meteorol. Soc.* *125*, 2333–2351.
- Barkmeijer, J., R. Buizza, T. N. Palmer and J.-F. Mahfouf (2001). Tropical singular vectors computed with linearized diabatic physics. *Q. J. R. Meteorol. Soc.* *127*, 685–708.
- Björnsson, H. and S. A. Venegas (1997). A manual for EOF and SVD analyses of climate data. Techn. Ber., Department of Atmospheric and Oceanic Sciences and Centre for Climate and Global Change Research, McGill University.
- Bosart, L. F. and G. M. Lackmann (1995). Postlandfall tropical cyclone reintensification in a weakly baroclinic environment: A case study of Hurricane David (September 1979). *Mon. Wea. Rev.* *123*, 3268–3291.
- Buizza, R. (2004). Chaos and weather prediction. *European Centre for Medium Range Weather Forecasts - Research Department* .
- Buizza, R., P. L. Houtekamer, Z. Thoth, G. Pellerin, M. Wei and Y. Zhu (2004). A comparison of the ECMWF, MSC, and NCEP global ensemble prediction systems. *Mon. Wea. Rev.* *133*, 1076–1097.

- Buizza, R., M. Miller and T. N. Palmer (1999). Stochastic representation of model uncertainties in the ecmwf ensemble prediction system. *Q. J. R. Meteorol. Soc.* *125*, 2887–2908.
- Buizza, R. and T. N. Palmer (1995). The singular-vector structure of the atmospheric global circulation. *J. Atmos. Sci.* *52*, 1434–1456.
- Buizza, R., T. Petroliaigis, T. N. Palmer, J. Barkmeijer, M. Hamrud, A. Hollingsworth, A. Simmons and N. Wedi (1998). Impact of model resolution and ensemble size on the performance of an ensemble prediction system. *Q. J. R. Meteorol. Soc.* *124*, 1935–1960.
- Buizza, R., D. S. Richardson and T. N. Palmer (2001). The new 80-km high-resolution ECMWF EPS. *ECMWF Newsletter No. 90*, 2–9.
- Cheng, X. and J. M. Wallace (1991). Cluster analysis of the northern hemisphere winter-time 500-hpa height field: Spatial patterns. *J. Atmos. Sci.* *50*, 2674–2696.
- Coutinho, M. M., B. J. Hoskins and R. Buizza (2004). The influence of physical processes on extratropical singular vectors. *J. Atmos. Sci.* *61*, 195–209.
- Davis, C. A. and K. A. Emanuel (1991). Potential vorticity diagnostics of cyclogenesis. *Mon. Wea. Rev.* *119*, 1929–1953.
- Davis, C. A., S. C. Jones and M. Riemer (2007). Hurricane vortex dynamics during Atlantic extratropical transition. *submitted to J. Atmos. Sci.*, revised.
- Eady, E. T. (1949). Long waves and cyclone waves. *Tellus* *1*, 33–52.
- Ehrendorfer, M. (1994). The Liouville equation and its potential usefulness for the prediction of forecasts skill. part i: Theory. *Mon. Wea. Rev.* *122*, 703–713.
- Ehrendorfer, M., R. M. Errico and K. D. Raeder (1999). Singular-vector perturbation growth in a primitive equation model with moist physics. *J. Atmos. Sci.* *56*, 1627–1648.
- Epstein, E. S. (1969). Stochastic-dynamic prediction. *Tellus* *21*, 739–759.

- Evans, J. L. and R. E. Hart (2003). Objective indicators of the life cycle evolution of extratropical transition for atlantic tropical cyclones. *Mon. Wea. Rev.* *131*, 909–925.
- Farrell, B. F. (1982). The initial growth of disturbances in a baroclinic flow. *J. Atmos. Sci.* *39*, 1663–1686.
- Franklin, J. L. (2006). Tropical cyclone report Hurricane Philippe 17-23 september 2005. National Hurricane Center .
- Golub, G. and C. van Loan (1996). *Matrix computations*. 3rd edition, The Johns Hopkins University Press Ltd, London.
- Harr, P. A., D. Anwender and S. C. Jones (2007). Predictability associated with the downstream impacts of the extratropical transition of tropical cyclones: Methodology and a case study of Typhoon Nabi (2005). *Mon. Wea. Rev.* , submitted.
- Harr, P. A. and R. L. Elsberry (2000). Extratropical transition of tropical cyclones over the western north pacific. Part II: The impact of midlatitude circulation characteristics. *Mon. Wea. Rev.* *128*, 2634–2653.
- Hartmann, D. L., R. Buizza and T. N. Palmer (1995). Singular vectors: The effect of spatial scale on linear growth of disturbances. *J. Atmos. Sci.* *52*, 3885–3894.
- Henderson, J. M., G. M. Lackmann and J. R. Gyakum (1999). An analysis of Hurricane Opal’s forecast track errors using quasigeostrophic potential vorticity inversion *127*, 292–307.
- Hirschberg, P. A. and J. M. Fritsch (1991). Tropopause undulations and the development of extratropical cyclones. Part I: Overview and observations from a cyclone event. *Mon. Wea. Rev.* *119*, 496–517.
- Holton, J. R. (1992). *An introduction to dynamic meteorology*. Third Edition, Academic Press.
- Hoskins, B. J., R. Buizza and J. Badger (2000). The nature of singular vector growth and structur. *Q. J. R. Meteorol. Soc.* *126*, 1565–1580.

- Hoskins, B. J. and M. M. Coutinho (2005). Moist singular vectors and the predictability of some high impact european cyclones. *Q. J. R. Meteorol. Soc.* 131, 581–601.
- Hoskins, B. J., M. E. McIntyre and A. W. Robertson (1985). On the use and significance of isentropic potential vorticity maps. *Q. J. R. Meteorol. Soc.* 111, 877–946.
- Hoskins, B. J. and P. J. Valdes (1990). On the existence of storm-tracks. *J. Atmos. Sci.* 47, 1854–1864.
- Houtekamer, P. L., L. Lefaiivre, J. Derome, H. Ritchie and H. Mitchell (1996). A system simulation approach to ensemble prediction. *Mon. Wea. Rev.* 124, 1225–1242.
- Hovmöller, E. (1949). The trough-and-ridge diagram. *Tellus* 1, 62–66.
- JMA (2006). Japan meteorological Agency. <http://www.jma.go.jp/jma/indexe.html> .
- Jones, S. C., P. A. Harr, J. Abraham, L. F. Bosart, P. J. Bowyer, J. L. Evans, D. E. Hanley, B. N. Hanstrum, R. E. Hart, F. Lalaurette, M. R. Sinclair, R. K. Smith and C. Thorncroft (2003). The extratropical transition of tropical cyclones: Forecast challenges, current understanding, and future directions. *Weather and Forecasting* 18, 16–56.
- Kalnay, E. (2003). *Atmospheric Modeling Data Assimilation and Predictability*. Cambridge University Press, University of Maryland.
- Klein, P. M., P. A. Harr and R. L. Elsberry (2000). Extratropical transition of western north pacific tropical cyclones: An overview and conceptual model of the transformation stage. *Weather and Forecasting* 15, 373–395.
- Klein, P. M., P. A. Harr and R. L. Elsberry (2002). Extratropical transition of western North Pacific tropical cyclones: Midlatitude and tropical cyclone contributions to re-intensification. *Mon. Wea. Rev.* 132, 2240–2259.
- Knabb, R. D., D. B. Brown and J. R. Rhome (2006). Tropical cyclone report Hurricane Philippe 18-26 september 2005. National Hurricane Center .
- Leith, C. E. (1974). Theoretical skill of monte carlo forecasts. *Mon. Wea. Rev.* 102, 409–418.

- Leutbecher, M. and T. N. Palmer (2007). Ensemble forecasting. *J. Comp. Phys. on forecasting weather, climate and extreme events* , submitted.
- Leutbecher, M. and J. E. Paulsen (2004). Revised initial condition perturbations for the EPS and the 28r3 EPS e-suite. Memorandum Research Department .
- Lorenz, E. N. (1955). Available potential energy and the maintenance of the general circulation. *Tellus* 7, 157–167.
- Lorenz, E. N. (1956). Empirical orthogonal functions and statistical weather prediction. *Sci. Rep. 1. Statistical Forecasting Project, Departement of Meteorology, MIT (NTIS AD 110268)* , 49 pp.
- Lorenz, E. N. (1963a). Deterministic non-periodic flow. *J. Atmos. Sci.* 20, 130–141.
- Lorenz, E. N. (1963b). The predictability of hydrodynamic flow. *Trans. New York Acad. Sci., Ser. 2* 25, 409–432.
- Lorenz, E. N. (1965). A study of predictability of a 28-variable atmospheric model. *Tellus* 17, 321–333.
- Mo, K. and M. Ghil (1988). Cluster analysis of multiple planetary flow regimes. *J. Geophys. Res.* 93, 10927–10952.
- Morgan, M. C. and J. W. Nielsen-Gammon (1998). Using tropopause maps to diagnose midlatitude weather systems. *Mon. Wea. Rev.* 126, 2555–2579.
- NHC (2006). National Hurricane Center. <http://www.nhc.noaa.gov> .
- Palmer, T. N. (2004). Predicting uncertainty in forecasts of weather and climate. *ECMWF Technical Memorandum No. 294*.
- Palmer, T. N., R. Gelaro, J. Barkmeijer and R. Buizza (1998). SVs, metrics and adaptive observations. *J. Atmos. Sci.* 55, 633–653.
- Pedlosky, J. (1987). *Geophysical Fluid Dynamics*. 2nd edition, Springer-Verlag, New York.

- Peng, M. S. and C. A. Reynolds (2006). Sensitivity of tropical cyclone forecasts as revealed by singular vectors. *J. Atmos. Sci.* 63, 2508–2528.
- Pichler, H. (1984). *Dynamik der Atmosphäre*. Bibliographisches Institut Mannheim/Wien/Zürich.
- Puri, K., J. Barkmeijer and T. N. Palmer (2001). Ensemble prediction of tropical cyclones using targeted diabatic singular vectors. *Q. J. R. Meteorol. Soc.* 127, 709–731.
- Rappin, E. D., G. J. Tripoli and M. C. Morgan (2006). The tropical cyclone - jet interaction. *26th conference on hurricanes and tropical meteorology*.
- Rayleigh, J. W. S. (1880). On the stability, or instability, of certain fluid motions. *Proc. London Math. Soc.* 9, 57–70.
- Reynolds, C. A., R. Gelaro and J. D. Doyle (2001). Relationship between singular vectors and transient features in the background flow. *Q. J. R. Meteorol. Soc.* 127, 1731–1760.
- Riemer, M., S. C. Jones and C. A. Davis (2007). The impact of extratropical transition on the downstream flow: an idealised modelling study with a straight jet. *Q. J. R. Meteorol. Soc.* (to be submitted).
- Ritchie, E. A. and R. L. Elsberry (2007). Simulations of the extratropical transition of tropical cyclones: Phasing between the upper-level trough and tropical cyclones. *Mon. Wea. Rev.*, in press.
- Schönwiese, C.-D. (1985). *Praktische Statistik für Meteorologen und Geowissenschaftler*. Gebrüder Borntraeger, Berlin, Stuttgart.
- Szunyogh, I., Z. Toth, A. V. Zimin, S. J. Majumdar and A. Persson (2002). Propagation of the effect of targeted observations: The 2000 winter storm reconnaissance program. *Mon. Wea. Rev.* 130, 1144–1165.
- Thorncroft, C. D., B. J. Hoskins and M. E. McIntyre (1993). Two paradigms of baroclinic-wave-life-cycle behaviour. *Q. J. R. Meteorol. Soc.* 119, 17–55.

- Toth, Z. and E. Kalnay (1997). Ensemble forecasting at NCEP and the breeding method. *Mon. Wea. Rev.* 125, 3297–3319.
- Tracton, M. S. and E. Kalnay (1993). Operational ensemble prediction at the National Meteorological Center: practical aspects. *Weather and Forecasting* 8, 379–398.
- Untch, A., M. Miller, M. Hortal, R. Buizza and P. Janssen (2006). Towards a global meso-scale model: The high-resolution system T799L91 and T399L62 EPS. *ECMWF Newsletter No. 108*, 6–13.
- Velden, C. S., M. Hayden, S. J. Nieman, W. P. Menzel, S. Wanzong and J. S. Goerss (1997). Upper-tropospheric winds derived from geostationary satellite water vapor observations. *Bull. Amer. Meteor. Soc.* 78, 173–195.
- Webster, P. J. and H.-R. Chang (1997). Atmospheric wave propagation in heterogeneous flow: basic flow controls on tropical-extratropical interaction and equatorial wave modification. *Dynamics of Atmospheres and Oceans* 27, 91–134.
- Wilks, D. S. (1995). *Statistical methods in the atmospheric sciences*. Academic Press Limited, London.

List of symbols

\mathbf{A}_1	tangent linear model
α_{ek}	coefficient to weight the initial singular vectors
\mathbf{B}	weight matrix for final norm
β_{ek}	coefficient to weight the evolved singular vectors
\mathbf{c}_i	eigenvectors
\mathbf{C}	matrix which has eigenvectors as columns
c_p	specific heat at constant pressure
d_{ik}	distance between point k and cluster i
D	dimension
\mathbf{E}	weight matrix for the total energy norm at optimization time
\mathbf{e}_ϵ	ensemble member
\mathbf{E}_0	weight matrix for the total energy norm at initial time
ϵ	index for ensemble members
f	Coriolis parameter
\mathbf{F}	set of nonlinear coupled ordinary differential equations
g	gravity acceleration

γ	parameter for description of Lorenz attractor
G	index for grid points
\mathbf{H}	resolved processes in the calculation of an ensemble member
i, j, k	natural number
\mathbf{k}	unit vertical vector
κ	parameter for description of Lorenz attractor
\mathbf{L}	linear propagator including dry physics
\mathbf{L}_m	linear propagator including moist physics
λ_i	eigenvalues
$\mathbf{\Lambda}$	diagonal matrix of eigenvalues
m	natural number
\mathbf{M}	nonlinear model solution
μ_{ini}	coefficient to determine the magnitude of a perturbation at initial time
μ_{evo}	coefficient to determine the magnitude of a perturbation at final time
N	static stability
\mathbf{N}_{SV}	natural number of singular vectors
\mathbf{N}_{pf}	natural number of perturbed forecasts
ν_m	principal component
O	terms of high order
S	volume
p	pressure

p_r	reference pressure
p_{sfc}	surface pressure
\mathbf{P}	projection operator
ϕ	parameter for description of Lorenz attractor
Φ	variance-covariance matrix
Π	parametrized processes in the calculation of an ensemble member
Ψ	latitude coordinate
q	fuzziness coefficient
r	random number
R_d	gas constant of dry air
ρ	probability density function (pdf)
σ_i	singular values
σ_E	Eady index
Σ	diagonal matrix of singular values
t	time
T	temperature
T_r	reference temperature
θ	potential temperature
Θ	longitude coordinate
u	zonal wind component
\mathbf{u}	3-dimensional wind velocity vector

\mathbf{u}_i	evolved singular vectors
\mathbf{U}	matrix which has the evolved singular vectors as columns
v	meridional wind component
\mathbf{v}_h	horizontal wind velocity
\mathbf{v}_i	initial singular vectors
\mathbf{V}	matrix which has the initial singular vectors as columns
w_{ik}	weight for a point k associated with cluster i
\mathbf{W}	weight matrix for initial norm
\mathbf{X}	state of the atmosphere consisting of all model variables x_i
\mathbf{x}_i	model variables describing the state of the atmosphere
\mathbf{x}'_0	short for \mathbf{x}'_{i0} , perturbation of model variable \mathbf{x}_i at initial time
\mathbf{x}'_i	perturbation of model variable \mathbf{x}_i
z	vertical coordinate
Z	natural number denoting the total number of principal components
ζ	relative vorticity

List abbreviations

APE	available potential energy
ECMWF	European Centre of Medium Range Weather Forecasts
EOF	empirical orthogonal function
EPS	Ensemble Prediction System
ET	extratropical transition
ETKF	Ensemble Transform Kalman Filter
FCST	defined forecast time, FCST1 longer before ET, FCST2 shorter before ET
GMT	Greenwich Mean Time
Highres	experiments with configuration 31r1 and resolution L399T62
IFS	Integrated Forecasting System
JMA	Japan Meteorological Agency
Lowres	experiments with configuration 31r1 and resolution L255T62
NCEP	National Centers of Environmental Prediction
NHC	National Hurricane Center
NOAA	National Oceanic & Atmospheric Administration
Nopert	experiments without targeted perturbations around Tokage

Nosto	experiments without stochastic physics
UTC	coordinated universal time
PC	principal component
PCA	principal component analysis
Pert	experiments with targeted perturbations around Tokage
PrepIFS	an interactive meteorological application to prepare calculations with IFS
PV	potential vorticity
PVU	potential vorticity unit
RMSD	root-mean-squared difference
RMSE	root-mean-squared error
SST	sea surface temperature
STD	standard deviation
Sto	experiments with stochastic physics
SV	singular vectors
T255L40	resolution; exemplarily: truncation after wave number 255, 40 level
TC	tropical cyclone
TY	typhoon
WMO	World Meteorological Organization

Acknowledgements

First and most of all I want to thank my supervisor Prof. Sarah Jones. She gave me the opportunity to do this interesting work and supported it with great enthusiasm. During precious discussions with her I gained a lot of additional knowledge about the dynamics of the atmosphere. Through her numerous connections to the scientific world she gave me valuable possibilities for scientific exchange and international connections. I thank her for being not only a supervisor but also a friend.

Second, I would like to thank Prof. Pat Harr, who provided the analysis method I used for my work. By inviting me two times to the Naval Postgraduate School in Monterey he gave me the possibility to learn a lot from him about EOF analysis and clustering.

I would like to express my thanks to Dr. Martin Leutbecher who helped me creating my experiments with the ECMWF model and sustained my work with a lot of important ideas. The discussions with him were greatly appreciated. Furthermore, I would like to thank my user support Carsten Maas from the ECMWF for helping me running the ECMWF model.

I owe thanks to the ECMWF for providing me with data and with their model for my experiments.

Many thanks to Prof. Kottmeier who showed his trust in my work by accepted the co-correctorship.

My friends at the university, especially Michael Riemer, Juliane Schwendike, Ralph Lux, Kai Schmidt, Hans Schipper and Simon Lang, were a great help not only through reading my work and giving useful comments but also through creating a relaxed and enjoyable atmosphere at the university.

Additionally, I want to thank our secretary Olgica Birnmeier for her help with administrative work and for bringing so much liveliness in our institute. I also thank Friederike Schönbein for having so much patience with me and my travel expenses.

Further, I would like to thank Gerhard Brückel for helping me with numerous computer problems. I owe special thanks to Mario Mech for his appreciated telephonic support during my computer crash.

I would have never had the possibility to study without the support of my parents, Irene and Walter Anwender, my brother, Andy Anwender, and my grandmother Aloisia Brauner. I thank them very much for their trust in me, their financial support and their proudness.

My boyfriend Hansi Hoefl played and plays a special role in my working and private life. Through his lively interest in my work and his constant curiosity in everything new he was a precious partner for discussions. I want to thank him for his love and comfort during my work.